UNIVERSITY OF KASSEL
FACULTY 10 - MATHEMATICS AND SCIENCES

Micromagnetic simulations of exchange biased micro geometries

Master thesis

Physics

Date of submission: April, 2023

Lukas Paetzold

1st Assessor:

Prof. Dr. Arno Ehresmann

2nd Assessor:

Prof. Dr. Kilian Singer

Abstract

As first observed by Meiklejohn and Bean [Mei56] and described as a unidirectional anisotropy, the exchange bias is a well-known interface effect between antiferromagnetic and ferromagnetic thin films. Initiated by field cooling [Mei56], sputter deposition [Ber99], or light-ion bombardment [Eng05] the effect appears as a shift of the hysteresis loop and increased coercive fields [Nog99]. Experimental studies on freestanding and embedded geometries in the micrometer range show an asymmetric magnetic reversal in hysteresis measurements [Akh22] and a dependence of the exchange bias effect on the geometry sizes. Micromagnetic simulations in Mumax3 [Van14, Cle16] are presented for investigating the magnetic reversal processes in exchange biased thin film systems with a polycrystalline uncompensated antiferromagnetic interface. Full film simulations are presented and compared to existing Stoner-Wohlfarth simulations [Har12], showing the general validity of the model presented here. Applied to different freestanding and embedded geometries like stripes, squares, and discs in the micrometer range, reproduction of the observed reversal processes and size dependencies are achieved, by extending the model to incorporate effects of the geometry edges. Further, the influence of ion bombardment is incorporated in the simulations for embedded geometries. The model is finally used to predict the magnetic behavior of embedded squares and discs.

Contents

Eigenständigkeitserklärung

Hiermit bestätige ich, dass ich die vorliegende Arbeit selbständig verfasst und keine anderen als die angegebenen Hilfsmittel benutzt habe. Die Stellen der Arbeit, die dem Wortlaut oder dem Sinn nach anderen Werken (dazu zählen auch Internetquellen) entnommen sind, wurden unter Angabe der Quelle kenntlich gemacht.

_____

Ort, Datum, Unterschrift

1 Introduction

The exchange bias (EB) effect is a well-known interface effect between ferromagnetic (FM) and antiferromagnetic (AFM) interfaces, originating from the exchange interaction between the FM and AFM moments on the interfaces between them. Macroscopically the effect can be observed in a horizontal shift of the hysteresis loop and increased coercive fields [Nog99]. This unidirectional anisotropy is mediated by an exchange interaction between FM interface spins and AFM spins with a fixed direction and is only present if the effect has been initialized by field cooling (FC) [Mei56], in the sputter deposition process [Ber99], or by light-ion bombardment (IB) [Eng05]. The EB effect is of great technological importance. For instance, in magnetic hard disk drives the read heads are based on the giant magnetic resistance effect [Fer08] and utilize the EB effect [Rad08]. Further than that, the effect is used in up-to-date development of magnetic random access memory [Rad08]. Besides the usage in information technology, the effect is used in magnetic pattering of surfaces to design stray field landscapes for lab-on-the-chip devices [Ehr15, Gau16]. Over time many different theoretical models have developed [Mei56, Mau87, Kiw01, Rad08, Har12, Mü16, Mer22a], but non of which were able to reproduce all experimental observations.
In the group, exchange biased patterned geometries with lateral dimensions in the micrometer scale have been fabricated and the magnetic reversal processes were investigated [Akh22]. The geometries are stripes, squares, or discs created by lithography in a periodic pattern. Most of the geometries are topographically arising from the substrate surface, but also embedded geometries, created by IB, were characterized. The EB effect was initialized with a magnetic field in the sputter deposition process and increased by FC. When investigating the samples, interesting magnetization reversal and nucleation behaviors were observed by Kerr microscopy depending on the hysteresis branch. On the decreasing field branch (DFB) the nucleation is more pronounced in the stripe's centers for instance. On the increasing field branch (IFB) the nucleation takes place on the edges. This is called asymmetric nucleation in this work. Connected to that, a higher nucleation density could be observed on the IFB. Further, the EB effect depends on the geometry size. For instance, the EB field increases with decreasing stripe width. The goal of this work is to investigate this behavior within micromagnetic simulations, which provide the possibility to incorporated the effects of the direct exchange interaction and stray fields resulting from limited geometry sizes [Abe19] and are therefore well suited to simulate the geometries. Compared to a classical Stoner-Wohlfarth approach, the FM magnetization is not simulated with just a single vector, rather than a complete three-dimensional vector field, allowing, for

instance, to investigate nucleation in detail. Micromagnetic simulations have therefore proven to be a suitable tool to simulate FM materials and geometries [Lel18]. Further, simulations are an important tool to investigate the observed effects form a theoretical point-of-view and allow to anticipate experimental results before the samples are elaborately fabricated. For the simulations presented here, MuMax3 was used, which is a finite-difference-based micromagnetic simulation program, that uses the GPU to accelerate the computation [Van14]. An already existing model by De Clercq [Cle16] will be extended and the experimentally observed properties will be reproduced. The extensions are further compared and validated with the experimental results.

This work is structured in the following way: A theoretical background will be presented in Chap. 2. By explaining basic magnetic interactions, the different types of magnetism will be introduced. Followed by the important magnetic anisotropies, the foundation for the exchange bias will be built. The chapter ends with a detailed overview of the exchange bias effect and general modeling approaches of magnetism. In Chap. 3 an overview of the experimental methods connected to this work will be presented. First, the fabrication and preparation of the samples will be explained. Secondly, the three used characterization methods are presented. These are the atomic force microscope, the vibrating sample magnetometry, and the Kerr microscopy. In Chap. 4 more details on the different modeling approaches of the exchange bias effect in thin film systems will be given. Furthermore, the basis of the used model by De Clercq will be explained. In Chap. 5 the results will be presented. By simulating full film systems and performing parameter studies, the usability of the model will be investigated. Afterward, the different geometries will be simulated in Sec. 5.2. The model will thereby be extended with an so-called edge region, that builds the basis for all simulations done. The observed nucleation asymmetry in the freestanding stripes can be simulated in two different ways. By increasing the pinning ratio (Sec. 5.2.1) or by a reduced saturation magnetization (Sec. 5.2.2). For both approaches, an experimental study, as a test for plausibility, was performed and will be presented. The freestanding stripes are followed by embedded stripes in Sec. 5.3. Here, the influence of the IB was simulated. In the end, simulations for freestanding squares and discs will be presented in Sec. 5.4 and, finally, embedded squares and discs will be simulated. Since there are no experimental results for these geometries so far, the results are an outlook for future experiments.

2 Theoretical background

First of all, a theoretical overview of magnetism will introduce the underlying physics. Starting with magnetism on an atomic scale, the magnetic moment resulting from the electron's motion and intrinsic spins will be explained. By describing interactions between different magnetic moments, magnetism on a macroscopic scale will be introduced. After discussing non-collective and collective magnetism, the preferred orientation of magnetic moments, called anisotropy will be described. By this, also energy considerations will be made, resulting in further effects like magnetic domains and reversal processes. Special focus will put further on the exchange bias effect present in the investigated samples. In the end, the important model of Stoner-Wohlfarth and the micromagnetic formulation will be presented, building the basis for the modeling described in later chapters.

2.1 Magnetic moment

The basis of the magnetism of solids is the magnetic moment $\vec{\mu}$ of a single atom, representing the strength of a magnetic dipole created by the motion of the electron around the nucleus [Kas05].
In the point of view of classical physics, the electron is moving on a circular path around the nucleus. The electron's motion on this path, surrounding an area $\vec{A} = A\vec{n}$, forms a current I, which leads to the definition of the magnetic moment [Kas05, Mes15]

$$\vec{\mu} = I\vec{A}. \tag{2.1}$$

Given the angular momentum $\vec{l} = m_e \omega r^2 \vec{n}$, with electron mass m_e, frequency ω, radius r of the path around the nucleus and the current $I = -e\omega/(2\pi)$, with electron charge e, the magnetic moment is given by [Kas05]

$$\vec{\mu}_l = -\frac{e}{2m_e}\vec{l}. \tag{2.2}$$

Since the angular momentum of the electron $\vec{l}$ is a quantum mechanical property, its magnitude is discretized by the angular orbital quantum number l and $\vec{l}^2 = l(l+1)\hbar^2$, with the reduced plank constant $\hbar = h/(2\pi)$. This results in the definition of the Bohr magnetron

$$\vec{\mu}_B = \frac{e\hbar}{2m_e}, \tag{2.3}$$

which represents the smallest magnetic moment of an electron for $l = 0$ [Kas05]. Besides the electron, the nucleus has a magnetic moment following the same idea. But because the nucleus is much heavier than the electron and the magnetic moments is inversely proportional to the mass, the magnetic moment is neglectable [Kas05].
Incorporating relativistic effects, represented by the Dirac equation, it can be shown that the electron owns a purely quantum mechanical internal magnetic moment, known as the spin [Sak17]. The spin $\vec{s}$ is an additional magnetic moment, which is also present if there is no angular moment in the atom and has been observed in the Stern-Gerlach experiment [Ger22]. Analogously to the angular momentum, the spin is given by the spin quantum number $s = \pm\frac{1}{2}$ for electrons and $\vec{s}^2 = s(s+1)\hbar^2$, leading to the spin moment

$$\vec{\mu}_\mathrm{s} = -g_\mathrm{e}\frac{e}{2m_\mathrm{e}}\vec{s}, \tag{2.4}$$

with gyromagnetic ratio $g_\mathrm{e} = 2.002$, representing the ratio between the magnetic moment and the angular momentum [Kas05,Mes15]. This means that the magnetic moment is approximately two times higher than expected in the classical case. The two different magnetic moments lead to the later discussed forms of magnetism in solids.
The total magnetic moment is given by the sum of both moments

$$\vec{\mu}_\mathrm{j} = \vec{\mu}_\mathrm{l} + \vec{\mu}_\mathrm{s} = -\mu_\mathrm{B}(\vec{l} + g_\mathrm{e}\vec{s}) = -g_\mathrm{j}\frac{e}{2m_\mathrm{e}}\vec{j}. \tag{2.5}$$

Thereby the spin $\vec{s}$ and the orbital angular momentum $\vec{l}$ is coupling to the total angular momentum $\vec{j}$ [Kas05]. The Lande - factor g_j is given by

$$g_\mathrm{j} = 1 + \frac{j(j+1) + s(s+1) - l(l-1)}{2j(j+1)}. \tag{2.6}$$

2.1.1 Spin-orbit interaction

The coupling of the orbital magnetic moment $\vec{\mu}_\mathrm{l}$ and the spin magnetic moment $\vec{\mu}_\mathrm{s}$ is the result of the spin-orbit interaction. Thereby, the electron observes a magnetic field created by the nucleus and its motion around the electron, which is interacting with the electron's spin. The resulting energy of this interaction is given by

$$E_\mathrm{ls} = \frac{e}{2m_\mathrm{e}^2c^2}\frac{1}{r}\frac{\mathrm{d}V}{\mathrm{d}r}\vec{l}\cdot\vec{s}, \tag{2.7}$$

with r representing the electron's distance from the nucleus and V the Coulomb potential of the nucleus [Kas05]. The gradient of V is increasing with increasing mass, leading to two extreme cases: For heavy atoms, the orbital and spin moments of the electrons couple to individual total angular moments $\vec{j}_\mathrm{i}$. These moments then couple via the jj-coupling, resulting in the total

angular moment

$$\vec{J} = \sum_{\mathrm{i}} \vec{j}_{\mathrm{i}}. \tag{2.8}$$

For light atoms, the electron spins couple to a total spin $\vec{S}$ and the orbital angular momentum couple to a total orbit angular moment $\vec{L}$ following

$$\vec{L} = \sum_{\mathrm{i}} \vec{l}_{\mathrm{i}} \text{ and } \vec{S} = \sum_{\mathrm{i}} \vec{s}_{\mathrm{i}} \tag{2.9}$$

first, which leads to the total angular moment

$$\vec{J} = \vec{L} + \vec{S}. \tag{2.10}$$

A consequence of the spin-orbit coupling is the Hund's law [Kas05,Hun25]. The Pauli principle forbids electrons with the same set of quantum numbers to occupy the same state. Since electrons have two possible spin quantum numbers $\pm 1/2$, only two electrons with opposite spins are allowed per state. Hund's law dictates how orbitals of an atom are filled with electrons, assuming the ground state to have the lowest energy. The energy contributions are the Coulomb energy, the exchange energy (see Chap. 2.2.2) and the spin-orbit coupling. All in all, there are three rules [Kas05]:

- As the total spin $\vec{S}$ is maximized, the spins have a larger distance to each other, fulfilling the Pauli principle and reducing the Coulomb energy.
- The total orbit angular momentum $\vec{L}$ is maximized, for a given total spin $\vec{S}$. A larger $\vec{L}$ implies larger distances between electrons and consequently a reduced Coulomb energy.
- The total angular momentum $\vec{J}$ is minimized for less than half filled shells and maximized for more than half filled shells, minimizing the spin-orbit coupling energy.

2.1.2 Zeeman interaction

For a given total angular momentum J, the corresponding energy is $2J+1$ degenerated. Implying that all states associated with a total angular momentum J have the same energy. When applying an external magnetic field B, this degeneracy is broken and split into $2J+1$ different states. Each of these states is characterized by their secondary total angular quantum number m_{J} and its projection $J_{\mathrm{z}} = m_{\mathrm{J}}\hbar$ of the total angular moment along the field [Kas05, Mes15].

2.2 Magnetic interactions

So far, only interactions within one atom have been considered. For magnetism, the interactions between different atoms play an important role, leading to an ordering of the magnetic moments and to a macroscopic magnetic state of the solid. This collective ordering is distinguished in ferro-, antiferro- and ferrimagnetism. Before the macroscopic effects are introduced, the dipole-dipole interaction and the direct exchange interaction will be discussed.

2.2.1 Dipole-Dipole interaction

The magnetic moment of one atom μ_i is creating a magnetic field

$$\vec{B}(\vec{r}) = \mu_0 \left(\frac{3(\vec{\mu}_\mathrm{i} \cdot \vec{r})\vec{r}}{r^5} - \frac{\vec{\mu}_\mathrm{i}}{r^3} \right), \tag{2.11}$$

with the magnetic permeability of the vacuum μ_0, and the distance to the magnetic moment r [Kas05]. This magnetic field interacts with a second magnetic moment $\vec{\mu}_\mathrm{j}$ resulting in an energy term

$$E(\vec{r}) = -\vec{\mu}_\mathrm{j} \cdot \vec{B}(\vec{r}) = \mu_0 \left(\frac{\vec{\mu}_\mathrm{i} \cdot \vec{\mu}_\mathrm{j}}{r^3} - \frac{3(\vec{\mu}_\mathrm{i} \cdot \vec{r})(\vec{\mu}_\mathrm{j} \cdot \vec{r})}{r^5} \right), \tag{2.12}$$

with distance r between both magnetic moments [Kas05]. The energy of the dipole-dipole interaction is minimized, if the magnetic moments are oriented parallel to each other, leading theoretically to a collective behavior of the moments. In reference [Kas05] an estimation of a typical energy contribution is given. Given two ions with $r = 3\,\mathrm{nm}$ and $\mu = \mu_\mathrm{B}$ the dipole-dipole interaction energy is in the order of $10^{-6}\,\mathrm{eV}$ or a corresponding temperature in the sub-Kelvin regime of $0,01\,\mathrm{K}$. This indicates that the collective effects leading to, for instance, ferromagnetism, are not based solely on the dipole-dipole interaction. Nonetheless, the dipole-dipole interaction is present over long distances and lead to shape anisotropy and domain formation, as will be shown later.

2.2.2 Direct exchange interaction

As has been discussed so far, electrons and their intrinsic spin are responsible for magnetism. Because electrons have a half-integer spin, they behave like fermions. This leads to the antisymmetry of the total many-particle wave function [Kas05, Sak17]. Separating the wave function into a space function and a spin function, two possible cases emerge, for which the product of both results in an antisymmetric wave function. First, the space function can be symmetric, and the spin function can be antisymmetric. Second, the space function can be antisymmetric, and the spin function can be symmetric [Kas05, Sak17].
When considering a two-electron system, the wave function $\Phi(\vec{r}_1\sigma_1, \vec{r}_2\sigma_2)$ is defined by the product of a space wave function $\Psi(\vec{r}_1, \vec{r}_2)$ and spin wave function $\chi(\sigma_1, \sigma_2)$, with electron

coordinates $\vec{r}_\mathrm{i}$ and spins σ_i. The indistinguishability now implies [Kas05]:

$$\Psi(\vec{r}_1,\vec{r}_2) = (-1)^l \Psi(\vec{r}_2,\vec{r}_1). \tag{2.13}$$

For even l the space function is symmetric, and the spin function has to be antisymmetric resulting in the singlet state [Kas05]:

$$\chi = \frac{1}{\sqrt{2}}(|\uparrow\downarrow\rangle - |\downarrow\uparrow\rangle) \tag{2.14}$$

For odd l the space function is antisymmetric, and the spin function has to be symmetric resulting in the triplet states [Kas05]:

$$\chi = |\uparrow\uparrow\rangle \tag{2.15}$$
$$\chi = \frac{1}{\sqrt{2}}(|\uparrow\downarrow\rangle + |\downarrow\uparrow\rangle) \tag{2.16}$$
$$\chi = |\downarrow\downarrow\rangle \tag{2.17}$$

In Fig. 2.1 the space wave function and the orientation of the spins are visualized, indicating that the parallel alignment of the spins goes along with an increased average distance between the electrons. This is known as the Pauli-exclusion principle and results in the exchange hole. For an antiparallel orientation, the electron can reduce its distance. Nevertheless, the Coulomb repulsion limits the distance, even though the Pauli-exclusion principle is not affected, which is known as the correlation hole. Overall, this exchange interaction results in ferro- or antiferromagnetic states depending on the different energy contributions as discussed now [Kas05].

Since the singlet and the triplet states have different energies, a so called exchange-energy

$$E_\mathrm{ex} = E_\mathrm{s} - E_\mathrm{t} \tag{2.18}$$

can be defined with singlet energy E_s and triplet energy E_t. Furthermore, the interaction between two neighboring spins σ_i can be described in the Heisenberg model using the exchange energy following

$$H_\mathrm{ex} = -(E_\mathrm{s} - E_\mathrm{t})\frac{1}{\hbar^2}\vec{\sigma}_1 \cdot \vec{\sigma}_2 = -2J_\mathrm{ex}\frac{1}{\hbar^2}\vec{\sigma}_1 \cdot \vec{\sigma}_2, \tag{2.19}$$

with $J_\mathrm{ex} = (E_\mathrm{s} - E_\mathrm{t})/2$. This exchange interaction is the main reason for collective magnetism. Depending on the sign of J_ex the spins will align parallel or antiparallel, resulting in ferromagnetism ($J_\mathrm{ex} > 0$) or antiferromagnetism ($J_\mathrm{ex} < 0$) [Kas05]. J_ex is called the exchange constant [Sak17].

For a solid, the Heisenberg model can be used as an approximation for the spin interaction.

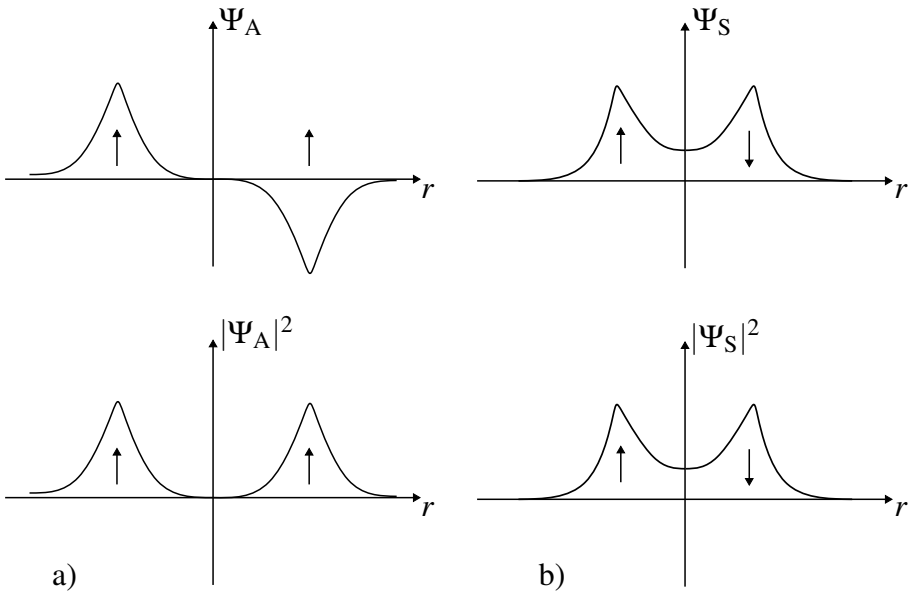

Figure 2.1: Schematic of an antisymmetric (a) and symmetric (b) space wavefunction and the corresponding probability distribution. The Pauli-exclusion principle permits the electrons to be close to each other if there spin is pointing in the same direction. Adapted from [Kas05].

Given n spins, the Heisenberg model reads

$$H_{\mathrm{ex}} = -2\frac{1}{\hbar^2}\sum_{\mathrm{i,j(i<j)}}^{n} J_{\mathrm{ex,ij}}\vec{\sigma}_{\mathrm{i}}\cdot\vec{\sigma}_{\mathrm{j}}, \tag{2.20}$$

with $i < j$ preventing double counting of spins. Typically, only next neighbor spin-spin interaction is considered by defining $J_{\mathrm{ex,ij}} = 0$ for non-neighboring spins i and j.
Furthermore, $J_{\mathrm{ex,ij}}$ depends on the distance between the spins i and j. This is a result of the Pauli-exclusion principle as discussed before. For small atom distances, the Coulomb energy between the cores is minimized if the electrons are located between them. Following the exclusion principle, the electron spins need to align antiparallel, resulting in a negative J_{ex}. For larger atomic distances, the electrons also prefer larger distances because of the Coulomb repulsion. At the same time, the parallel orientation of the spins is now preferred since the exclusion principle is not violated. In the end, this leads to a parallel orientation of all spins. The overall trend is summarized in the Berthe-Slater curve, as shown in Fig. 2.2 [Kas05].

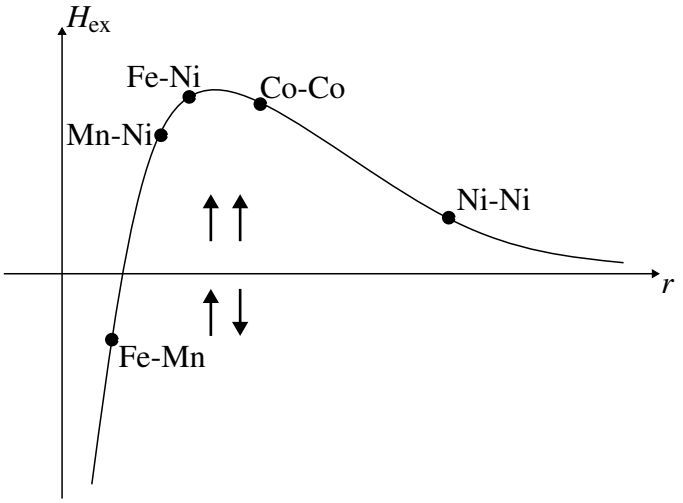

Figure 2.2: Bethe-Slater curve with some materials as reference points. For small atomic distances, the Heisenberg exchange energy H_{ex} becomes negative, leading to an antiparallel alignment of neighboring spins. For larger distances, H_{ex} becomes positive, leading to ferromagnetism, and for even larger distances, H_{ex} stays positive but is small compared to thermal fluctuations and leads therefore to paramagnetism. Adapted from [Kas05].

2.3 Dia-, Para- and Ferromagnetism

As discussed in the last chapter, the exchange interaction is the main reason for collective magnetism. In the following section different types of magnetism will be explained.
So far, single magnetic moments have been classified, and their interactions among themselves. Typically, if a solid is inserted into an external field with field strength $\vec{H}$, magnetic moments will be created and or aligned to the field. The resulting total magnetic moment per volume element is then called magnetization $\vec{M}$ [Kas05, Mes15]. The sum of $\vec{H}$ and $\vec{M}$ is the magnetic field $\vec{B}$ given by

$$\vec{B} = \mu_0(\vec{H} + \vec{M}). \tag{2.21}$$

In case of a linear dependence between $\vec{H}$ and $\vec{M}$ the magnetic susceptibility χ is defined via

$$\vec{M} = \chi\vec{H}. \tag{2.22}$$

Examples for constant χ are dia- and paramagnetism, while the collective behavior of ferro- and antiferro magnetism cannot simple described by a constant χ [Kas05, Mes15]. In the following, the different types will be discussed.

2.3.1 Diamagnetism

Within an external field, the orbital moments of the electrons begin to precess around the magnetic field. The frequency is given by the Larmor frequency ω_L, and depend on the field strength

B, electron charge e and its mass m_e [Kas05] as

$$\omega_L = \frac{eB}{2m_e}. \tag{2.23}$$

This precession leads to a change in the circular current around the nucleus by

$$\Delta I = -Ze\frac{\omega_L}{2\pi} = -\frac{Ze^2}{4\pi m_e}B \tag{2.24}$$

and, as can be seen by equation (2.1), to a change of the magnetic moment

$$\Delta\mu = \frac{Ze^2}{4m_e}B\left\langle\rho^2\right\rangle, \tag{2.25}$$

where $\left\langle\rho^2\right\rangle = \left\langle x^2\right\rangle + \left\langle y^2\right\rangle$ is the average orbital radius around the field axis [Kas05]. It can furthermore be shown that the susceptibility is given by

$$\chi_L = -\frac{\mu_0 N_0 Ze^2}{6m_e}\left\langle r^2\right\rangle. \tag{2.26}$$

This susceptibility is called Langevin susceptibility and is typically much smaller than the susceptibility of paramagnetic materials and therefore only relevant if $L = 0$ and $S = 0$ [Kas05]. Since χ_L is negative, the resulting magnetization is always opposed to the inducing external field, following Lenz's law [Mes15].
Besides a precession of the angular momentum of the bond electrons, a small diamagnetic effect of the quasi-free electrons in the conduction band is observable. This is known as Pauli diamagnetism and the susceptibility is given by one-third of the susceptibility of the paramagnetic Pauli magnetism [Kas05], which will be discussed next.

2.3.2 Paramagnetism

Besides diamagnetism, paramagnetism can be observed if permanent magnetic moments are present, which align in an external field due to Zeeman interaction. Permanent magnetic moments are present if there is an odd number of electrons in the atom, if the inner shells of atoms and ions in solids are only partly filled, or if the material is a metal.
As discussed in Sec. 2.2.1, magnetic moments align in an external magnetic field to minimize the Zeeman energy

$$E_{\text{Zeeman}} = -\vec{\mu}\cdot\vec{B}_{\text{ext}} = -\mu B_{\text{ext}}\cos\Theta. \tag{2.27}$$

Besides the zeeman energy, thermal fluctuation have to be considered. The fluctuations can be described by the Boltzmann distribution. Under the assumption that the free energy is minimized, the number of magnetic moments pointing into the solid angle element $\mathrm{d}\Omega\sin\Theta\mathrm{d}\Theta\mathrm{d}\Phi$ is

proportional to $\exp(-E_{\text{Zeeman}}/k_{\text{B}}T)$, with Boltzmann constant k_{B} and temperature T [Kas05]. In thermal equilibrium the macroscopic magnetization of N magnetic moments is given by an average distribution $\langle\cos\Theta\rangle$ leading to

$$M = N\mu_{\text{B}}\langle\cos\Theta\rangle\,. \tag{2.28}$$

For small temperatures and/or strong fields all magnetic moments point into the same direction adding up to

$$\vec{M} = Ng_{\text{J}}\mu_{\text{B}}\vec{J}, \tag{2.29}$$

with total angular momentum J and Lande - factor g_{J}. Using the Boltzmann distribution it can be shown that $\vec{M}$ is proportional to the external field

$$\vec{M} = \chi\vec{B}, \tag{2.30}$$

with the paramagnetic susceptibility χ, given by the temperature T and a material depended on constant C, called the Curie constant, as

$$\chi = \frac{C}{T}. \tag{2.31}$$

For paramagnetic materials, the exchange interaction between neighboring spins is only weakly present. At room temperature, the thermal fluctuations prevent the magnetic moments from aligning, since the typical exchange energy is below the potential energy of the fluctuations. In Fig. 2.3 a schematic of a paramagnet at room temperature is drawn, showing the non-ordered state. If the exchange interaction is dominating thermal fluctuations, an ordered magnetic state can establish [Kas05].

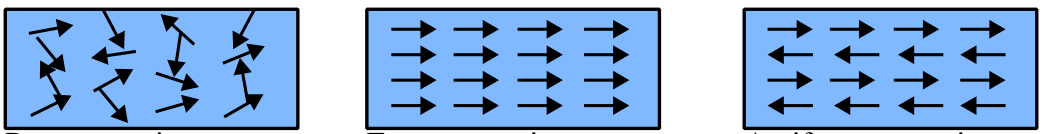

Figure 2.3: Schematic of different magnetic states. The paramagnetic state is showing a non-ordered orientation of the magnetic moments. While in the ferromagnetic state, all moments are aligned parallel. For the antiferromagnetic state, neighboring moments are aligned antiparallel.

2.3.3 Ferromagnetism

For materials with a strong exchange interaction, like iron, nickel, and cobalt, the magnetic spins align parallel as long as the temperature is below a certain value, known as the Curie-temperature T_{C} (see Fig. 2.3). In this case, even at vanishing external field a non-vanishing

magnetization can be present. These materials are called ferromagnetic (FM). Besides that, the magnetization depends also on the history of the sample [Kas05].
The interaction between the magnetic moments can be interpreted as a molecular field. Given an atom i with spin $\vec{S}_\mathrm{i}$ the exchange energy with its n nearest neighbors is given by

$$E_\mathrm{ex}^i = -2J_\mathrm{ex}\frac{1}{\hbar^2}\vec{S}_\mathrm{i}\sum_\mathrm{n}\vec{S}_\mathrm{j}. \tag{2.32}$$

Using the thermal average $\left\langle \vec{S}_\mathrm{j} \right\rangle$ for the neighboring atomic spins, the energy changes to

$$E_\mathrm{ex}^i = -2nJ_\mathrm{ex}\frac{1}{\hbar^2}\vec{S}_\mathrm{i}\left\langle \vec{S}_\mathrm{j} \right\rangle. \tag{2.33}$$

Using Equ. 2.28 for the magnetization

$$\vec{M} = -N_0 g\mu_\mathrm{B}\frac{1}{\hbar}\left\langle \vec{S}_\mathrm{j} \right\rangle \tag{2.34}$$

the exchange energy is

$$E_\mathrm{ex}^i = -\left(-g\mu_\mathrm{B}\frac{1}{\hbar}\vec{S}_\mathrm{i}\right)\frac{2nJ_\mathrm{ex}}{N_0 g^2\mu_\mathrm{B}^2}\vec{M}. \tag{2.35}$$

Interpreting $-g\mu_\mathrm{B}\frac{1}{\hbar}\vec{S}_\mathrm{i}$ as an magnetic dipole in an field $\vec{B}_\mathrm{ex}$, the field can be calculated as

$$\vec{B}_\mathrm{ex} = \frac{2nJ_\mathrm{ex}}{N_0 g^2\mu_\mathrm{B}^2}\vec{M} = \lambda_\mathrm{ex}\mu_0\vec{M}. \tag{2.36}$$

This field is called molecular field and is representing the internal field created by the magnetization of the sample. The factor λ_ex is called molecular field constant [Kas05].
The molecular field is responsible for the collective ordering of the magnetic moments in FM materials. When applying an external field $\vec{B}$, the molecular field needs to be considered resulting in an effective field

$$\vec{B}_\mathrm{eff} = \vec{B} + \vec{B}_\mathrm{ex}. \tag{2.37}$$

Since the effective field depends on the magnetization of the sample, there is no simple connection between magnetization and field like in the case of dia- or paramagnetism. The susceptibility itself depends not only on the temperature T, but also on the external field $\vec{B}$ and the magnetization $\vec{M}$ [Kas05].
To visualize this, a typical hysteresis loop is shown in Fig. 2.4 and can be obtained by measuring the magnetization of the sample in an external field from positive to negative saturation and back to positive saturation. If the sample as never been magnetized in a field and has no magnetization on its own, the curve starts in the center. With increasing field, the magnetization approaches its saturation M_S (light blue curve), where all spins are aligned parallel. When reducing the field, the magnetization will not follow the same path again. Instead, the sample

tends to keep its magnetization even at zero external field (remnant magnetization M_R). The exchange interaction between the spins is keeping them aligned. Further reducing the field, the magnetization will decrease and vanish at $H_{C,l}$. Finally, the magnetization will reach negative saturation in further decreased fields. When increasing the fields again, the process is mirrored. The fields $H_{C,l}$ and $H_{C,r}$ are called coercive field and represent the width of the loop [Mes15].

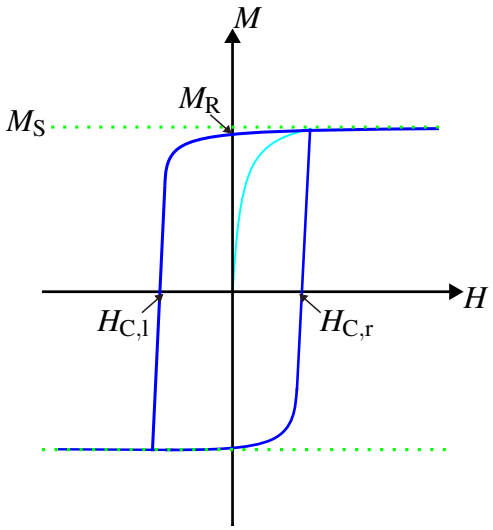

Figure 2.4: Schematic of a typical hysteresis loop of a magnetic material. In light blue, the initial magnetization curve is indicated. In blue, the actual hysteresis loop is sketched and reaches from positive to negative saturation M_S. At zero field, the remnant magnetization M_R can be found. The width of the hysteresis loop is given by the coercive fields $H_{C,l}$ and $H_{C,r}$.

The change in the magnetization is known as magnetization reversal. The processes involved will be explained in detail in Sec. 2.5.2. In short, the magnetization reversal can take place by coherent rotation, nucleation, movement of domain walls and by spin flips [Kas05]. The processes can also be characterized by the hysteresis curve. Coherent rotation is characterized by a slowly changing magnetization, typical for hard axis (see 2.4). Along easy axis mostly spin flop, nucleation and domain wall motion can be observed, characterized by abrupt changes in the magnetization [Kas05].
As already said, the shape of the hysteresis loop strongly depends on the direction of the external field. The reason are magnetic anisotropies, as will be explained in the next chapter. But before that, antiferromagnetism will be explained as a result of negative exchange interaction constants.

2.3.4 Antiferromagnetism

As indicated in the Bethe-Slater curve (see Fig. 2.2) negative exchange coupling constants are possible, leading to antiferromagnetic (AFM) materials. Negative coupling constants are a consequence of the Pauli-exclusion principle, since closely neighboring electrons need to have

opposite spin directions. In AFM materials neighboring spins therefore possess an antiparallel alignment (see Fig. 2.3). Averaged over a macroscopic volume, the magnetization is vanishing. Analogously to FM materials, above a critical temperature, the AFM ordering is destroyed, and paramagnetic behavior is present. This temperature is called Nèel temperature T_N [Kas05]. In this work, the AFM spin structure is thought of as uncompensated, like it is shown in Fig. 2.3, meaning that the spins align layer-wise.

2.4 Magnetic anisotropies

So far, the orientation of the macroscopic magnetization is not further defined. When investigating magnetic materials, often a preferred orientation of the magnetization is observable. For instance, the magnetization of a thin FM wire tends to point along the wire due to the minimization of the stray field [Fra00]. The preferred orientation is called easy direction or easy axis. Along the easy axis or direction, the free energy is minimized in respect to the angle between magnetization and axis. Opposed to that, the hard direction or axis is maximizing the free energy. For the easy axis, smaller fields are sufficient to saturate the magnetization compared to the hard axis for a given system. In Fig. 2.5 typical hysteresis loops along the easy and the hard axes are plotted. The easy axis hysteresis shows a steep change in magnetization from positive to negative saturation and vise versa. The magnetization along the hard axis is changing way more linearly with the field. Knowing that the energy necessary for the change of the magnetization is given by the area above the hysteresis, the anisotropy energy ΔE_{anis} can be calculated by

$$\Delta E_{\text{anis}} = \mu_0 \int_0^{M_s} H_{\text{hard}}(M)\mathrm{d}M - \mu_0 \int_0^{M_s} H_{\text{easy}}(M)\mathrm{d}M \tag{2.38}$$

The origin of easy and hard axes are magnetic anisotropies [Kas05]. The interplay of all anisotropies result in an energy landscape in respect to the angle between magnetization and total anisotropy. In the following, the most important anisotropies for this thesis are introduced.

2.4.1 Magneto-crystalline anisotropy

The preferred alignment of the spins to the crystal's lattice is called magneto-crystalline anisotropy. The origin is the spin-orbit interaction between the electron's spins and the angular moments of the orbits [Kas05]. The electron spins on its own are interacting through exchange interaction, which is isotropic, meaning that the exchange energy is independent of the spin's orientation as long as the spins are parallel. But the spin-orbit interaction is coupling the spins to the angular moments. The angular moments therefore also rotate if the spin's orientation is changed by an

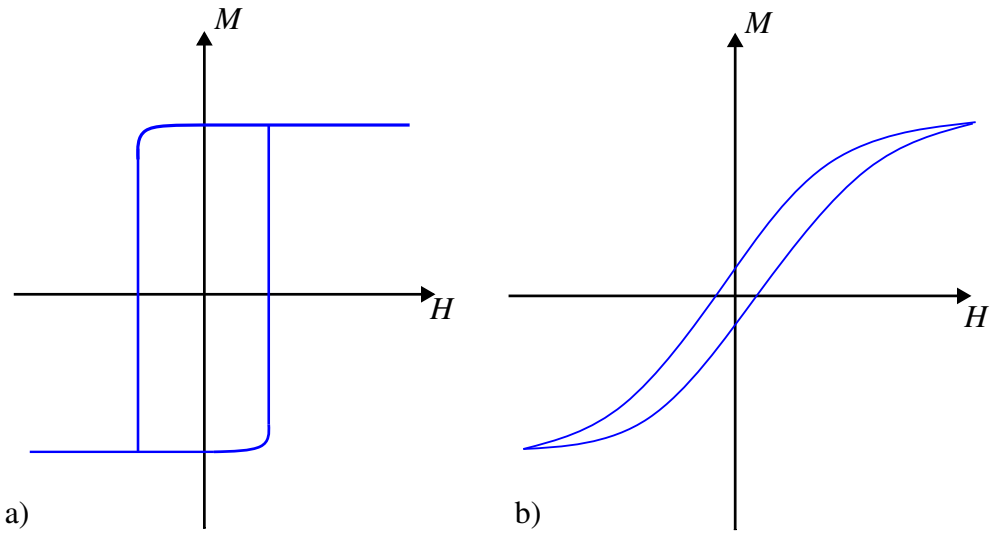

Figure 2.5: Illustration of hysteresis loops along the easy axis (a) and the hard axis (b). The easy axis hysteresis shows a steep reversal with a large coercive field. The hard axis hysteresis instead shows a gradual reversal with a small coercive field.

external field. In some materials, i.g. transition metals, the orientation of the angular moments is not isotropic and connected to an angular dependence. That means that also the spin orientation is angular dependent [Kas05].
In order to describe the anisotropy phenomenologically, a power series expansion is used. A coordinate system $(\alpha_1, \alpha_2, \alpha_3)$ is defined using the direction of the magnetization (θ, ϕ) in cubic coordinates and is given by

$$\alpha_1 = \sin\theta\cos\phi \tag{2.39}$$
$$\alpha_2 = \sin\theta\sin\phi \tag{2.40}$$
$$\alpha_3 = \cos\theta \tag{2.41}$$

The anisotropy energy is then given by a power series with expansion coefficients K_0, K_1, K_2 etc.. The coefficients themselves have no direct physical interpretation, rather than being the result of a mathematical description. In principle, the symmetry properties of the lattice have to be reflected in the anisotropy [Kas05]. This typically reduces the amount of necessary coefficients strongly. For a cubic crystalline lattice for instance, the energy density is given by

$$\varepsilon_{\text{cryst}} = E_{\text{cryst}}/V = K_0 + K_1(\alpha_1^2\alpha_2^2 + \alpha_2^2\alpha_3^2 + \alpha_3^2\alpha_2^2) + K_2\alpha_1^2\alpha_2^2\alpha_3^2, \tag{2.42}$$

with sample volume V [Kas05]. The equation above can be further simplified for specific cases. For instance, if a thin film system with in-plane magnetization and easy axis for $\phi = 0$ is considered, the crystalline anisotropy is given by

$$E_{\text{cryst}}/V = K_0 + K\sin^2(2\phi), \tag{2.43}$$

with $K = K_1/4$ [Kas05]. In this work, the thin film systems have been prepared by sputtering. Sputtering typically leads to a polycrystalline grain structure, where each grain possess a random anisotropy orientation. Averaging over the hole sample, leads to a vanishing anisotropy. Nonetheless, the grains themselves can in principal possess an anisotropy [Get08], which can be considered in the theoretical calculations. Besides that, the used ferromagnet NiFe has no crystalline anisotropy even as single crystalline phase [Yin06].

2.4.2 Shape anisotropy

Of special importance for thin film systems and magnetic structures in the micrometer range is the shape anisotropy. Those systems have a small volume, but at the same time the dipole field generated by the magnetic moments is only decreasing with distance r^{-3}. That means that for a small system volume, the dipole moments on the surface are of important role for the dipole field, which is interacting with the magnetic moments inside the system. The dipole moments on the surface act like surface charges generating an internal homogeneous field, the demagnetization field $\vec{H}_{\text{demag}}$, and a stray field $\vec{H}_{\text{stray}}$ outside the sample [Kas05].
The demagnetization field created by the magnetization $\vec{M}$ of the sample is given for a homogeneous magnetization by

$$\vec{H}_{\text{stray}} = -\hat{N}\vec{M}, \tag{2.44}$$

where $\hat{N}$ is the demagnetization tensor, depending on the sample's geometry [Kas05]. The energy within the demagnetization field is given by

$$E_{\text{Shape}} = -\frac{1}{2}\mu_0 \int_{\text{Sample\_volume}} \vec{M} \cdot \vec{H}_{\text{stray}} \mathrm{d}V \tag{2.45}$$

Alternatively the energy can be calculated by the stray field $\vec{H}_{\text{S}}$ and the total volume $\mathbb{R}^3$:

$$E_{\text{Shape}} = \frac{1}{2}\mu_0 \int_{\mathbb{R}^3} \vec{H}_{\text{S}}^2 \mathrm{d}V. \tag{2.46}$$

It can be seen here, that the energy in the stray field minimizes if the stray field is minimized. For an infinite thin magnetic layer the shape anisotropy tends to align the magnetic moments parallel to the surface, leading to a vanishing stray field [Kas05]. Mathematically, the shape anisotropy energy density is given by

$$\varepsilon_{\text{Shape}}^{thinfilm} = -\frac{1}{2}\mu_0 M_{\text{s}}^2 \sin^2\Theta, \tag{2.47}$$

with saturation magnetization M_{s} and polar angle Θ [Kas05].
Reducing the lateral size of the film to a stripe with a width in the micrometer range, then the magnetization will point along the stripe. Further reducing the size to a square leads to a nonhomogeneous magnetization and therefore domain wall formation, as will be discussed

later. Furthermore, the calculation of the stray field becomes complex since the calculation of the demagnetization field is not possible analytically anymore. As will be discussed later the stray field is calculated numerically in the simulations enabling to simulate basically arbitrary geometries [Lel18].

2.4.3 Zeeman interaction

In an external field $\vec{H}$ all magnetic moments tend to align in that field, as can be seen by Equ. 2.12. In weak fields, other anisotropies are dominating, and the magnetic moments are not aligned with the field, when the field points away from the easy axis. This results in an energy increase given by

$$E_{\text{Zeeman}} = -\mu_0 \int_{\text{V}} \vec{M} \cdot \vec{H} \mathrm{d}\vec{r}, \tag{2.48}$$

with sample volume V and its magnetization $\vec{M}$ [Kas05].

2.4.4 Surface anisotropy

Besides the reduction of the stray field, a contradicting observation can be made for thin films. On surfaces the translation symmetry is broken and an additional surface anisotropy can be observed. For decreasing film thicknesses, the surface contribution become increasingly important. The surface anisotropy with constant k_{S} is pointing perpendicular to the surface. Energetically, this leads to additional energy term

$$E_{\text{Surface}}^{thin film} = k_{\text{S}} \sin^2 \Theta. \tag{2.49}$$

For $k_{\text{S}} < 0$, an in-plane orientation of the moments is preferred. But for $k_{\text{S}} > 0$ an out-of plane orientation is preferred and contradicting the shape anisotropy, which is preferring an in-plane magnetization [Kas05].
An effective anisotropy constant K_{eff} can be defined combining volume effects with anisotropy K_{Vol} and surface effects with K_{Surf} given by

$$K_{\text{eff}} = K_{\text{Vol}} + \frac{2K_{\text{Surf}}}{t}, \tag{2.50}$$

with layer thickness t. The factor 2 is taking the two surfaces of the layer into account. It can be seen, that for a critical thickness t_{crit} the easy axis is switching from an in-plane orientation to an out-of-plane orientation, if $K_{\text{Surf}} > 0$. [Kas05].
In this work, only systems with an in-plane easy axis and magnetization are considered. Therefore, the surface anisotropy can be neglected in the simulations.

2.4.5 Futher anisotropies

A further anisotropy can be induced by the sputtering process itself. Therefore, an in-plane magnetic field needs to be applied while the layers are sputtered. The orientation of the field is then setting the uniaxial anisotropy [Mer20].
Typically, after sputtering the film possess a polycrystalline structure. Each grain has its own anisotropy direction, since the orientation of the lattice is undefined. Averaged over the hole layer, the total anisotropy is vanishing leading to no magnetocrystalline anisotropy. By applying a magnetic field in the sputtering process, the lattice orientation is aligning on the external field and therefor resulting in an uniaxial anisotropy along the field [Mer20].
In the simulations, the FM layer is considered crystalline for simplicity. The vanishing or only small magnetocrystalline anisotropy is then modeled with an anisotropy constant K_1 only having values below $2000\,\mathrm{J/m^3}$.

2.5 Domains and magnetic reversal processes

As discussed in the last chapter, magnetic moments align themselves in order to minimize the total free energy. A uniform magnetization is leading to large stray fields on the boundaries of the sample. Therefore, usually a non-uniform magnetization is energetically preferred [Kas05]. In Fig. 2.6 the stray fields are visualized. As it can be seen, the magnetization is split into regions of opposing magnetization. Regions of uniform magnetization are called domains. Different domains are separated by domain walls, where the magnetization is changing. Since the magnetization is changing in the domain walls, neighboring spins are non-parallel to each other and rotated away from their easy axis. Therefore, domain wall formation is energetically unfavorable. All in all, a equlibrium between stray field energy and domain wall energy is reached to minimize the total energy [Kas05].

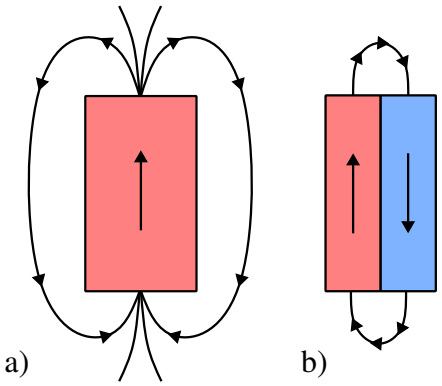

Figure 2.6: Simplified visualization of stray fields resulting from a uniform magnetization (a) and a two-domain state (b). A uniform magnetization leads to larger stray fields on the sample boundaries, while multiple domains reduce the stray field. Between the domains, domain walls are formed. Adapted from [Kas05].

2.5.1 Domain walls

Forming domains lead to a reduction of stray fields. Naively, one would expect that as many domains as needed to completely avoid stray fields would built up. However, domain wall formation requires energy, leading to an equilibrium state between domain wall energy and stray field energy [Kas05, Sto06].
First, the exchange interaction between neighboring spins is increasing with the enclosed angle between the spins. A complete 180 degree angle results in an exchange energy of

$$E_{\mathrm{ex}}^{1} \approx \frac{\pi^2}{a^2} J_{\mathrm{ex}} S^2, \tag{2.51}$$

with lattice constant a, exchange coupling J_{ex} and spin moment S [Sto06]. A 180 degree rotation along N spins results in a reduced energy of

$$E_{\mathrm{ex}}^{N} \approx \frac{\pi^2}{a^2 N} J_{\mathrm{ex}} S^2. \tag{2.52}$$

Given the wall width $w = N \cdot a$, the exchange energy reads

$$E_{\mathrm{ex}}^{w} = \frac{\pi^2}{wa} J_{\mathrm{ex}} S^2. \tag{2.53}$$

Second, if there is an anisotropy K_1 present, it takes energy to rotate spins away from there easy axis. For a domain wall with length w the anisotropy energy is given by

$$E_{\mathrm{ani}}^{w} = K_1 w. \tag{2.54}$$

The total domain wall energy reads

$$E_{\mathrm{tot}}^{w} = E_{\mathrm{ex}}^{w} + E_{\mathrm{ani}}^{w} = \frac{\pi^2}{wa} J_{\mathrm{ex}} S^2 + K_1 w. \tag{2.55}$$

The minimum of E_{tot}^{w} is defining the wall width and is calculated by

$$w = \sqrt{\frac{S^2 \pi^2}{a}} \cdot \sqrt{\frac{J_{\mathrm{ex}}}{K_1}} \tag{2.56}$$

Materials with a small anisotropy possess larger domain walls than materials with a high anisotropy [Kas05, Sto06].
Domain walls can be further characterized by the spins rotation. The rotation can take place by in-plane rotation or by out-of-plane rotation. In-plane rotation leads to Néel walls, while a wall with out-of-plane rotation is called Bloch wall [Kas05]. In Fig. 2.7 the two wall types

are visualized. Depending on the geometry of the sample, one of the two types is energetically

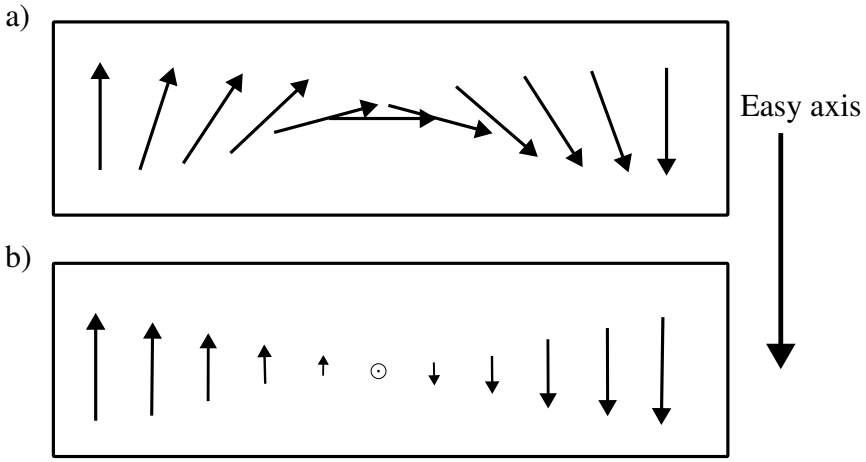

Figure 2.7: Visualization of Nèel (a) and Bloch walls (b). In Nèel wall type domain walls, the spins rotate in-plane. In Bloch walls, the spins rotate out-of-plane. Adapted from [Kas05].

preferred. In bulk materials, Bloch type walls are preferred, but for thin layers, Bloch walls lead to large stray fields, since the rotated spins obey an out-of-plane component. Therefore, in thin layers Nèel type domain walls are energetically preferred [Kas05].

2.5.2 Magnetization reversal

The magnetic reversal within a hysteresis loop can take place via different effects. Fast magnetic changes along the easy axis take place via nucleation. Along the hard axis, coherent rotation is responsible for gradually changing magnetization. Another magnetization reversal process is domain wall motion [Kas05].

Nucleation

Nucleation refers to the flipping of single magnetic spin. These spins are then seeds for further spin flips, building a magnetic domain droplet of increasing size. The process typically takes place all over the sample and different droplets are combining as they increase their size. In the hysteresis loop this can be seen by fast magnetization changes and is typical for remagnetization along the easy axis.

Coherent rotation

Coherent rotation states that the magnetization stays uniform during the reversal, but the direction is rotating until the magnetization points along the external field. This process is often encountered when the external field points along the hard axis. In the hysteresis loop, this reversal process can be determined by the gradual change of the magnetization [Kas05].

Domain wall creation and motion

Domain wall creation and motion is connected to nucleation. After the creation of a domain droplet, the droplet is growing and remagnetizing a part of the sample. The created domain wall is moving across the sample until it is fully magnetized.

2.6 Exchange bias

The exchange bias (EB) effect is a well known interface effect between FM and AFM interfaces and is originating from the interaction between the interface FM and AFM moments [Rad08]. The effect has been first observed by W. H. Meiklejohn and C. P. Bean in 1956 [Mei56]. They measured hysteresis curves of fine cobalt particles. Interestingly the curve was shifted horizontally and possessed higher coercive fields if the particles have been cooled from above their Nèel temperature T_N in an external field to 77 Kelvin. The process is called field cooling (FC) and will be explained below. They described this shift as an unidirectional anisotropy with anisotropy constant K_x. Macroscopically this anisotropy shifts the external field into the anisotropy direction. In general the effect appears on interfaces between FM and AFM materials [Rad08]. In the experiment of W. H. Meiklejohn and C. P. Bean, the surfaces of the cobalt particles were oxided and since cobaltoxid is an AFM the effect could be observed after FC.
EB systems are characterized by their EB field of strength H_{EB} and their coercive field H_C. Both can be determined in a hysteresis measurement by the fields $H_{C,1}$ and $H_{C,2}$ as indicated in Fig. 2.8. The EB field given by

$$H_{EB} = \frac{H_{C,1} + H_{C,2}}{2} \tag{2.57}$$

and the coercive field is given by

$$H_C = \frac{H_{C,1} - H_{C,2}}{2}. \tag{2.58}$$

Phenomenologically, the effect can be understood by a coupling between uncompensated and fixed AFM moments, which possess a small net magnetization, and the FM interface spins. The effect is established, for instance, by the FC process (see Fig. 2.8). After the fabrication of the EB system, the AFM moments are typically randomly oriented, leading to a vanishing EB field. By using FC, the AFM moments are oriented into one direction, resulting in a unidirectional EB effect. In the FC process, the system is first heated above the Néel temperature T_N of the AFM. At that temperature the AFM is in a paramagnetic state. At the same time, an external field is applied to saturate the FM spins into the field direction. By cooling through the Néel temperature, the AFM moments align to the interface spins of the FM. Thereby, a unidirectional anisotropy is created. Besides the EB field also an increase in the coercive fields can be observed compared to the unbiased system.

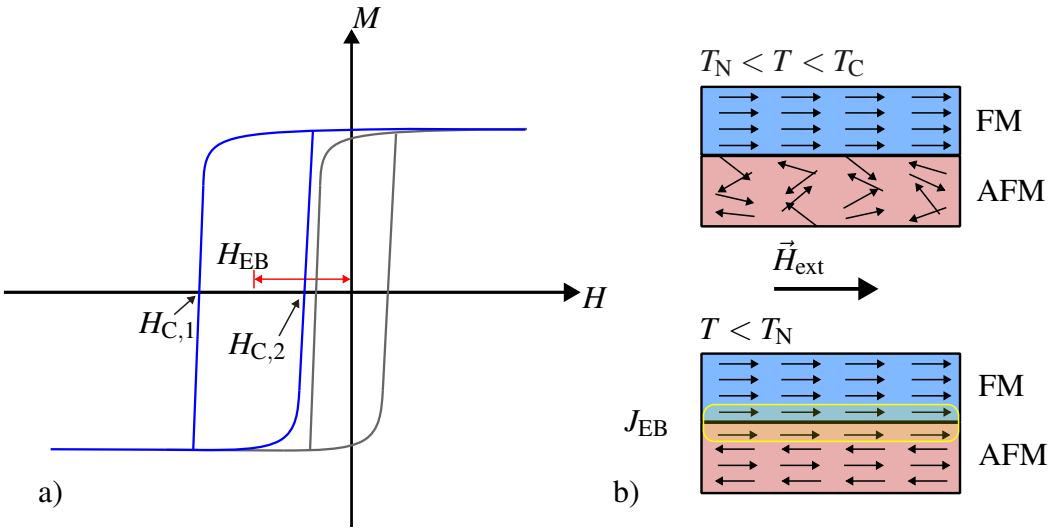

Figure 2.8: a) Two hysteresis loops are shown. In grey, a hysteresis loop of an unbiased system is sketched, while in blue an EB is present. The loop is characterized by the EB field H_{EB} and the coercive fields $H_{C,1}$ and $H_{C,2}$. b) Visualization of the FC process.

2.6.1 General properties of exchange bias

Before a closer look on the simulations is taken, an overview about general properties of EB systems will be given. Since this work is focusing on thin film systems, the influence of the layer thickness will be discussed first. Followed by the so-called training effects and the asymmetry of the hysteresis loop. Those three effects are of special interest here, because they are also reproduced and supported by the simulation presented later. Besides that, EB systems show dependencies on experiential conditions like the temperature and the fabrication process of the system itself. Here, the influence of the sputter parameters will be presented shortly.

Layer thickness dependencies

Experimentally, a dependence of the EB on the layer thicknesses both of the FM and the AFM can be observed. The EB field H_{EB} typically shows a $1/t_F$ dependence, where t_F is the layer thickness of the FM [Rad08]. For a Co/CoO system even at low thicknesses down to 2 nm this dependence could be observed experimentally [RES03]. Experimental deviations with other materials at that thickness are explained by discontinuous layers. Also for thick layer with some hundred nm thickness deviation could be observed. Here, it is assumed that domain wall formation leads to the observed deviations [Rad08].

The layer thickness of the AFM layer shows a more complicated dependence. Below a critical thickness the EB is vanishing. For CoFe/IrMg systems, the critical thickness is at about $t_{AFM,crit} = 5$ nm [Mer22b]. For increasing thicknesses, the EB strength is rapidly increasing to a maximum. Even thicker layers result in a plateau of the EB strength [Nog99, Mer22b]. The vanishing of the EB for thin layers below the critical thickness can be understood by a depinning of the AFM moments. For strong coupling, meaning $K_{AFM} t_{AFM} \leq J_I$, AFM moments follow the

FM and do not establish an EB [Nog99]. Thereby is K_{AFM} the anisotropy of the AFM and J_{I} the exchange coupling constant between the AFM and the FM. In Sec. 5.1.2 simulation result investigating this dependence will be presented.

Training effects

The decrease of the EB strength H_{EB} over sequential hysteresis cycles is referred to training effects. In the coercive field H_{C} the decrease is also present. Here, two types of training effects can be distinguished. First, type I when $|H_{\mathrm{C},1}|$ is decreasing and $|H_{\mathrm{C},2}|$ is increasing and second, type II when $|H_{\mathrm{C},1}|$ and $|H_{\mathrm{C},2}|$ are decreasing [Zha02]. A simple empirical law for $H_{\mathrm{EB}}(n)$, where n is the cycle number, states for $n > 1$

$$H_{\mathrm{EB}}(n) = H_{\mathrm{EB}}^{\mathrm{inf}} + \frac{k}{\sqrt{n}}, \tag{2.59}$$

with k being an experimental constant and $H_{\mathrm{EB}}^{\mathrm{inf}}$ being the limit of the EB strength for $n \to \mathrm{inf}$. This expression is in good agreement with experiments for $n > 1$. Training effects for $n > 1$ are called thermal training effects. In general, irreversible changes in the AFM domain are suspected to be responsible for the effect. The thermal training effect depends further on the temperature, since higher temperatures lead to faster reductions [Rad08]. The reduction of the EB strength in the very first cycle ($n = 1$) is independent on the temperature and is therefore called athermal training effect. Besides the empirical expression given in Equ. (2.59), recursive expression are able to capture the decrease in the first cycle as well. Binek [Bin04] found a possible recursive expression to be

$$H_{\mathrm{EB}}(n-1) - H_{\mathrm{EB}}(n) = -\Gamma(H_{\mathrm{EB}}(n) - H_{\mathrm{EB}}^{\mathrm{inf}})^3 \tag{2.60}$$

with physikal parameter Γ.
Simulation on the basis of the Stoner-Wohlfarth model as well as micromagnetic simulation have been performed in the past to investigate possible sources of training effects [Rad08, Cle17]. To summarize their results, one can state that rotations of AFM moments lead to a reduction of the EB. Because the rotated moments do not recover even in saturation, the number of rotated moments increase with increasing hysteresis cycles [Rad08]. These results have also been supported by experimental results based of example on Kerr microscopy [Rad08].
In [Cle16] a micromagnetic model is presented that also builds up the foundation of the simulations presented here. The model is assuming a polycrystalline AFM structure and has been used to simulate athermal training effects, indicating irreversible rotations of some AFM grains. Their results will be used as reference for the simulations performed in this work.

Asymmetry of hysteresis loop

In some experimental studies, an asymmetry in the hysteresis loop could be observed [Rad08]. Asymmetry means that the shape of the descending and the increasing hysteresis branch have a different shape. The origin of the asymmetry can be separated into two different groups. First, asymmetry due to an angle between the external field and the EB direction, which is an intrinsic property of EB systems. Second, asymmetry even in parallel field directions, but with instabilities in the AFM layer connected to the training effect. A short overview about both cases will be given. Further information can be found in [Rad08].
Characteristic for the first type of asymmetry is the fact, that the asymmetry occurs only if there is a small angle between the external field and the EB direction. In the hysteresis, the asymmetry leads to different shapes of the hysteresis branches. For instance, a more extended decreasing branch can be observed, due to a so-called exchange spring [Kim05]. Or, the decreasing field branch (DFB) is much sharper or steeper than the increasing one [McC03]. Especially in the perpendicular magnetization, the asymmetry can be clearly seen and characterized [Cam05]. In [Cam05] the different heights of the peaks in the perpendicular magnetization are used to quantify the asymmetry of the hysteresis loop:

$$\xi = \frac{M_{\mathrm{perp},1} - M_{\mathrm{perp},2}}{M_{\mathrm{S}}}, \tag{2.61}$$

with peaks $M_{\mathrm{perp},1}$ and $M_{\mathrm{perp},2}$ of the perpendicular magnetization and saturation magnetization M_{S} and will be applied to the simulation results in later chapters. The degree of asymmetry depends thereby also on the angle between external field and FC direction [Cam05, Til08]
Besides that, different magnetization reversal processes in the different hysteresis branches could be observed. In [Fit00] coherent rotation was observed on the DFB, while on the increasing field branch (IFB), domain wall nucleation and motion was observed. Opposed to that, in [McC03] the opposite is the case and domain wall motion on the DFB and coherent rotation on the IFB could be observed.

Further dependencies

To end this section, a few further properties are given, which are not investigated in this work. The magnitude of the EB field depends on the temperature at which the experiment is carried out [Rad08]. At low temperatures, a stronger EB field can be observed. While for increasing temperature the EB effect is decreasing and for temperature above the blocking temperature even vanishing. The reason can be found in the AFM layer and its increasing instability with increasing temperature [Rad08]. The simulations performed here are assuming a temperature of 0 K.
Even though the EB effect is mostly an interface effect, the bulk of the AFM also plays a cer-

tain role. In [Bas14] it has been shown that the creation of defects in the AFM bulk influences the EB strength, indicating that not only interface moments need to be considered in the understanding of the EB effect. In the simulations presented here, only interface moments are considered, neglecting the influence of the bulk AFM. This simplification is connected to the fact, that it is not possible to correctly simulate an AFM on an atomistic level with micromagnetic simulations [Cle16, Cle17].
Of important role is further the fabrication of the system. First, strong differences in the used fabrication technique can be found, as it can be seen in Tab. I in [Rad08]. Second, the used parameters in the fabrication process also play an significant role. For instance, the grain size distribution of the polycrystalline AFM after sputtering depends on the parameters in the sputter process and influence the EB field significantly. [Mer20, Mer22a, Mer22b].

2.7 Modeling

The aim of this thesis is the modeling of magnetization reversal processes in exchanged bias thin film geometries. Before a detailed description of the model is given, a general overview over two different modeling approaches will be given. First, there is the simple model of Stoner and Wohfarth [Sto47, Sto91]. By assuming a uniformly magnetized ferromagnet a simple description of the different energy contribution can be found. Unfortunately, the assumption of an uniformly magnetized ferromagnet is in many cases of a magnetization reversal not realistic, as other magnetization reversal process, like nucleation or domain wall motion, are neglected. The second approach is known as the micromagnetic formulation. Here, the magnetization is described by a continuous vector field. The formulation is way more mathematically involving, but allows to investigate nucleation and size effects of the geometry, e.g. shape anisotropy [Abe19]. Since size effects are of important role and also nucleation needs to be investigated, the model used here will be the micromagnetic formulation.

2.7.1 Stoner-Wohlfarth model

Stoner and Wohlfarth [Sto47, Sto91] are assuming that the magnetization of the ferromagnet is given by a vector $\vec{M}_\mathrm{F}$ of constant length M_F. This allows to neglect the exchange interaction between the magnetic moment. All moments are aligned parallel, resulting in a uniform magnetization. Since M_F is constant, only coherent rotation can change $\vec{M}$. As already discussed, the magnetization is governed by the minimization of the free energy. In the basic model, the magnetization is interacting with an external field $\vec{H}$ via Zeeman interaction and only an uniaxial anisotropy K_F is present. In Fig. 2.9 the different components are visualized.
For an infinitely extended thin film with in-plane magnetization, layer thickness t_F, saturation

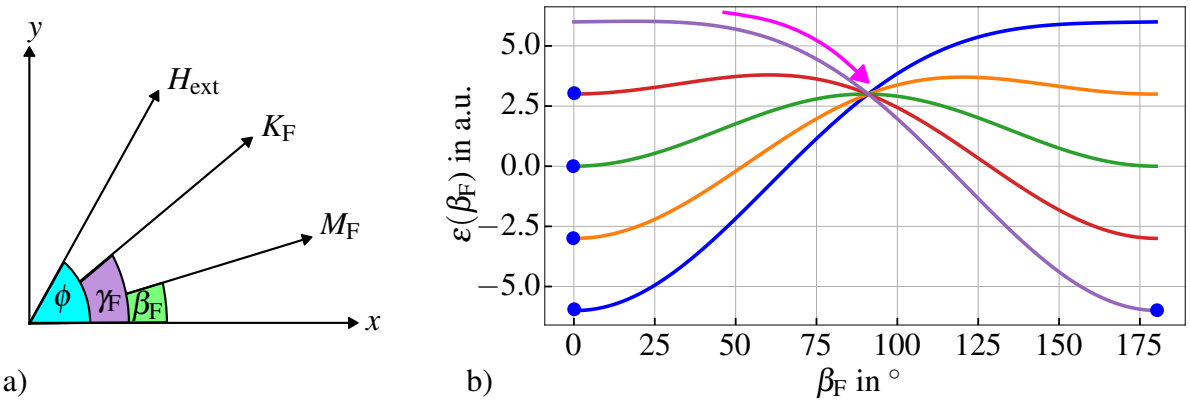

Figure 2.9: a) Visualization of the Stoner-Wohlfarth model with a given reference frame. Further, the magnetization $\vec{M}_F$, anisotropy K_F and the external field H_{ext} are shown. Each component possesses an angle β_F, γ_F, and ϕ with the reference frame. Adapted from [Mer22a]. b) An example energy landscape for different external fields is shown. Depending on the field strength (decreasing from blue to purple), the global minimum and the possible local minimum are separated by an energy barrier. The magnetization (blue dot) is flipping if the energy barrier is vanishing (purple curve).

magnetization M_F^S and uniaxial anisotropy K_F, the area energy density ε is given by

$$\varepsilon(\beta_F) = -\mu_0 H M_F^S t_F \cos(\beta_F - \phi) + K_F t_F \sin^2(\beta_F - \gamma_F). \tag{2.62}$$

The first term is giving the zeeman interaction between $\vec{H}$ and $\vec{M}_F$ (see 2.4.3) and the second term describes the uniaxial anisotropy (see 2.4.1). The angles are defined in Fig. 2.9 and describe the orientation in a chosen reference frame. The magnetization direction is obtained by minimizing ε in dependence of β_F [Mer22a].

In Fig. 2.9 the energy landscapes for different external fields (decreasing from blue to purple) are illustrated. For strong external fields, the Zeeman energy is dominating and only one energy minimum is possible (blue and purple curve). In this case, the magnetization is parallel to the external field. For a decreasing field strength, a second local minimum can be found (red, orange and green curve). This local minimum describes the antiparallel orientation and corresponds to the other hysteresis branch. As the external field is further reduced, the global minimum becomes a local minimum and the local minimum becomes the global minimum (red curve), both separated by an energy barrier. This energy barrier keeps the magnetization in its own minimum. As soon as this energy barrier is vanishing, the magnetization rotates to align with the field (purple curve) [Mer22a]. Increasing the field again, the process is reversed, but the magnetization is following the other energy minimum, leading to a hysteresis loop.

The number of possible orientations can also be found by the Stoner-Wohlfarth asteroid. The external field is split into a parallel component $H_{\parallel}$ and a perpendicular component $H_{\perp}$ to the

easy axis of the sample [Rad08]. The asteroid then yields

$$\left(\frac{H_{\parallel}}{A}\right)^{2/3} + \left(\frac{H_{\perp}}{A}\right)^{2/3} = 1, \text{ with } A = \frac{2K_{\mathrm{F}}}{\mu_0 M_{\mathrm{F}}^{S}}. \tag{2.63}$$

In Fig. 2.10 the asteroid is visualized. Depending on the external field (blue arrow) there are one or two possible magnetizations. If the external field vector lays within the asteroid, then there are two possible magnetization directions and the actual directions depend on the history as described above. For field vectors ending outside of the asteroid, only one magnetization direction is possible [Rad08].

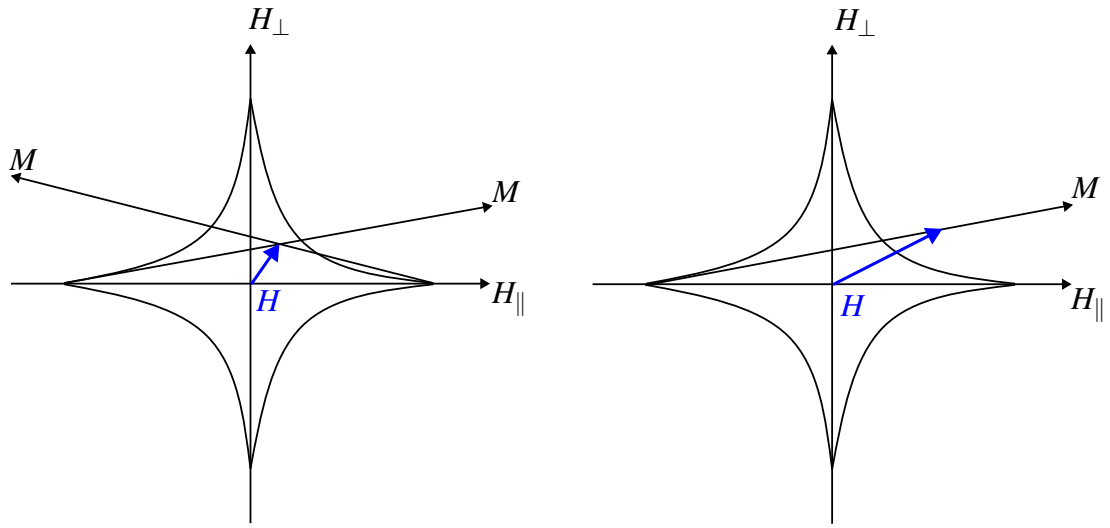

a) b)

Figure 2.10: Visualization of the Stoner-Wohlfarth asteroid. a) Only a weak external field in present and two possible magnetization directions are indicated. One for the local minimum and one for the global minimum in the energy landscape. b) A strong field is present. Energetically, only one global minimum is present. Adapted from [Rad08].

2.7.2 Micromagnetic formulation

In the model of Stoner-Wohlfarth the magnetization is described by a single vector. The ferromagnet is assumed to be uniformly magnetized, and remagnetization only takes place by coherent rotation. In micromagnetics the magnetization is described by a continuous vector field $\vec{M}$. At each point in space the vector field is of equal length to the saturation magnetization meaning $|\vec{M}(\vec{r})| = M_{\mathrm{S}}\ \forall \vec{r} \in V$, where V is the investigated volume. For simplification, a normalized vector field $\vec{m} = \vec{M}/M_{\mathrm{S}}$ with $|\vec{m}(\vec{r})| = 1\ \forall \vec{r} \in V$ is defined and called magnetization. Within the formulation of micromagnetics lays the possibility to include more effects, like FM exchange interaction. At the same time, working with classical expectation values makes micromagnetism a semiclassical theory [Abe19, Lel18].
In order to compute the magnetization $\vec{M}$ correctly, all energy contributes need to be considered.

From the total energy an effective field can be calculated, which in then used in the Landau–Lifshitz–Gilbert equation to calculate the time derivative of $\vec{m}$ [Van14]. In the following, the required energy terms are presented.

Exchange energy

The exchange interaction describes the interaction between two neighboring spins. As already discussed, the energy density in the Heisenberg picture is given by

$$\varepsilon_{\mathrm{ex}} = J_{\mathrm{ex,ij}} \vec{S}_{\mathrm{i}} \cdot \vec{S}_{\mathrm{j}}, \tag{2.64}$$

for two neighboring spins $\vec{S}_{\mathrm{i}}$ and $\vec{S}_{\mathrm{j}}$. In the micromagnetic formulation the interaction reads

$$\varepsilon_{\mathrm{ex}} = A_{\mathrm{ex}} (\nabla \vec{m})^2, \tag{2.65}$$

with exchange stiffness A_{ex} and is the result of the continuum limit of micromagnetism [Abe19, Lel18]. In order to calculate the total exchange energy, the energy density needs to be integrated over the simulation volume V. In total, the exchange energy reads

$$E_{\mathrm{ex}}(\vec{m}) = A_{\mathrm{ex}} \int_{\mathrm{V}} (\nabla \vec{m})^2 \mathrm{d}\vec{r}. \tag{2.66}$$

Zeeman energy

The Zeeman energy is the result of the interaction between the external field $\vec{H}$ and the magnetization $\vec{M}$ of the sample. The total zeeman energy is given by [Abe19, Lel18]

$$E_{\mathrm{Z}}(\vec{m}) = -\mu_0 \int_{\mathrm{V}} \vec{M} \cdot \vec{H} \mathrm{d}\vec{r}. \tag{2.67}$$

Magnetostatic energy

The magnetostatic energy is the energy resulting from the magnetization with the field created by the magnetization itself. It is given by [Abe19, Lel18]

$$E_{\mathrm{demag}}(\vec{m}) = -\frac{\mu_0}{2} \int_{\mathrm{V}} \vec{M} \cdot \vec{H}_{\mathrm{demag}} \mathrm{d}\vec{r}, \tag{2.68}$$

with demagnetizing field $\vec{H}_{\mathrm{demag}}$. The demagnetization field is given by

$$\vec{H}_{\mathrm{demag}}(\vec{m}) = \frac{M_{\mathrm{S}}}{4\pi} \int_{\mathrm{V}} 3 \frac{(\vec{m} \cdot \vec{r})\vec{r}}{r^5} - \frac{\vec{m}}{r^3} \mathrm{d}\vec{r}. \tag{2.69}$$

As already discussed, the magnetostatic energy results from dipole-dipole interaction and is weak compared to the exchange interaction, but is acting on much larger distances. The results are the formation of domains. The big advantage of micromagnetic simulations is therefore

the possibility to simulate domain formation. Nonetheless, the calculation of the magnetostatic energy is computationally involving and results in much longer computation times compared to the Stoner-Wohlfarth model.

Crystalline anisotropy energy

The last important energy contribution results from the crystalline anisotropy. As discussed before, in some materials exists an easy axis, originating from the interaction between the magnetic moments and the atomic lattice. From symmetry considerations it is known that the energy E_{ani} is uniaxil, meaning

$$E_{\mathrm{ani}}(\vec{m}) = E_{\mathrm{ani}}(-\vec{m}). \tag{2.70}$$

For the simple case of a single easy axis in $\vec{e}_{\mathrm{u}}$ direction, a phenomenological energy expression is given by

$$E_{\mathrm{ani}}(\vec{m}) = \int_{\mathrm{V}} K_{\mathrm{u},1}(\vec{m}\cdot\vec{e}_{\mathrm{u}})^2 + K_{\mathrm{u},2}(\vec{m}\cdot\vec{e}_{\mathrm{u}})^4 + \mathscr{O}(\vec{m}^6)\mathrm{d}\vec{r}, \tag{2.71}$$

with anisotropy constants $K_{\mathrm{u},1}$ and $K_{\mathrm{u},2}$ [Abe19]. Because of symmetry reasons only even powers need to be considered. In many cases the first two or even only the first order needs to be taken into account for precise results. The energy expression given above is typical for hexagonal or tetragonal crystal structures. For materials with a body-centered structure, a phenomenological energy expression is given by

$$E_{\mathrm{ani}}(\vec{m}) = \int_{\mathrm{V}} K_{\mathrm{c},1}(m_1^2m_2^2 + m_2^2m_3^2 + m_1^2m_3^2) + K_{\mathrm{c},2}m_1^2m_2^2m_3^2\mathrm{d}\vec{r}, \tag{2.72}$$

with cubic anisotropy constants $K_{\mathrm{c},1}$ and $K_{\mathrm{c},2}$ [Abe19].

Static energy minimization

The listed energy contributions are the only ones that are considered in this work. Besides them, for example antisymmetric exchange energy or interlayer-exchange energy can be included [Abe19]. All energy contributions are then summed up to a total energy

$$E(\vec{m}) = E_{\mathrm{ex}}(\vec{m}) + E_{\mathrm{Z}}(\vec{m}) + E_{\mathrm{demag}}(\vec{m}) + E_{\mathrm{ani}}(\vec{m}) \tag{2.73}$$

representing the total energy in dependence of the magnetization $\vec{m}$. In order to calculate the static magnetization, $E(\vec{m})$ needs to be minimized. In [Abe19] and [Lel18] a detailed deviation of the necessary minimization condition is given. To summarize, an effective field $\vec{H}_{\mathrm{eff}}$ can be calculated by the functional derivative of the total energy E:

$$\vec{H}_{\mathrm{eff}} = \frac{-1}{\mu_0 M_{\mathrm{S}}}\frac{\delta E}{\delta \vec{m}}. \tag{2.74}$$

The effective field is then used in the equation of motion of $\vec{m}$, given by

$$\dot{\vec{m}} = -\vec{m} \times (\vec{m} \times \vec{H}_{\text{eff}}). \tag{2.75}$$

The energy is minimized if $\vec{m}$ is a constant in time. Following [Abe19] this is the case if and only if

$$\vec{m} \times \vec{H}_{\text{eff}} = 0, \tag{2.76}$$

which is the final condition to find the energy minimum. In this work, only static energy minimization will be used, since we are only interested in static problems like the calculation of hysteresis loops.

Dynamic micromagnetics

For the seek of completeness also dynamic micromagnetics are briefly introduced. The equation used for dynamic simulations is called Landau-Lifshitz-Gilbert (LLG) equation [Lan35]. The effective field $\vec{H}_{\text{eff}}$ is again used to calculate the time derivative of $\vec{m}$:

$$\dot{\vec{m}} = -\frac{\gamma}{1+\alpha^2}\left[\vec{m} \times \vec{H}_{\text{eff}} + \alpha \vec{m} \times (\vec{m} \times \vec{H}_{\text{eff}})\right]. \tag{2.77}$$

Here, γ is the gyromagnetic ratio of the electron and α is an phenomenological damping constant. The first term $\vec{m} \times \vec{H}_{\text{eff}}$ describes the precession of the magnetic moments around the field $\vec{H}_{\text{eff}}$. The second term describes the alignment in the field [Van14]. The damping constant is a phenomenological constant, introduced by Landau and Lifshitz [Lan35] and can be determined experimentally [Pap18] or calculated theoretically [Bar13]. For permalloy, it is $\alpha = 0.01$ for instance [Van14]. Setting a high damping parameter $\alpha = 1$ and neglecting the precession term, the LLG equation simplifies to the static minimization problem given in Equ. 2.75 [Van14].

3 Experimental background

This chapter aims to give an overview of the sample preparation and characterization methods used in connection with this work. The goal of the work was to simulate the experimental observations in magnetic reversal processes of different exchange bias (EB) geometries, like stripes, squares, and discs. To understand certain simulation approaches, background knowledge of the sample preparation and the magnetic characterization is required. Besides that, atomic force microscopy and vibrating sample magnetometry (VSM) were used to manifest simulation results experimentally.

3.1 Sample preparation

The samples used in this work are thin film multilayer systems. In Fig. 3.1 a schematic of the samples is given. The samples consist of four layers fabricated by sputtering. First, a buffer layer of 5 nm Cu is deposited. The EB system consists of a 30 nm $Ir_{17}Mn_{83}$ layer acting as the antiferromagnetic (AFM) layer, followed by 10 nm of a ferromagnetic (FM) $Ni_{81}Fe_{19}$ layer. To protect the system from oxidation, an Al top layer of 3 nm is deposited.

The investigated sample geometries can also be seen in Fig. 3.1. In summary, there are three different geometries: stripes, squares, and discs. The spacing between the geometries is equal

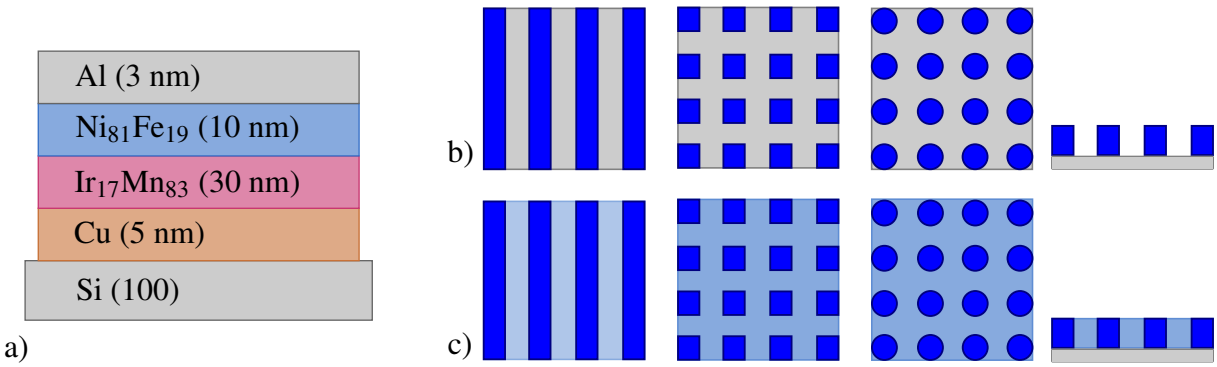

Figure 3.1: a) Sketch of the layer system. On top of a silicon substrate and a buffer layer, the actual EB system consisting of IrMn and NiFe is sputtered, followed by a top layer of Al. b) Visualization of the freestanding stripes, squares, and discs. c) Visualization of the embedded geometries. The bombarded area is shown in light blue, while the actual geometries are given in blue.

to their width. Besides that, the three geometries can be separated into freestanding geometries and embedded geometries. The freestanding geometries have been sputtered with a lithographic resist pattern on top of the silicon substrate, which is removed in a subsequent lift-off process, leading to freestanding topographic stripes. The embedded stripes are fabricated by ion bombardment (IB). After the deposition, a mask is lithographically put on top of the system to protect the stripe's area, defined by the resist pattern. The uncovered and therefore unprotected areas are bombarded with an ion dose high enough to destroy the EB effect. By this, within the layer system the embedded stripes are created and a flat surface is obtained. The other geometries are fabricated in a similar way, but electron beam lithography has been used instead.

3.1.1 Sputtering

Sputtering describes the process by which a thin layer of a target material is deposited on a substrate, by using a plasma to evaporate the target material. A basic schematic of the working principle can be found in Fig. 3.2. The used technique is called high-frequency sputtering. Here, a Leybold Heraeus Z400 was used. Between an anode - the target - and a cathode - the sample - a high-frequency voltage with a frequency of $f = 13.56\,\mathrm{MHz}$ is applied. The voltage in the sputtering process is usually between 500 V and 1500 V [Huc18]. In Tab. 3.1 the used voltages can be found. The working gas, in case of this work Argon, is ionized by the electric field, resulting in ions and electrons that are accelerated in the field, but only the light electrons reach the electrodes at first. Since the target is grounded via a capacitor, an effective DC-voltage is created by the impinging electrons that accelerates the Ar^+ towards the target. When the ions hit the target, their kinetic energy is transferred and target material is released [Huc18]. The released material impinges on the sample and a layer is growing over time. By changing the voltage, the kinetic energy of impinging ions is changed, and thereby the number of released atoms and clusters. For the samples the growth rates are below 10 nm per minute. The base pressure in the process chamber is in the order of $10^{-6}\,\mathrm{mbar}$ and an Argon gas flow of 140 sccm at a working pressure of $8 \cdot 10^{-6}\,\mathrm{mbar}$ is set. The polycrystalline structure of the deposited material strongly depends on the target material, the applied voltage, and the sample temperature [Mer22a]. Additionally, a magnetic field of $B_{\mathrm{sputter}} = 40\,\mathrm{mT}$ can be applied in-plane in relation to the sample leading to a defined uniaxial anisotropy of the material system. In table 3.1 the layer thicknesses and sputter rates can be found.

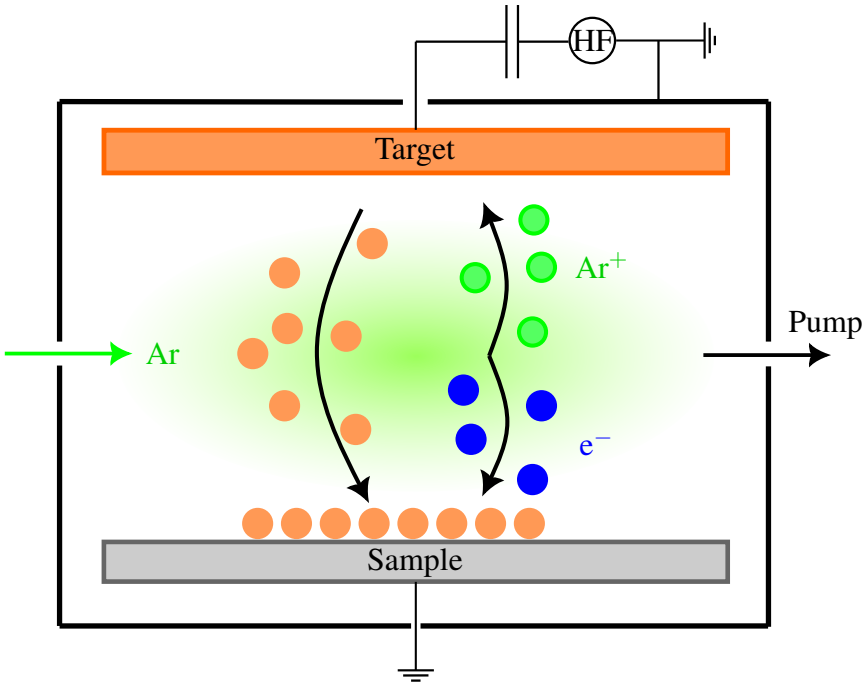

Figure 3.2: Schematic sketch of the sputtering process. Ions of the ionized working gas are accelerated and release atoms of the target material, which are then deposited on the sample. Adapted from [Mü16].

Table 3.1: Overview of the layer system and the sputter parameters for each layer.

material	thickness in nm	sputter rate in nm/min	DC voltage in V
Cu	5	6.21	600
$Ir_{17}Mn_{83}$	30	5.45	750
$Ni_{81}Fe_{19}$	10	3.88	600
Al	3	3.05	400

3.1.2 Field cooling

An important step in the preparation process is the initialization of the EB effect by field cooling (FC). After deposition, non or only a weak EB effect can be measured. The initialization is done by the so-called FC process, which establishes the unidirectional EB effect [Mei56]. In the field cooling (FC) process, the sample is heated to a temperature between the Nèel temperature T_N of the AFM IrMn and the higher Curie-temperature T_C of the FM NiFe. Thereby, the AFM occupies a paramagnetic state. In the presence of an external field, the sample is cooled down slowly. Since the ferromagnet is saturated in the homogeneous external field, the AFM interface moments align to the FM interface moments and freeze out when cooling down through the Nèel temperature [Mer22a]. In our case, a field of $H_{FC} = 115\,\mathrm{kA/m}$ for $t_{FC} = 60\,\mathrm{min}$ at a temperature of $T_{FC} = 300\,^{\circ}\mathrm{C}$ was applied.

3.1.3 Lithography

To fabricate the described geometries, optical lithography was used for structuring the patterned systems. In the case of the freestanding geometries, the lithography process was performed before sputtering, while the embedded geometries are sputtered first, and the lithography is used to protect the geometries from the IB as a shadow mask.
In general, by this process, a light-sensitive photoresist is spread homogeneously on the silicon wafer by spin coating. After cleaning the silicon wafer with acetone, isopropyl, the sample is dried in the hard-baking step. Next, a primer and the photoresist is placed on the sample and spread homogenously in a spin coater to form a thin layer. To harden the resist, the sample is heated in the soft-baking step. Afterward, a photomask, containing the desired pattern, is placed on top of the resist by a mask aligner and radiated by UV-light. The patterning of the photomask is thereby transferred to the photoresist. Those areas, which are radiated by UV-light, are modified by a photochemical reaction [Huc18]. Depending on the photoresist type, the radiated parts of the resist have an increased or decreased solubility. By using an alkaline developer, the parts with higher solubility are removed in the development process [Huc18]. After fabrication the remaining non-soluble parts are removed by immersing the resist in a strong, heated solvent. In Fig. 3.3 the two different processes are visualized. Since this thesis is focusing on the modeling of the systems, the precise parameters are not of interest here, but can be found in Appendix 7.1.

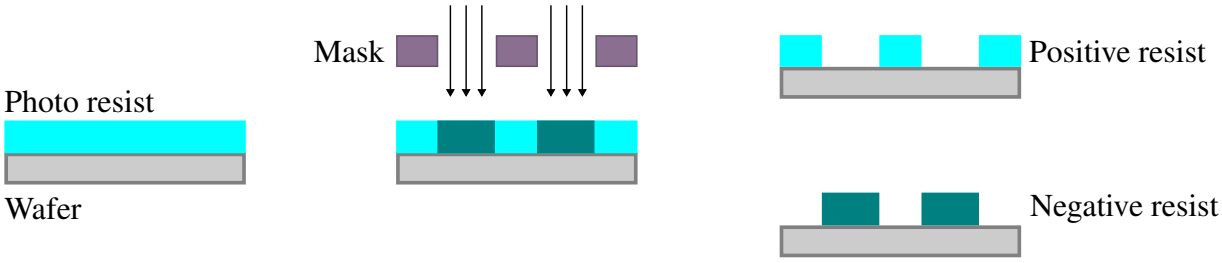

Figure 3.3: Simplified schematic showing the basic principal of optical lithography. A wafer is prepared with a photoresist. A photomask is protecting certain areas from being irradiated. Depending on the resist, a positive or negative image of the mask is created. Adapted from [Huc18].

With this technique the fabrication of structures with sizes of typically 1 µm is possible [Maa08]. The size is limited by the optical resolution limit, due to the diffraction of the UV-light [Maa08]. Alternatively, electron beam lithography (EBL) [Pea81] allows the creation of structures in the nm range [Tse03], by using a scanning electron beam to irradiate the photoresist instead of a mask and UV-light.

3.1.4 Ion bombardment

Ion bombardment (IB) of EB thin film systems is a powerful tool to initialize [Eng05], increase, weaken, or even invert [Ehr06, Mü18] the EB in a controlled manner. In combination with

lithography IB allows magnetic pattering in the micrometer range [Sch14], which can also be used as a possible lab-on-the-chip realization [Gau16].
In our home-built system, He^+ ions with a kinetic energy of about 10 keV are impinging on the sample surface, leading to two contradicting effects. First of all, hyperthermal heating allows grains in the AFM (see Chapter 4.2) to rotate from a local energy minimum into a global energy minimum given by an external field by overcoming an energy barrier. By this, the EB effect is increased or decreased depending on the direction of the external magnetic field [Ehr06]. The second effect accounts for the interfacial mixing of FM and AFM material on the interfaces or defect creation. This intermixing and the increased defect density lead to a decrease of the EB effect independently on the external field [Ehr06]. Of important roles are the ion dose and the direction of the external field. For low ion doses, the EB can be increased by aligning the external field in the EB direction. For increasing doses, the intermixing effect has a growing influence, reducing the EB independently of the external field.

In this work, the keV-He^+ IB was used to create the embedded geometries. Those areas of the thin film system representing the actual geometries were covered with a photoresist by UV-lithography to protect them from the bombardment. The unprotected area was bombarded with $2 \cdot 10^{16}$ ions/cm^2 in order to fully destroy the EB in those regions without an applied external magnetic field. In Fig. 3.4 a schematic of the used ion beam gun can be seen. In a Penning ion source, He^+ ions are created and afterwards accelerated towards the sample by an electric field. The beam is focused by electrostatic lenses and formed by an aperture. The aperture is used to make sure that the beam has a quasi-constant ion intensity across the beam. The ion beam is

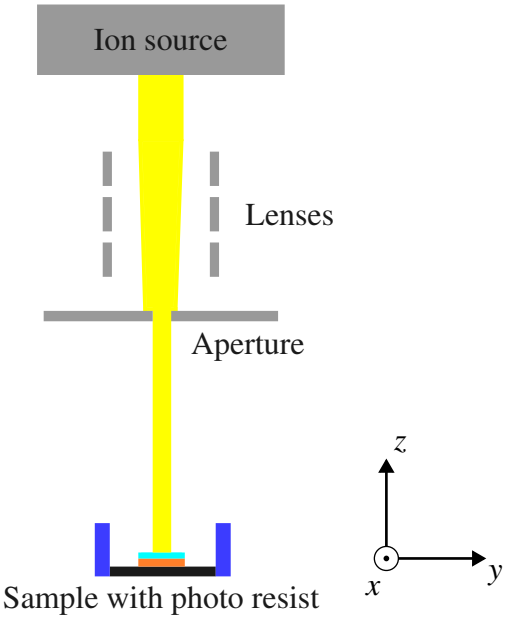

Figure 3.4: Simplified schematic of the used ion beam gun (ISA) adapted from [Gau17]. The ion source is followed by electrostatic lenses, which focus the ion beam (yellow) onto an aperture. The ion beam is then irradiating the sample. The sample itself is prepared with a photoresist, as described in Chap. 3.1.3.

scanned across the sample, whereby the movement in the x-direction is continuous and discrete in the y-direction [Gau17]. The ion dose D is then given by the ion current I, the speed of the aperture v, and the sample's x- and y-dimensions b and d as

$$D = \frac{I}{e \cdot v \cdot b}, \tag{3.1}$$

with electron charge e [Gau17]. Next to the sample, magnets can be placed allowing to have a magnetic field applied in the bombardment process.

3.2 Characterization Methods

The characterization of the samples was mainly done by three different techniques. The sample's surface and grain structure was investigated by atomic force microscopy. Saturation magnetization was measured by vibrating sample magnetometry (VSM) and the magnetization of the sample's surface, while measuring the hysteresis loop, was performed by Kerr microscopy. Each technique and the measurement's procedure will be explained briefly.

3.2.1 Atomic Force Microscopy

Atomic force microscopy is a technique to investigate the sample's surface topography of the sample by probing it with a tip. In close proximity to the surface, the tip is interacting with local attractive and repulsive forces. The deflection of the cantilever holding the tip is measured and thereby information about the interacting between tip and surface is gained. The cantilever is positioned by piezoelectronics. By scanning with the tip laterally across a defined area, a three-dimensional topography is measured. The deflection of the cantilever is measured by the reflection of a laser beam pointed on the cantilever and reflected to a four-element segmented photodiode. Important properties are the geometry, size, and condition of the tip and its precise positioning [Hol15, Huc18, Mer22a].
The tip's interaction with the surface can be approximated by the Lennard-Jones Potential

$$V(r) = \frac{C_\mathrm{r}}{r^{12}} + \frac{C_\mathrm{a}}{r^6}, \tag{3.2}$$

giving the potential energy in dependence of the distance r between tip and surface. The constants C_r and C_a are material parameters for the repulsive and attractive forces [Mes15]. In Fig. 3.5 the potential is shown. Near contact, the repulsive forces dominate, while for larger distances the attractive forces predominate. Attractive force are the result of van-der-Walls-forces, while Pauli exclusion principle leads to a repulsive force near the surface. Both forces can be used for three different measuring modes [Mer22a]. The repulsive forces are used in the so-called contact mode. In contact mode, the tip is touching the surface of the sample. When scanning across the surface, the tip is following the surface topography and the cantilever

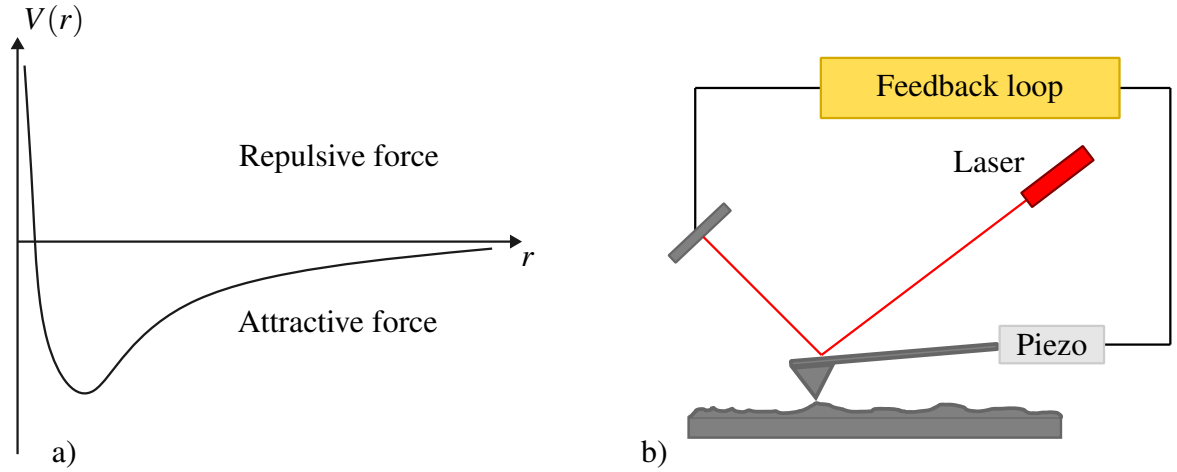

Figure 3.5: a) Visualization of the Lennard-Jones potential. Larger distances r between tip and surface result in attractive forces, while smaller r lead to repulsive forces. b) Schematic setup of an atomic force microscope can be seen. The deflection of the tip is measured by a reflected laser beam. A Feedback loop is then correcting the tip position by a piezo electronic. Adapted from [Mer22a].

is defected. Opposed to the contact mode, the non-contact mode is using the attractive force. Thereby, the tip in not in contact with the surface. In order to get topographical information of the surface, the tip is oscillating near the resonance frequency of the cantilever. Changes in the attractive forces lead to changes in the resonance frequency, the phase difference and amplitude of the oscillation. By adjusting the frequency to keep the amplitude constant, topological information of the surface is gained. A mixture of both modes is the intermittent mode. In this mode, the tip is oscillating, but the amplitude is high enough to touch the surface. In contact mode, the resolution is the highest of all three modes, but the tip wear is the highest, since the tip is touching the surface while moving. In the non-contact mode the tip is not touching the surface and the tip' lifetime is maximized, but also the resolution is reduced. The intermittent mode is therefore a compromise between both mods and their advantages [Mer22a].
Atomic force microscopy was used to investigate the grain structure on the IrMn layer. Samples were prepared without the two top layers, only consisting of 5 nm Cu and 30 nm IrMn, allowing to access the AFM layer physically. The question under consideration was whether there is a difference measurable between edge and middle part of the geometries in terms of grain size distribution. Further details are given in Chap. 5.2.1.

3.2.2 Vector Vibrating Sample Magnetometry

Vibrating sample magnetometry (VSM) is a technique to measure the magnetization and its direction of a sample. In this work, vector vibrating sample magnetometry (VVSM) is used to measure the saturation magnetization of the freestanding stripe geometries, and to investigate the influence of the stripe width on the saturation magnetization.
The working principle can be seen in Fig. 3.6. Two electromagnets are generating a homo-

geneous magnetic field. In the middle of the magnetic field, the sample is placed on a sample holder. The sample holder itself is vibrating in the z-direction. The vibration of the sample leads to an induction current in the nearby located pickup coils, which is proportional to the magnetic moment of the sample [Fra21]. The voltage in the coils is given by

$$V = m \cdot A \cdot f \cdot S, \tag{3.3}$$

with magnetic moment m, amplitude of the vibration A, frequency f and sensitivity S [Fra21]. The sensitivity S is determined by calibration with a probe of known magnetization at a given external field. An extension to the normal VSM is the VVSM, which has a rotatable sample holder and a further coil perpendicular to the sample [Fra21]. Thereby, the angular dependence of the magnetization can be measured as well. Measuring $m_{\parallel}$ and $m_{\perp}$ the magnetic moment is given by

$$m = \sqrt{m_{\parallel}^2 + m_{\perp}^2}. \tag{3.4}$$

For this work, a VVSM by MicroSense, for each direction (x and y) four pickup coils are used. This setup is known as the four-coil configuration by Mallinson [Mal66]. If the coils are appropriately balanced, a zero signal is produced in the absence of the sample. The coil size is a balance between sensitivity and size to minimize the influence of inhomogeneous field components. The sample is placed horizontally and in-plane to the external magnetic field (in-plane configuration). The x-coils are measuring the signal along the external field ($m_{\parallel}$), while the y-coils are measuring the signal perpendicular to the field ($m_{\perp}$). When rotating the sample and only considering the x-coil's signal, an angular depended hysteresis loop can be measured, revealing information about the easy- and hard-axis for instance. By changing the sample holder, the sample can be placed out-of-plane to the field, resulting in an out-of-plane signal [Fra21].

The external field can be varied by the electromagnets, resulting in the possibility to measure $m(H_{\text{ext}})$ in dependence of the external field H_{ext}. By measuring $m(H_{\text{ext}})$ for strong enough field from positive to negative saturation, a hysteresis loop can be measured and the saturation magnetization M_{S} determined. The magnetization M is the magnetic moment per volume V [Mes15]. Since only the magnetic moments can be measured directly, the magnetization needs to be determined by

$$M = \frac{m}{V}.$$

Here, it is assumed that the magnetization is uniform over the hole sample. This is the case in saturation, when all magnetic moments point into the same direction, what allows measuring the saturation magnetization by

$$M_{\text{S}} = \frac{m(H_{\text{ext,saturation}})}{V}.$$

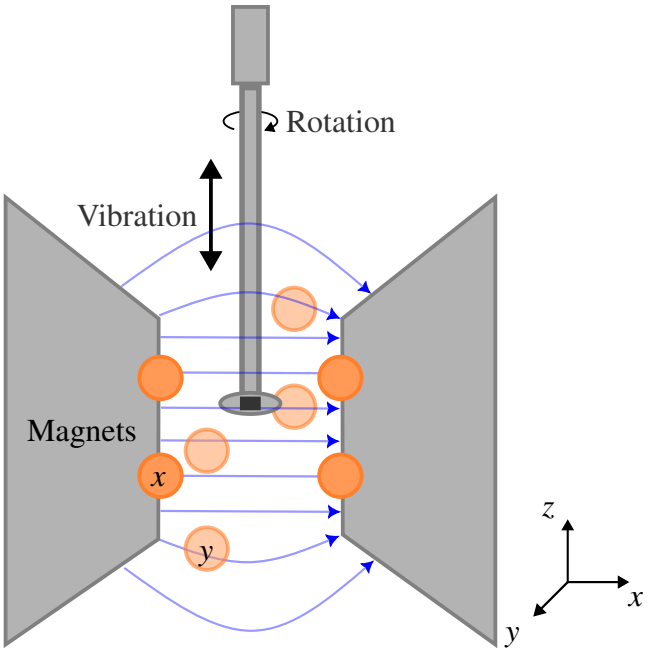

Figure 3.6: Schematic showing the basic setup of a VVSM. Within the homogeneous magnetic field (blue) of two electromagnets, the sample (black) is positioned. The sample holder is vibrating and can be rotated around the z-axis. In the x- and y-plane, four pickup coils each are sketched in orange. Adapted from [Fra21].

The saturation magnetization is determined only for the freestanding stripe geometries. With a light microscope, the width w of the stripes and the spacing d between the stripes has been determined. The resulting magnetic volume is given by

$$V = w \cdot l \cdot t_{\mathrm{F}} \frac{b}{w+d}, \tag{3.5}$$

where l is the length of the stripes and t_{F} the thickness of the FM material. The term $b/(w+d)$ represents the number stripes across the sample dimension b perpendicular to the stripes.

3.2.3 Kerr microscopy

In this work, Kerr microscopy is used to investigate the magnetization reversal processes in the geometries. This means, that the magentization reversal processes can be visualized by means of optical instruments. The underlying effect is the Kerr effect, which will be explained first.
Light can be described as an electromagnetic wave and characterized by its polarization. The direction of the electric field vector $\vec{E}$ is thereby the polarization direction. Linear polarized light, for instance, is characterized by the fact that $\vec{E}$ lays in a plane along its propagation, meaning its direction is constant. If the direction of $\vec{E}$ is rotating with a constant angular velocity, then it is called left or right circular polarized light, depending on the rotation's direction.
When linear polarized light is reflected from a magnetized material, two distinct effects are occurring. First, a rotation of the polarization of the reflected part, which is called Kerr effect.

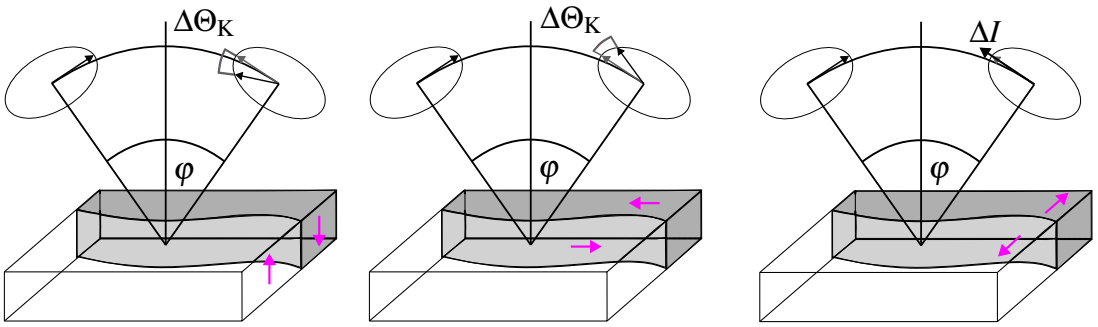

a) b) c)

Figure 3.7: Sketch of the three Kerr effects for p-polarized light. The black arrows indicate the incident and the outgoing light polarization. In gray the reference polarization is visualized. In the polar (a) and the longitudinal (b) configurations, a Kerr rotation $\Delta\Theta_K$ can be observed. In the transversal configuration (c), only a change in the intensity ΔI is detectable. The magnetization of the sample is indicted by the white and gray area and the corresponding direction given by the violet arrows. Adapted from [Fra21].

And second, a rotation of the polarization of the transmitted part, which is called Faraday effect. The change in the polarization can be understood by describing linear polarized light as a superposition of left and right circular polarized light. Depending on the magnetization, the two circular polarized light parts exhibit different absorption and reflection coefficients. Thereby, the ratio of the two left and right circular polarized components is changing, leading to a change of the polarization of the superposed linear light [Fra21]. Mathematically the effect results in a dependence of the dielectric displacement field $\vec{D}$ on the magnetization $\vec{m}$, which is in first order given by

$$\vec{D} = \varepsilon(\vec{E} + iQ_V\vec{m} \times \vec{E}), \tag{3.6}$$

with permittivity ε, Voigt Constant Q_V and electric field $\vec{E}$ [Fra21]. It can be seen, that the imaginary part of $\vec{D}$ depends linearly on the magnetization $\vec{m}$. This dependence of $\vec{D}$ on $\vec{m}$ results in a change of the polarization. Since the Kerr effect is used by the microscope and the Faraday effect is only parasitic effect here, only this effect will be explained in further detail. More general information can be found in [Fra21] and [Hub98]. The Kerr effect can be described by the Kerr rotation Θ_K and the Kerr ellipticity ξ_K resulting in the complex Kerr angle

$$\Theta_K^c = \Theta_K + i\xi_K. \tag{3.7}$$

For the Kerr effect, three basic effects can be separated by referencing the magnetization direction relative to the plane of incidence of the light (see Fig. 3.7). Furthermore, the polarization of the light can be in-plane (p-geometry) or out-of-plane (s-geometry) relative to the plane of incidence. Following Equ. 3.6 only perpendicular components of $\vec{m}$ and $\vec{E}$ lead to a rotation. If only parallel components are present, no effect can be observed. Therefore, the following effects can be observed [Fra21]: In the polar configuration, the magnetization points out-of-plane.

In both cases of the p- and s-geometry, the parallel component of the electric field leads to a Kerr rotation. The maximum effect can be observed by normal incidence of the light. The strength of the Kerr effect in the polar configuration is the highest of the three configuration [Fra21].
In the longitudinal configuration, the magnetization points parallel to the surface of the sample and in-plane to the plane of incidence. In the s-geometry again the parallel component of the electric field leads to a rotation of the polarization. In the s-geometry, the perpendicular component leads to a rotation instead. For the longitudinal Kerr effect, gracing incidence is preferred. The effect amplitude is about one order of magnitude weaker compared to the polar configuration [Fra21].
The last configuration is the transversal configuration. Here, the magnetization points parallel to the surface of the sample but out-of-plane to the plane of incidence. Only in the p-geometry, an effect is visible by a change in the intensity of the light instead of a rotation. For the transversal configuration, a normal incidence of the light leads to a maximum effect. Again, the effect amplitude is one order of magnitude weaker compared to the longitudinal configuration, meaning that the transversal Kerr effect is the weakest of the three [Fra21].
As already discussed, the dielectric displacement field $\vec{D}$ dependence linearly on the magnetization $\vec{m}$. An opposed magnetization leads to inverted rotation, by this, the relative strength and the direction of magnetization can be determined by a simple polarizer and analyzer setup [Fra21].
For the Kerr images a commercial wide-field Kerr microscope by Evico Magnetics is used. A camera is imaging a grayscale image of the sample. Besides the surface topology, each pixel is a representation of the surface magnetization. By changing an external field, for a hysteresis measurement for instance, the camera is capturing the change in the magnetization. An LED light source is used to irradiate the sample homogeneously with polarized light after applying the polarizer. The reflected beam is imaged after the analyzer through a 50x objective by a digital camera. The camera allows to laterally resolve the magnetization of the sample surface. Furthermore, the sample holder is surrounded by electromagnets, which can be used to apply an in-plane magnetic field. By varying the external field, a hysteresis loop can be measured and the magnetic reversal processes can be detected by the camera at the same time.

4 Modeling exchange bias

The following chapter aims to give an overview of possible ways to simulate the exchange bias (EB). First, a simple approach within the model of Stoner-Wohlfarth will be given. Extending on that, more advanced models capable of modeling more properties of real EB systems will be presented. Afterward, the model used in this work will be presented.

4.1 The model of Meiklejohn-Bean

In 1956 Meiklejohn and Bean observed the EB effect by hysteresis measurements of fine cobalt particles [Mei56]. They interpreted the shift of the hysteresis loop by an additional unidirectional anisotropy. This unidirectional anisotropy should result from the interaction between the ferromagnetic (FM) moments and the uncompensated antiferromagnetic (AFM) moments on the atomically smooth interface. For modeling the EB they further assumed that the FM is in a single domain state and rotating coherently. The AFM magnetization is assumed to be fixed and also in a single domain state [Rad08]. In Fig 4.1 the additional AFM magnetization $\vec{M}_{\mathrm{AFM}}$ has been added to the simple Stoner-Wohlfarth picture.

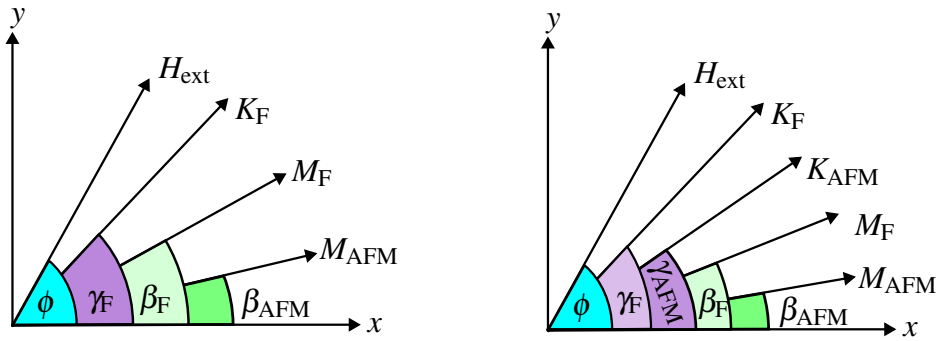

Figure 4.1: Extensions to the Stoner-Wohlfath model given in Chap. 2.7.1. a) The magnetization of the AFM M_{AFM} and its angle β_{AFM} is added in the Meiklejohn and Bean model. b) Extension of the realistic Meiklejohn and Bean model by the AFM anisotropy K_{AFM} and its angle γ_{AFM}.

Using the Heisenberg model for describing the interaction of the ferromagnetic spins $\vec{S}_{\mathrm{F,i}}$ and the antiferromagnetic spins $\vec{S}_{\mathrm{AFM,j}}$, coupled by an exchange interaction $J_{\mathrm{F/AFMi,j}}$, the interaction

is given by

$$\sum_{i,j} J_{F/AFMi,j} \vec{S}_{F,i} \cdot \vec{S}_{AFM,j} = \sum_{i,j} J_{F/AFMi,j} \left|\vec{S}_{F,i}\right| \left|\vec{S}_{AFM,j}\right| \cos(\beta_F - \beta_{AFM}) \tag{4.1}$$

Here it is assumed, that the FM and the AFM is always uniformly magnetized. The angles β_F and β_{AF} are defined in Fig. 4.1. Further assuming that the interaction is given by a single exchange coupling constant J_{EB} and an interface area A, the equation can be simplified to

$$\sum_{i,j} J_{F/AFMi,j} \left|\vec{S}_{F,i}\right| \left|\vec{S}_{AFM,j}\right| \cos(\beta_F - \beta_{AFM}) = J_{EB} A \cos(\beta_F - \beta_{AFM}) \tag{4.2}$$

giving the exchange energy for a given interface area. This additional energy contribution is then used in the Stoner-Wohlfarth model (see 2.7.1) resulting in

$$E(\beta_F)/A = \mu_0 H M_F^S t_F \cos(\beta_F - \phi) + K_F t_F^2 \sin(\beta_F - \gamma_F) - J_{EB} \cos(\beta_F - \beta_{AFM}). \tag{4.3}$$

Assuming for simplicity that the external field $\vec{H}$ is pointing along $\phi = 0$ and that the FM easy axis and AFM magnetization are pointing along $\phi = 0$, meaning $\gamma_F = M_{AFM} = \phi = 0$, then the equation is simplifying to Minimizing the energy density $E(\beta_F)/A$ for β_F, the strength of the EB field is given by [Rad08]

$$H_{EB} = -\frac{J_{EB}}{\mu_0 t_F M_F^S} \tag{4.4}$$

and the strength of the coercive field by

$$H_C = \frac{2K_F}{\mu_0 M_F^S}. \tag{4.5}$$

First of all, the results indicate that the hysteresis loop is shifted by H_{EB} as a result of the exchange interaction between the FM and the AFM. Furthermore, the dependence on the FM layer thickness is correctly captured. Nonetheless, the analytic result is orders of magnitude too high compared to experimental observations. The coercive field is also independent of the exchange interaction, which is not in accordance with the experimental observations of an increase in the coercive field [Rad08].

4.1.1 Realistic Meiklejohn and Bean model

A first extension to the simple Meiklejohn and Bean model is the realistic Meiklejohn and Bean model, by which the AFM magnetization can rotate as well. The rotation is given by an angle β_{AFM} of the AFM magnetization and an anisotropy K_{AFM} analogously to the FM layer. Equ. 4.3 is extended by a further energy contribution $K_{AFM} t_{AFM}^2 \sin(\beta_{AFM} - \gamma_{AFM})$, due to the angle

between the AFM magnetization and its anisotropy. All in all, the energy reads:

$$\begin{aligned} E(\beta_F)/A = {} & \mu_0 H M_F^S t_F \cos(\beta_F - \phi) \\ & + K_F t_F^2 \sin(\beta_F - \gamma_F) + K_{AFM} t_{AFM}^2 \sin(\beta_{AFM} - \gamma_{AFM}) \\ & - J_{EB} A \cos(\beta_F - \beta_{AFM}). \end{aligned} \tag{4.6}$$

The anisotropy K_{AFM} is of important role, since it has an influence on the EB strength H_{EB} and the coercive field H_C. In order to quantify different cases the R factor can be introduced by [Rad08]

$$R = \frac{K_{AFM} t_{AFM}}{J_{EB}}. \tag{4.7}$$

R describes the ratio between the anisotropy energy density of the AFM and the exchange coupling energy density. Depending on the value of R, the AFM magnetization rotates reversible, irreversible or isn't rotating at all. Further details can be found in [Rad08].

4.1.2 Further approaches

To account for the lower experimentally observed EB field, different models were introduced in the past, some of which will be introduced in the following. Néel [Kiw01] introduced a model where a partial domain wall can form in the AFM while remagnetization. The domain wall is thereby parallel to the interface and the AFM is still rigid, meaning that the AFM order is preserved. The creation of the partial domain wall costs energy that reduces the observed EB field. Noteworthy, his model predicts correctly a necessary minimum AFM thickness [Rad08].
A step further goes the model of Mauri [Mau87] by removing the assumption of the rigid AFM, allowing a formation of the partial domain wall even in the bulk of the AFM. The formation of the domain wall can be thought of as a spring. The energy of the domain wall is given by its angle α and an exchange stiffness of the AFM A_{AFM} following $-2\sqrt{A_{AFM} K_{AFM}}(1-\cos(\alpha))$. The formation of the domain wall is thereby reducing the total energy and also the observed EB strength. The model was further extended by Kim and Stamps [Kim00, Kim01b, Kim01a, Kim05].
The assumption of perfectly flat uncompensated interfaces is discarded by Malozemoff and his Random Field model [Mal87]. Those imperfections, e.g., layer roughness, lead to variations in the EB field and are modeled by a random field. As a result, the AFM breaks into domains with perpendicular domain walls. This model allows an understanding of the discrepancy between experimental results and models that assume a fully uncompensated AFM layer. Here, the AFM is compensated, but the imperfections create uncompensated spins at the interface, which lead to the EB shift. In [Rad08] the model has been compared to experimental results for a CoO/Co system. The results indicate a good agreement between experiment and theory.
Besides imperfections on the interface, the Domain State model by Usadel et al. [Rad08] assumes disorder even in the bulk by magnetic dilution. This magnetic dilution leads to magnetic

frustration and to domain formation in the AFM. Those domains have a small net magnetization because of statistical imbalances between two AFM sublattices. A strength of this model is the description of the EB effect in presence of nonmagnetic impurities in the AFM bulk and the dependence of the EB strength on temperature and AFM layer thickness [Rad08].
Another approach was done by Radu et al. [Rad08] in their Spin Glass model. Three assumptions are made in their model. First, there is a frustrated spin-glass-like interface between the FM and the AFM layer. Uncompensated frozen spins are responsible for the EB effect, and rotatable AFM spins with low anisotropy are responsible for an increase of the coercive fields. They further define a transition region from a purely FM layer to a purely AFM layer. In this transition region, the AFM anisotropy continuously increases towards the AFM layer. Spins close to the FM layer are therefore rotatable, and spins close to the AFM layer are frozen. Radu et al. were able to reproduce the azimuthal dependence of H_{EB} and H_{C} on the external field, the dependence of H_{EB} on the AFM layer thickness, and training effects [Rad08].

4.2 Polycrystalline models

The previously discussed models do not take into account the polycrystalline nature of the sputtered layers. The first approach to polycrystalline structures was done by Fulcomer and Charap [Ful72]. They described the AFM layer as consisting of small particles that only interact with the FM layer. The interaction takes place by uncompensated spins that are exchange coupled to the FM layer. Since the grains possess different sizes and shapes, they also assumed a distribution of anisotropies and coupling strengths. Further, they introduced a thermal stability for each particle depending on their properties, the external field frequency, and the temperature. Depending on the repose of the grains by magnetization reversal of the FM layer, three types of grains are defined. Particles that instantly follow the FM layer, because their coupling is much stronger than the anisotropy for every given temperature. Particles with a larger anisotropy to coupling strength ratio are superparamagnetic and follow the FM layer within the measurement time. With even higher anisotropies particles become blocked, meaning that they keep their orientation even in opposite saturation of the FM layer all over the measurement time. By this blocking, the particles contribute to the EB shift, while the superparamagnetic and unblocked particles contribute to an increase of the coercive field. Since the boundaries of the grain types also depend on the temperature, the model is able to capture a range of effects connected to measurement temperatures, like the decrease in the EB shift for increasing temperature or the peak of H_{C} at the blocking temperature. Many other models are based on the general idea of Fulcomer and Charap [OG10].
The idea of different grain type has been extended by Soeya et al. [Soe96] to four distinct types of grains. This separation is based on the idea that AFM grains possess two orientations for which the energy is minimized [Ehr05, Ehr06]. Both minimums, a local (antiparallel to the

field) and a global one (parallel to the field), are separated by an energy barrier given by

$$\Delta E = E_1 - E_2 \left(1 - \frac{E_2}{4E_1}\right), \tag{4.8}$$

with $E_1 = K_{\mathrm{AFM}} V_{\mathrm{grain}}$ and $E_2 = J_{\mathrm{EB}} A_{\mathrm{grain}}$. Both given by the grain volume V_{grain} and interface area A_{grain}. Due to thermal fluctuations, grains can relax from the local to the global one or vice versa into the local one with relaxation time τ. The grain types are now defined by their relaxation time compared to the experiment time. Type I grains possess a small energy barrier resulting in a random occupation of the minimums, independent of the external field. These grains are called superparamagnetic. Type II grains can relax into the global minimum within the measurement time. In a hysteresis measurement, those grains follow the FM layer and therefore contribute to the increased coercive field. Type III grains do not relax into the minimum, because the energy barrier is too high. But type III grains can be aligned at high temperatures, e.g., in the field cooling (FC) process. Type III grains, therefore, contribute to the EB shift. Type IV grains do not relax into the global minimum even in the FC process and are therefore randomly oriented and do not contribute to the macroscopic EB effect [Mer20].
On the basis of the above given separation, a time-depended Stoner-Wohlfarth approach was introduced by Müglich et al. in [Mü16] and recently improved by Merkel et al. in [Mer20].

4.3 Polycrystalline model of Harres

The basis for the micromagnetic simulations is the model of Harres et al. [Har12]. Here, a polycrystalline AFM layer with a granular interface is assumed. Each grain possess a small net magnetization due to uncompensated spins and is exchanged coupled to the FM layer. The AFM grains are characterized by their behavior when the FM layer is changing its magnetization. Grains can either be stable, meaning that they keep their orientation, or unstable, e.g., following the FM layer by remagnetization. By this classification, an understanding of the EB shift and increase of the coercive field H_{C} compared to unbiased systems is possible.
The energy contribution of each grain is given by

$$K_{\mathrm{AFM,i}} v_{\mathrm{i}} \sin(\beta_{\mathrm{AFM,i}} - \gamma_{\mathrm{AFM,i}}) - J_{\mathrm{EB,i}} a_{\mathrm{i}} \cos(\beta_{\mathrm{F}} - \beta_{\mathrm{AFM,i}}), \tag{4.9}$$

where i stands for the i^{th} grain possessing its own anisotropy $K_{\mathrm{AFM,i}}$, orientation $\beta_{\mathrm{AFM,i}}$, volume v_{i}, interface area a_{i} and exchange coupling constant $J_{\mathrm{EB,i}}$. Following the Stoner-Wohlfrath model all energy contributions need be summed up. In summary the energy reads

$$\begin{aligned} E(\beta_{\mathrm{F}}) = {} & \mu_0 H M_{\mathrm{F}}^S V \cos(\beta_{\mathrm{F}} - \phi) + K_{\mathrm{F}} V \sin(\beta_{\mathrm{F}} - \gamma_{\mathrm{F}}) \\ & + \sum_{\mathrm{i}} K_{\mathrm{AFM,i}} v_{\mathrm{i}} \sin(\beta_{\mathrm{AFM,i}} - \gamma_{\mathrm{AFM,i}}) - J_{\mathrm{EB,i}} a_{\mathrm{i}} \cos(\beta_{\mathrm{F}} - \beta_{\mathrm{AFM,i}}) \end{aligned} \tag{4.10}$$

with total volume V of the FM layer. The first line is the energy given by the Zeeman energy and the anisotropy energy for the FM layer, and the second line sums up all energy contributions of the grains. A possible Zeeman energy of the AFM grains is thereby neglected. Again, in general, four types of grains can be separated:

- Superparamagnetic grains with no stable magnetization.
- Grains that have a stable magnetization but rotate directly the FM layer, called rotatable or unstable grains.
- Grains that are fixed in direction by the FC direction, called pinned or stable grains.
- Grains that are fixed but independently of the FC direction.

The superparameganetic and unset grains are neglected in their model by assuming that they average out over the sample volume. Following that assumption, only two types of grains are considered. The stable grains are pointing in the EB direction and contribute therefore to the EB shift. The unstable grains follow the FM layer and contribute to the increase of H_C. Simulation results indicate that the EB field is increasing with an increasing number of set grains, while the coercive field is decreasing. With this model, Harres et al. were also able to reproduce the experimental results of a sputtered Co/IrMn system and training effects could be captured. As a last important remark, it is worth noticing that a grain is not classified set or rotatable just by their anisotropy, rather than by the ratio between anisotropy and exchange coupling strength. Large grains with high anisotropy can also be rotatable if the coupling to the FM is strong enough.

4.4 Micromagnetic model of De Clercq

All the discussed models so far are based on the ideas of Stoner and Wohlfarth. The remagnetization takes place only by coherent rotation. Furthermore, the effects occurring due to stray fields are neglected since only full film systems are simulated. To simulate the nucleation processes, micromagnetic simulation can be used. The concrete basis for the used model here is the model of De Clercq [Cle17] for uncompensated interfaces.
The simulation tool used is Mumax3 [Van14], which is a micromagnetic simulation program, that is using the finite difference method to solve the Landau-Lifschitz-Gilbert (LLG) equation with appropriate discretization. In the context of micromagnetic simulations, layers are meant to be layer of the discretized volume rather than layers in the multi-layer thin film system. Here, only the FM and FM/AFM interface is simulated, neglecting all other layers of the system. Further information regarding Mumax3 and GPU optimization can be found in [Van14, Lel18].
The idea of De Clercq is to simulate the AFM interface as a pseudo-AFM layer, by using a FM layer for the uncompensated spins and neglecting the bulk of the AFM. The layer is

given effective parameters, e.g., realistic anisotropy, as it would be an AFM. For simplicity, the pseudo-AFM layer is simply called AFM layer, even though it actually is a FM layer. The layer is then exchanged coupled to the lowest FM layer. To gain realistic exchange coupling energies a scaling factor can be set between the AFM and the lowest FM layer. Energies in Mumax3 generally depend on the cell volume, rather than on the interface area. Therefore, the interface exchange energy needs to be converted into a volume energy by the scaling factor.
The exchange energy density between two neighboring cells with magnetization $\vec{m}_1$ and $\vec{m}_2$ and saturation magnetizations M_1 and M_2 is given by

$$\varepsilon = -\frac{1}{2} M_1 \vec{m}_1 \cdot \vec{B}_{\text{exch},1}. \tag{4.11}$$

The exchange field $B_{\text{exch},1}$ is given by

$$\vec{B}_{\text{exch},1} = 2S\alpha \left(\frac{\vec{m}_1 - \vec{m}_2}{\Delta^2} \right) \text{ with } \alpha = \frac{2}{\frac{M_1}{A_1} + \frac{M_2}{A_2}}. \tag{4.12}$$

Thereby, is Δ the distance between the cells and A_1 and A_2 the exchange stiffness. Further is S the scaling factor mentioned above. Which is given by

$$S = \frac{J_{\text{I}} C_{\text{z}}}{\alpha (M_1 + M_2)}, \tag{4.13}$$

with C_{z}, the height of the cell. In the case of FM/AFM interfaces are $M_1 = M^S_{\text{FM}}$, $M_2 = M^S_{\text{AFM}}$, $A_1 = A_{\text{FM}}$ and $A_2 = A_{\text{AFM}}$ the saturation magnetization and exchange stiffness of the FM and AFM layers.
In order to get the correct interface energy density J_{I}, the exchange stiffness at the interface $A_{\text{I}} = J_{\text{I}} C_{\text{z}}/2$ needs to be symmetrical for the FM and AFM cells. This is realized by setting $M^S_{\text{AFM}} = M^S_{\text{FM}}$. This first seems unrealistic, but since the magneto static energy is neglected in AFM cells, the assumption has no further influence on the simulation results. Furthermore, the effective field is only changing its absolute value and not its direction. This leads to a scaling in time, but since only static energy minimization is performed, the same energy minimum will be found.
The AFM layer is split into grains via Voronoi Tessellation [Lel18]. Each grain receives randomly a region number within a defined interval. In total 256 regions can be defined. A region is then further characterized by a set of material parameters. By this, different material parameters can be given to grains, making them rotatable or fixed like in the model of Harres et al.. In other words, a region is a representation of a certain volume in the simulation with defined properties.

In [Cle16] and [Cle17] the model has been used to simulate training effects in Co/CoO systems. The system was discretized in $2,5\,\text{nm}$ x $2,5\,\text{nm}$ x $3\,\text{nm}$ cells with a total simulation size

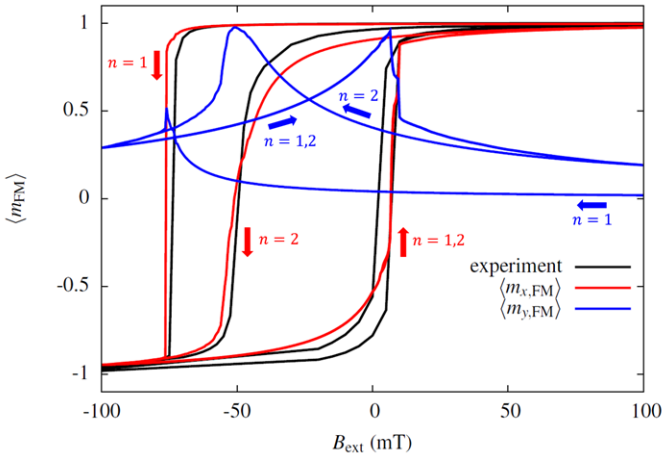

Figure 4.2: Simulated hysteresis loop for a FM Co layer. Shown are the average magnetizations in the x (red) and the y (blue) directions in the dependence on the external field B_{ext} in the x-direction for the first and second hysteresis cycles. Taken from [Cle17].

of 512 x 512 x 11 cells, where the lowest layer is used for the AFM layer. To simulate a full film system, periodic boundary conditions (x = 10, y = 10, z = 0) were used. The volume was further split into grains of 12 nm size with Voronoi Tessellation. For the FM layer a saturation magnetization of $M_{FM}^{S} = 1400\,\text{kA/m}$, an exchange stiffness of $A_{FM} = 30\,\text{pJ/m}$, and an anisotropy of $K_{FM} = 2.0 \cdot 10^4\,\text{J/m}^3$ with an angular distribution of 10° around the easy axis were set. For the AFM layer, the grains were split into two categories. 30% of the grains are fixed and 70% are rotatable. The ratio is rather arbitrary since, as they argued, experiments show that pinned grain densities can range from a few percent [Ohl03] to 80% [Wu10]. The pinned grains possess a high anisotropy of $K_{AFM,pin} = 2.7 \cdot 10^7\,\text{J/m}^3$ and the rotatable grains possess an anisotropy of $K_{AFM,pin} = 2.0 \cdot 10^6\,\text{J/m}^3$. The smaller anisotropy allows those grains to follow the FM magnetization. The exchange stiffness for the AFM grains was set to $A_{AFM} = 4.0\,\text{pJ/m}$. Last, the exchange coupling constants for the interfaces were set to $A_{I,pin} = 6.9 \cdot 10^{-12}\,\text{J/m}$ and $A_{I,rot} = 1.1 \cdot 10^{-11}\,\text{J/m}$ for the pinned and rotatable grains. A simulated hysteresis loop can be seen in Fig. 4.2 for two consecutive hysteresis cycles. The first hysteresis loop possess an EB field of $B_{EB} = 35\,\text{mT}$ and a coercive field of $B_C = 42\,\text{mT}$. The second loop possess a reduced EB field of $B_{EB} = 22\,\text{mT}$ and a reduced coercive field of $B_C = 29\,\text{mT}$. By this, it can be seen that the athermal training effect could be reproduced. The thermal training effect could not be reproduced, since the simulations were performed at 0 K [Cle16, Cle17]. The results of their model are a reference for the simulations presented in the next chapter.

5 Results

In the last chapter, an overview of different models was given. Especially the model of De Clareq will be the basis for most of the simulations here. Using their results as a fundament, further full film simulations will be presented. Besides the pinning ratio, the ferromagnetic (FM) and antiferromagnetic (AFM) layer thicknesses, the angular distribution of anisotropies will be revisited. Afterward, simulations for the different geometries will be presented. The simulations will be compared to experimental results provided by Sapida Akhundzada in the scope of a PhD thesis. The experimental observations delivered suggestions for development and modification steps of the model. In agreement with the experimental results, the theoretical model will deliver information about the physical background and origins of the observed phenomena. The validated theoretical model will further be used to simulate magnetic sample geometries and predict their magnetic behaviour well in advance of the experimental realization. Thereby, an edge region will be defined, allowing to incorporate edge effects, e.g. effects of the lithographical process or the ion bombardment (IB) in the case of the embedded geometries. Why this was necessary will also be explained by unfolding the steps taken to build the model. Besides that, simulations of embedded squares and discs will be presented, which have not been investigated experimentally so far.

The presented simulations, aim to reproduce a $Ni_{81}Fe_{19}$(FM)/$Ir_{17}Mn_{83}$(AFM) exchange bias (EB) system. The NiFe layer has a thickness of 10 nm in the experiment. In the simulations, the FM layer is 9 nm thick, due to the fixed cell size of 3 nm. Typical parameters for a $Ni_{80}Fe_{20}$(FM) layer are an exchange stiffness of $A_{\mathrm{FM}} = 13 \cdot 10^{-12}$ J/m and a saturation magnetization of $M_{\mathrm{FM}}^{S} = 796$ kA/m [Hei08]. Even though this is a slightly different composition, it will be used as a reference. Using both parameters, an exchange length [Abo13] of $l_{\mathrm{ex}} = \sqrt{2A_{\mathrm{FM}}/\mu_0 M_{\mathrm{FM}}^{S}} \approx 5,7$ nm can be calculated. This justifies a cell size of 5 nm x 5 nm x 3 nm, as it is used in all simulations presented here. As mentioned in Chap. 3.1.1, after sputtering a polycrystalline structure is obtained, leading to a vanishing crystalline anisotropy. Nonetheless, a small uniaxial anisotropy can be present due to the applied magnetic field in the sputtering process. This is taken into account with a small anisotropy of $K_1 = 1000\,\mathrm{J/m^2}$.

For the AFM an exchange coupling of $A_{\mathrm{AFM}} = 1.1 \cdot 10^{-11}$ J/m has been chosen for both the pinned and rotatable grains. To pin the set grains, an anisotropy of $K_{\mathrm{AFM,pin}} = 2.7 \cdot 10^{8}\,\mathrm{J/m^2}$ was used. This value has been taken from [Cle17] and could have been chosen way smaller, but as long as the grains are pinned, the value is rather arbitrary. The interface exchange coupling constant was set to $J_{\mathrm{I,pin}} = 1.8 \cdot 10^{-4}$ J/m. In Mumax3 the exchange energy is a volume energy.

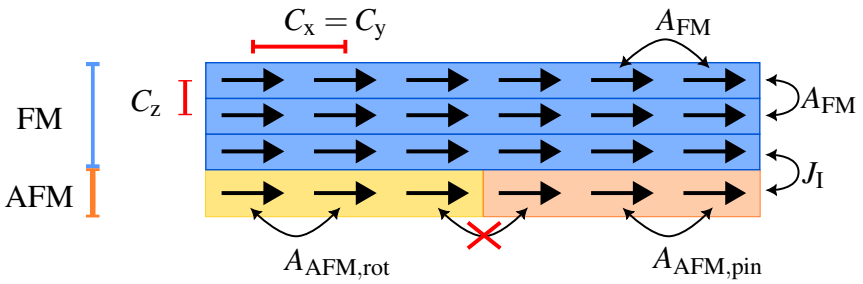

Figure 5.1: Visualization of the basic model used here. The FM layer (blue) consists of three layers. The AFM layer is split into rotatable (yellow) or pinned (orange) grains. Further the exchange stiffnesses A_i, the interface coupling constant J_I and the cell dimensions C are indicated. The exchange coupling between the grains is deactivated.

To get the correct interface energy, it needs to be mapped from a 2D surface to a 3D volume. This is achieved by setting a scaling factor S, as explained in Chap. 4.4.

Given a cell height of $C_z = 3\,\text{nm}$, the grains stay pinned since $K_{AFM,pin} C_z \gg J_{I,pin}$. For the rotatable grains, a value of $K_{AFM,rot} = 4000\,\text{J/m}^2$ has been set. Further, the interface exchange coupling constant for the rotatable grains was set to $J_{I,rot} = 0.4 \cdot 10^{-4}\,\text{J/m}$. This results in a rotatability of the grains, since $K_{AFM,rot} C_z < J_{I,rot}$. The described system with the introduced parameters is visualized in Fig. 5.1. The exact ratio between pinned and rotatable grains depends on the respective simulation and will be mentioned each time. The AFM was split into grains by Voronoi-Tesselation [Cle17] represented by the regions 0 - 199 in MuMax3. To realize a pinning ratio of x percent, simply the first $2x$ region received the parameters for pinned grains, while the rest were set to the rotatable grains. All AFM grains possess no demagnetization field and do not interact with each other. Further, no interaction with the external field is assumed. For receiving a hysteresis curve, a 'for loop' was defined starting at a field strength of $B_{max} = 50\,\text{mT}$ and stepping in $\Delta B = 0.5\,\text{mT}$ field steps down to $B_{min} = -50\,\text{mT}$ and up again.

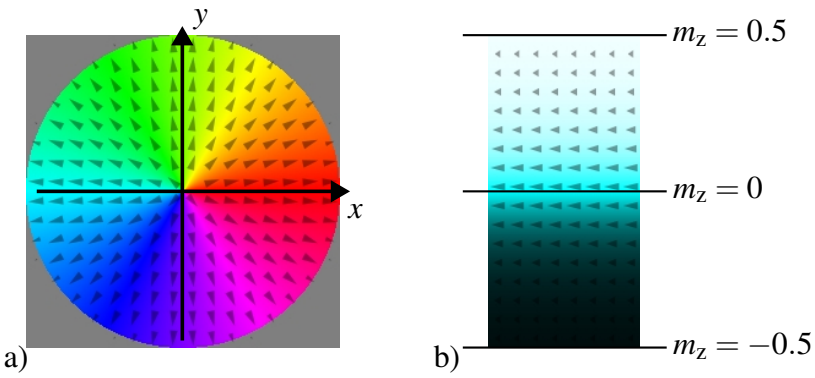

Figure 5.2: a) Representation of the in-plane field direction and the corresponding color is given. A magnetic field pointing in positive x-direction is given by a red color for instance. b) The effect of a out-of-plane component for the color brightness is shown. A positive out-of-plane component leads to lighter colors, while a negative component leads to darker colors.

Each step, the system was relaxed by the 'Relax()' function. To avoid artifacts, the field and the easy axis are slightly canted by an angle of 3° to each other, as it is also done in other micromagnetic simulations [PZL20]. At each field step, the magnetization of the AFM and FM top layer was saved as an image and a 3D matrix. In the images, the magnetization direction is indicated by a color. In Fig. 5.2 a circle is given, showing which color represents which magnetization direction. Besides that, the brightness represents the out-of-plane component. A positive z-component leads to a lighter color and a darker color indicates a negative z-component.

5.1 Full film simulations

Full film simulations were performed to investigate the basic capabilities of the model described above. As already said, the model is based on the model used in [Cle16] and [Cle17], but the material parameters have been changed as described above. Periodic boundary conditions (PBC) have been set to $x = 10$, $y = 10$, and $z = 0$ to avoid edge effects. At the same time, the cell size was set to 5 nm x 5 nm x 3 nm, still matching the required size below the exchange length $l_{ex} \approx 5.7$ nm. The simulation volume is given by the cell size multiplied by the discretization of 512 x 512 x 4 cells. The bottom layer is the AFM layer, modeled as described in Chap. 4.4 and representing the interface moments. All anisotropies are aligned parallel to the field axis. In Fig. 5.3 a simulated hysteresis is shown. In this simulation the pinning ratio was at 30%,

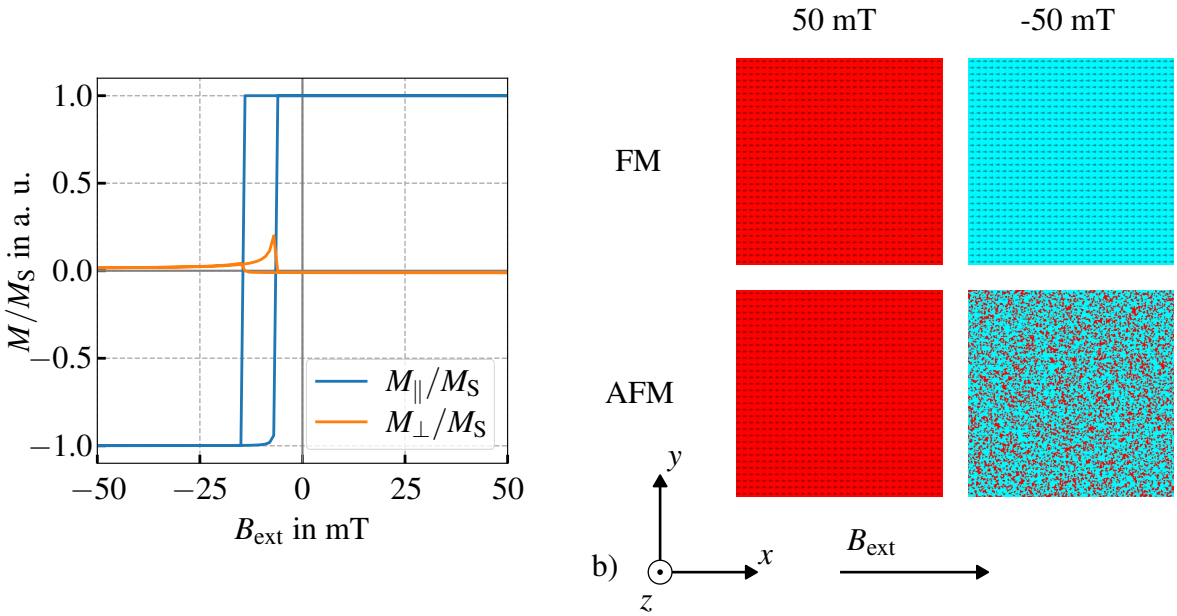

Figure 5.3: a) Hysteresis loops gained by a full film simulation for a pinning ratio of 30%. Shown are the parallel and perpendicular magnetization M in dependence on the external field B_{ext} b) The corresponding magnetization of the FM and AFM layer is given in positive and negative saturation. In negative saturation the pinning of the pinned grains is clearly visible in the AFM layer.

meaning that 30% of the grains were pinned and the remaining 70% were rotatable grains. In Appendix 7.2 an example code for the full film simulations is given. The resulting hysteresis shows an EB field of $\mu_0 H_{\mathrm{EB}} = 8.0\,\mathrm{mT}$ and a coercive field of $\mu_0 H_{\mathrm{C}} = 4.5\,\mathrm{mT}$. Both values are close to experimentally observed values of 6 mT and 2 mT (see. Fig. 5.10), indicating that the chosen parameters are acceptable. Nonetheless, the coercive field is overestimated by a factor of 2. Besides that, the AFM layer at different field strength can be seen in Fig. 5.3. In positive saturation of the FM layer, the rotatable and pinned AFM grains point into the same direction. In negative saturation, the rotated AFM grains are clearly visible, since they are magnetized in the negative direction, while the pinned AFM grains keep their initial orientation. All in all, the model replicates a realistic hysteresis loop. The steep hysteresis branches indicate, that the remagnetization takes place by spin-flip. This can also be seen in the images of the magnetization. The rotatable and pinned grains behave as expected, meaning that they follow the FM layer or stay pinned respectively. In the following, parameter variations are done and investigated in detail to gain more insights of the EB system's behavior.

5.1.1 Number of pinned grains

In [Har12], the ratio between pinned and rotatable grains was varied in their extended Stoner-Wohlfarth model. With an increasing number of pinned grains the EB field was increasing, while the coercive field was decreasing. Similar simulations have been performed with micromagnetic simulations and the introduced MuMax3 model. The ratio between pinned and rotatable grains was varied between 0% and 100% in 10% steps. The resulting values for $\mu_0 H_{\mathrm{EB}}$ and $\mu_0 H_{\mathrm{C}}$ are plotted in Fig. 5.4. The linear trend is clearly visible. The EB field linearly depends on the amount of pinned grains. In case of no pinned grains, the EB field is vanishing, as expected. The maximum field of $\mu_0 H_{\mathrm{EB}} = 25.5\,\mathrm{mT}$ is realized when all grains are pinned. It can be concluded that the pinned grains are responsible for the EB effect. With the model of Meiklejohn and Bean, one would expect an EB field of $\mu_0 H_{\mathrm{EB,MB}} = -pJ_{\mathrm{I,pin}}/(M^S_{\mathrm{FM}} t_{\mathrm{F}})$, with a pinning ratio p. For $p = 1$ and the simulation parameters ($J_{\mathrm{I,pin}} = 1.4 \cdot 10^{-4}\,\mathrm{J/m}$, $M^S_{\mathrm{FM}} = 796\,\mathrm{kA/m}$, and $t_{\mathrm{F}} = 9\,\mathrm{nm}$), the theoretical result reads $\mu_0 H_{\mathrm{EB,MB}} = 25,06\,\mathrm{mT}$, and is therefore perfectly matched. Keeping in mind that the experimental results were closely matched, the used interface coupling constant and the chosen pinning ratio of 30% seem acceptable. Opposed to that, the coercive field is decreasing with increasing number of pinned grains. Starting at 5.6 mT the field is decreasing to 2.0 mT when all grains are pinned. Here, it can be noticed that the often observed increase in the coercive field in EB systems is connected to the rotatable grains. Using again the model of Meiklejohn and Bean, a coercive field of $\mu_0 H_{\mathrm{C,MB}} = 2K_{\mathrm{F}}/M^S_{\mathrm{FM}} = 2.5\,\mathrm{mT}$ for full pinning would be expected and is nearly matched by the simulations. Here it was assumed, that the applied magnetic field in the sputtering process, leads to a small anisotropy of $K_{\mathrm{F}} = 1000\,\mathrm{J/m^3}$. Summarizing the results, it can be concluded, that the influence of the pinned and rotatable grains is correctly modeled. The observed influence of the pinned and

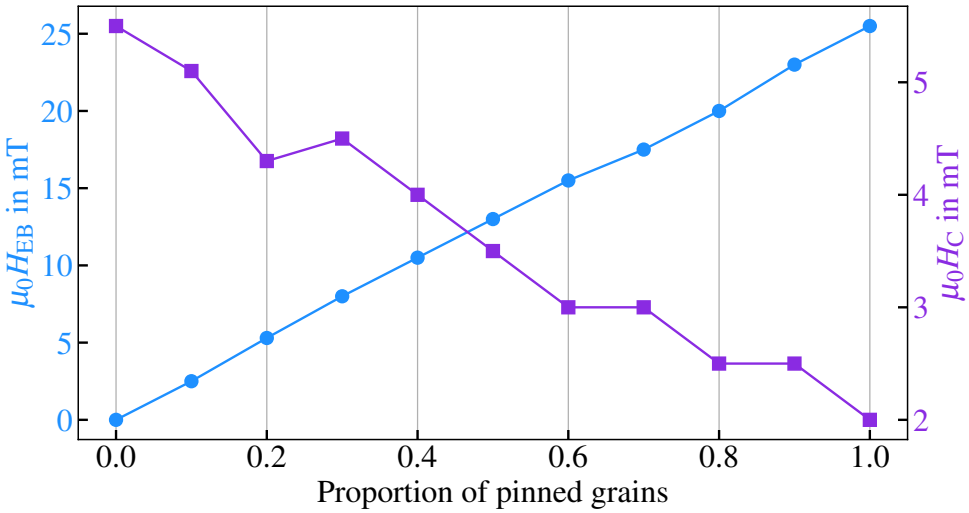

Figure 5.4: In blue the EB field and in violet the coercive field for simulated pinning ratios from 0% to 100% are plotted. The EB is linearly increasing, while the coercive field is decreasing with increasing pinning ratio.

rotatable grains by Harres et al. [Har12] could be reproduced. When taking a look at the perpendicular magnetization an asymmetry can be observed (see Fig. 5.3). This asymmetry can be characterized by $\xi = m_{\text{perp},1} - m_{\text{perp},2}$, with peaks of the perpendicular magnetization $m_{\text{perp},1}$ and $m_{\text{perp},2}$ [Cam05] and is also depending on the pinning ratio (Fig. 5.5). With an increasing number of pinned grains, the asymmetry is first increasing and then decreasing again. This observation strengthens the fact that the asymmetry cannot be observed in non-EB systems and

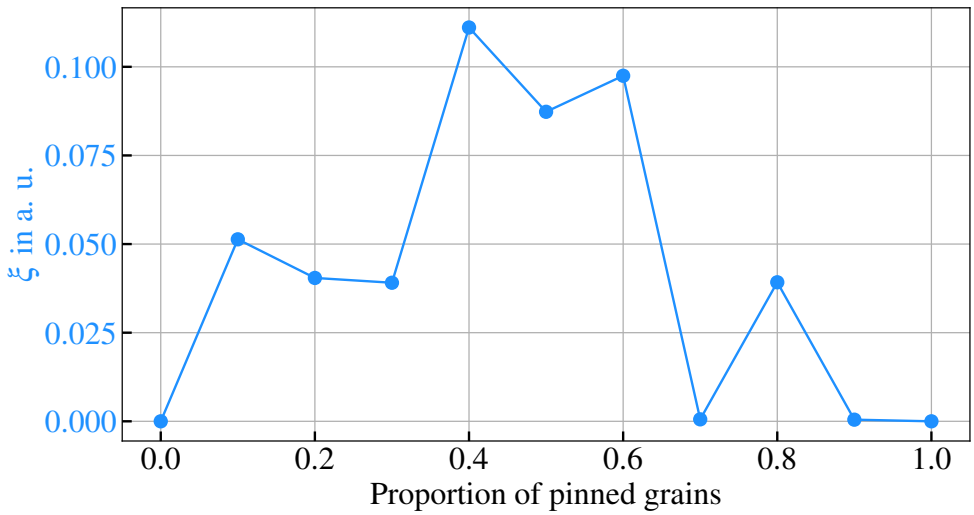

Figure 5.5: Plot of the asymmetry $\xi = m_{\text{perp},1} - m_{\text{perp},2}$ given by the peaks in the perpendicular magnetization $m_{\text{perp,i}}$, simulated with an angle of 7° between EB field and external field. With increasing number of pinned grains, the asymmetry is increasing until it reaches a maximum and decreases afterwards.

therefore is connected to the EB effect. To be more precise, for no pinned grains, the asymmetry is vanishing. A maximum can be observed at 40% of $\xi = 0.12$. Afterwards the asymmetry is decreasing to $\xi = 0$ again.
As it has been described in Sec. 2.6.1, the asymmetry is only present if there is a angle between EB direction and the direction of the external field. Interestingly the position of the maximum of ξ depends on this angle. Simulations at different angles between the EB field and the external field have been performed showing that the maximum shifts towards lower pinning ratios with increasing angles. For a small angle of 3°, the maximum is reached at a pinning ratio of 70%, for 5° at 60%, for 7° at 40% and for a angle of 10° already at 30%. In [Cam05] simulations based on the Stoner-Wohlfarth model showed, that there is a critical angle α_C under which a asymmetry is observable. An increasing EB strength leads to a decreasing critical angle. This explains why the peak is moving towards smaller pinning ratios with increasing angle.

5.1.2 Ferro- and antiferromagnetic layer thickness

Interesting properties are the influence of the FM and AFM layer thicknesses. For investigating the influence of the FM layer thickness, the model has been slightly changed. Simple changing the cell size is not sufficient, since the AFM layer thickness would be changed. Therefore, the cell height was set to 1 nm and the FM thickness was changed by changing the number of layers. To keep the parameters for the AFM untouched, the interface was simulated by three AFM layers, resulting again in a total height of 3 nm for the interface. The FM thickness was varied between 3 nm and 9 nm or three to nine layers. All other parameters were kept unchanged. In Fig. 5.6 the resulting EB and coercive fields are plotted. The EB field clearly shows the expected $1/t_F$ dependence, while the coercive field is also slightly decreasing. The reason for the decrease is unclear. Taking a look at the magnetization of the FM, it can be seen that the FM layer is more rigid, meaning the spins stay more aligned with each other. The effect is only weakly present but could be a possible reason. In [Mer22b] experiments for different FM layer thicknesses showed, that the coercive field is increasing like the exchange field with decreasing FM layer thicknesses. This behavior could not be reproduced in the simulations.
For the AFM layer, the approach is different. Since only the interface is simulated, the thickness cannot be simple reduced or increased. Theoretically one would expect a steep decrease of the EB field below a critical thickness. Following [Mer22a] and [Mer22b], this is connected to a change in the pinning ratio. Below the critical thickness, grains do not possess enough volume to be pinned and therefore the pinning ratio is decreasing in favor of increasing the number of rotatable grains. To simulate this behavior, the anisotropy of the pinned grains is multiplied by the thickness. Resulting in an effective anisotropy

$$K_{\text{eff}} = K_{\text{AFM,pin}} \cdot t_{\text{AFM}}/t_{\text{AFM,ref}}, \tag{5.1}$$

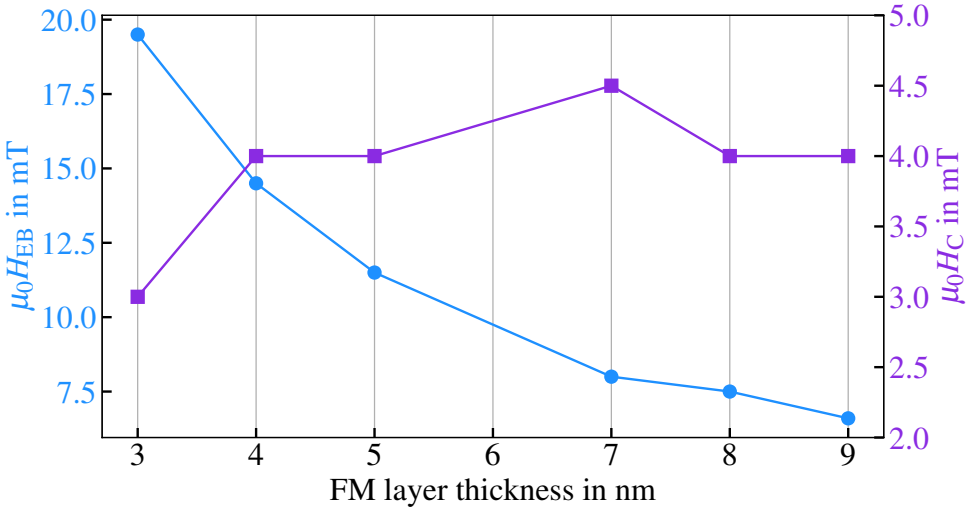

Figure 5.6: Plot of the simulated EB (blue) and coercive (violet) fields against the FM layer thickness at three AFM layers of 1 nm each. The EB field shows the expected $1/t_{FM}$ thickness dependence.

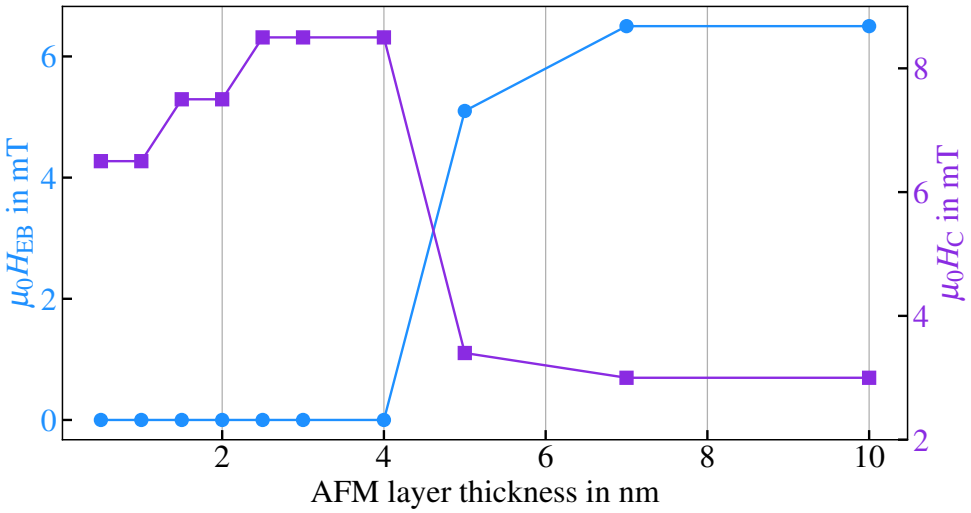

Figure 5.7: Plot of the simulated EB (blue) and coercive (violet) fields against the AFM layer thickness at a FM thickness of 9 nm. Below a critical thickness the EB field is vanishing. At the same time the coercive field is increasing. Above the critical thickness the coercive field is decreasing and the EB effect is occurring.

with reference thickness $t_{AFM,ref}$. By choosing $K_{AFM,pin} = 100000\,J/m^2$ and $t_{AFM,ref} = 10\,nm$, the steep decrease could be simulated, as can be seen in Fig. 5.7. Besides that, also the peak in the coercive field could be observed. The determined critical thickness is $t_{AFM,crit} = 4\,nm$. At $t_{AFM,crit}$, $K_{eff} \cdot t_{AFM,crit}$ is $1.5 \cdot 10^{-4}\,J/m$. At the same time, the coupling is $J_{I,pin} = 1.8 \cdot 10^{-4}\,J/m$. For lower thicknesses, the grains are rotatable, while for larger thicknesses the grains are pinned.

5.1.3 Angular distribution of anisotropies

So far, all anisotropies were perfectly aligned with the easy axis. A further question is the influence of the angular distribution of the grain's anisotropies. In the following simulations, two angles for the pinned grains α_{pin} and the rotatable grains α_{rot} have been defined. Within the limits of these angles, the anisotropy axes of the grains are randomly distributed. To be more precise, when initializing the grains, the anisotropy axis is defined. The angle between this axis and the x-axis is smaller than α_{rot} or α_{pin} but randomly chosen. The pinning ratio was 30%.
Foremost, α_{rot} was varied from 0° to 180° in 10° steps, while keeping α_{pin} constant at $0°, 10°$ and 20°. The results for $\mu_0 H_{\text{EB}}$ and $\mu_0 H_{\text{C}}$ can be seen in Fig 5.8. The EB field stays constant for all α_{rot} at about 6 mT. The coercive field is decreasing with increasing angular distribution until reaching a plateau at about 3 mT. The decrease is about the same for all distributions.

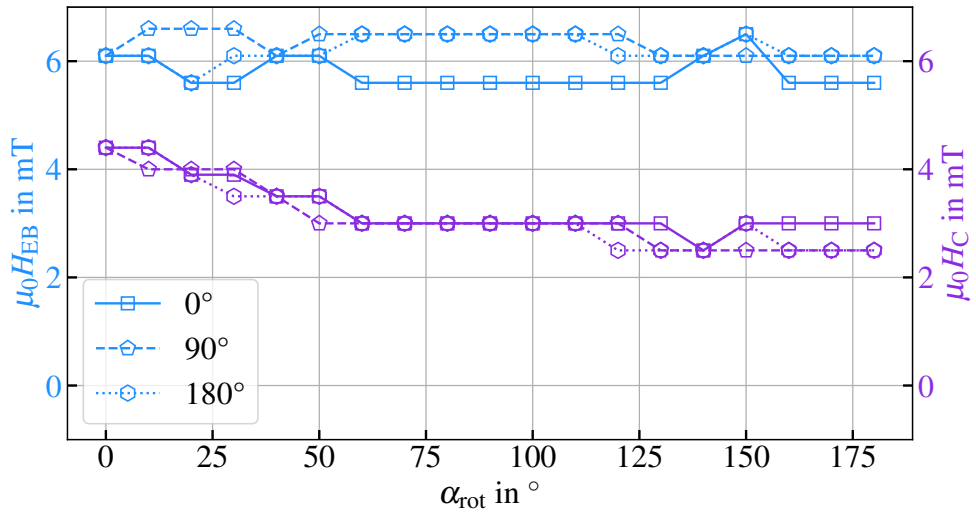

Figure 5.8: Shown is the simulated EB field (blue) and coercive field (violet) in dependence of α_{rot} for $\alpha_{\text{pin}} = 0°$ (solid line, square), 10° (dashed line, pentagon) and 20° (dotted line, hexagon).

Second, α_{pin} was varied from 0° to 180° in 10° steps, while keeping α_{rot} constant at $0°, 90°$ and 180°. The results for $\mu_0 H_{\text{EB}}$ and $\mu_0 H_{\text{C}}$ can be seen in Fig. 5.9. This time, a strong dependence of the EB field can be seen. The wider the anisotropies are distributed, the weaker the EB effect. This corresponds to the importance of the field cooling (FC) process. After sputtering without applied field no EB effect can be observed. This is represented by a wide distribution of the grain's orientations. The FC process aligns the grains along the field axis reducing the angular distribution and thereby creating the EB effect.
Opposed that, no dependence of the coercive field on α_{pin} can be observed, even though a small peak around 80° can be seen. Nonetheless, the coercive field is larger for $\alpha_{\text{rot}} = 0°$ compared to $\alpha_{\text{rot}} = 90°$ and $\alpha_{\text{rot}} = 180°$.
It can summarized, that the angular distribution of the rotatable grains does not influence the

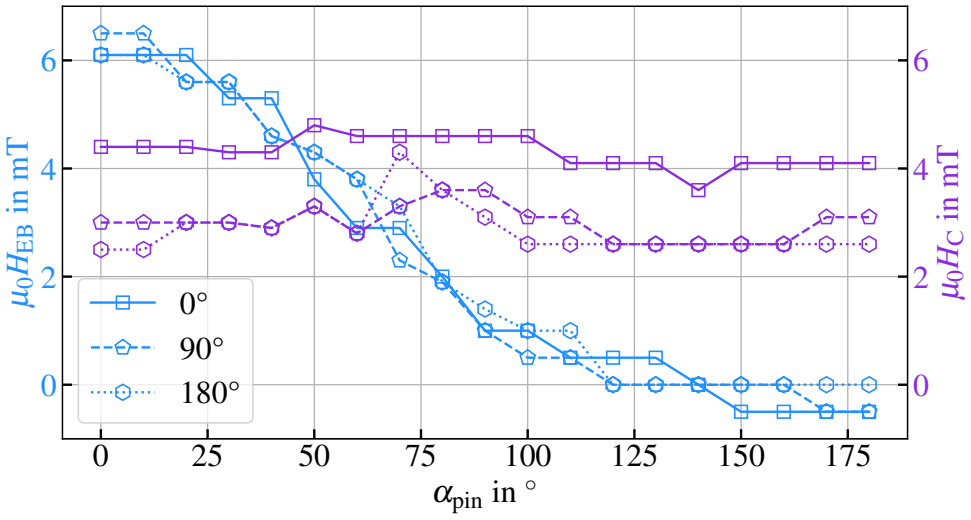

Figure 5.9: Shown is the simulated EB field (blue) and coercive field (violet) in dependence of α_{pin} for $\alpha_{rot} = 0°$ (solid line,square), 90° (dashed line, pentagon) and 180° (dotted line, hexagon).

EB field. The coercive fields are decreasing but only slightly with increasing angular distribution. The angular distribution of the pinned grains has a much larger influence and indicates that the pinned grains need to be aligned properly to show an EB effect, as it has been done experimentally for instance with FC.

5.2 Freestanding micro stripes

The main goal of this work is to understand the remagnetization behavior during magnetization reversal of freestanding EB micro stripes (see Fig. 5.10), as investigated experimentally by Sapida Akhundzada. In Fig. 5.10 the experimentally observed EB fields and coercive fields are plotted against the stripe width. Interestingly, the EB field is increasing with decreasing stripes width. In the modeling approaches so far this behavior has not been observed. Besides that, two different remagnetization behaviors for the hysteresis branches can be observed. On the decreasing field branch (DFB) nucleation takes place first on the center of the stripes. On the increasing field branch (IFB) nucleation takes place first on the edges of the stripes. In the following, this remagnetization behavior is simply called asymmetric. Several different approaches were attempted for reproducing the EB dependence and this remagnetization behavior.

First of all, a simple model was tried out, by simulating the EB effect by an additional field. Only the FM layer of the stripe was modeled with the parameters given above, neglecting the AFM layer. The stripe was simulated as a cuboid with dimensions smaller than the simulation volume. By this, the stray fields were also taken into account. The stripes were simulated with a width between 50 nm and 5 µm. The EB field was included with an additional field (custom

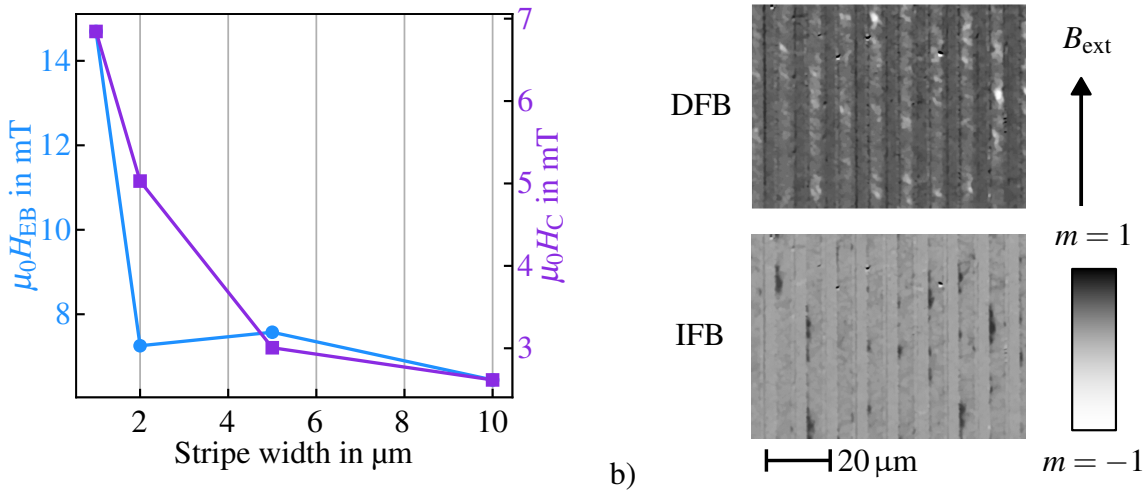

Figure 5.10: Experimental results for the freestanding EB mirco stripes obtained by Kerr microscopy. a) The dependence of H_{EB} and H_C on the stripe width is plotted. Especially the 1 µm stripes show a much stronger EB effect. b) The remagnetization behavior for the 5 µm stripes can be seen. On the DFB the nucleation starts in the middle of the stripes (white area), while in the IFB the nucleation starts on the edges (black area). Taken from [Akh22].

field). As expected the resulting EB field was constant and equal to the implemented custom field. The coercive field showed the expected inverse proportionality to the stripe width. Furthermore, the nucleation took place as expected, meaning nucleation first in the middle on both field branches. In summary, the experimentally observed effects cannot be explained by a constant EB field and changes in the stray field due to the width of the stripes.

Next up the model used for the full film simulations has been used to simulate the stripes, by limiting the dimensions in the y-direction between 500 and 2500 nm. In Fig. 5.11 the EB field and coercive field in dependence on the stripe width are plotted. As one can see, the EB field of about 6 mT is basically independent of the stripe width, maybe slightly decreasing with decreasing stripe width. The coercive field is increasing with decreasing stripe width due to increasing shape anisotropy. Starting at 6 mT for the 2.5 µm stripes, the coercive field is increasing to 12.5 mT at the 750 nm stripes. Besides that, the remagnetization behavior is not captured correctly within the simulations. The magnetic reversal is always starting in the middle of the stripes and not on the edges on the IFB as seen experimentally.

Since the above mentioned approaches did not show the desired behavior, the model was further changed. On the DFB the nucleation is retarded at the edges, while on the IFB the remagnetization begins at the edges, indicating different magnetic properties in the edges compared to the center of the stripes. This behavior can be understood by an increased exchange coupling between the AFM and the FM layer in a certain region on the edges. With decreasing stripe width, the relative influence of this region will increase, if one assumes that the size of this region is constant. With this assumption, both observations can be explained. The increase in the EB field due to the increasing influence of the edge region with decreasing stripe width and

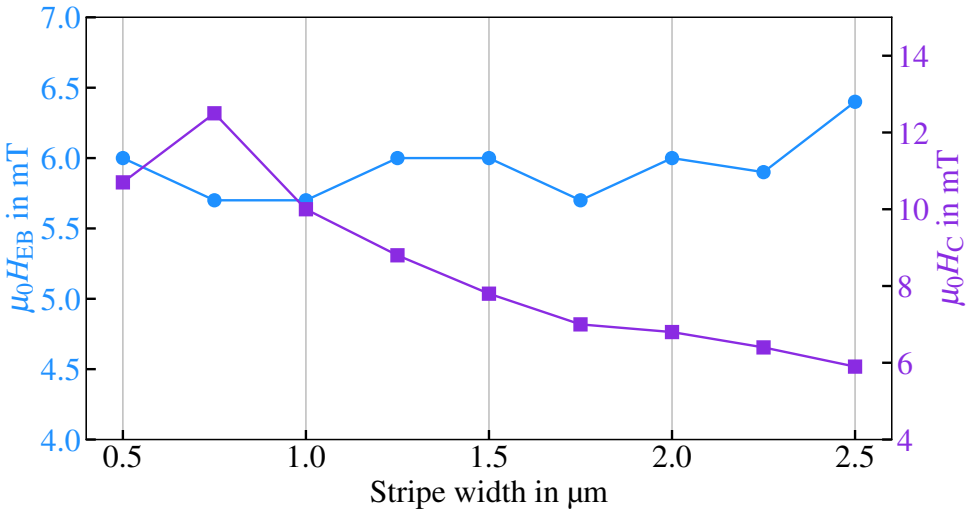

Figure 5.11: Shown is the simulated EB field (blue) and coercive field (violet) in dependence on the stripe width. The EB field is nearly constant around 6 mT, while the coercive field is increasing with decreasing stripe width from 6 mT to 12 mT.

the nucleation asymmetry due to the stronger EB effect. A possible reason for such a region could be the lithographical process leading to structural changes. In the following two different modeling approaches are presented and also experimentally investigated for plausibility.
The model introduced in Chap. 5.1 has to be extended. On each side of the geometry an edge region of 200 nm has been defined. In MuMax3 this was realized by assigning the first 100 regions to the edge region and the other 100 regions to the center part of the AFM interface layer. By this, all parameters could be varied in the edges independently of the center part. The FM layer was split into two regions in the same manner. Since the FM layer is not split into grains, only two region numbers were necessary. In Fig. 5.12 the extended model is sketched. In total two different parameters could be determined leading to the observed behavior. First, the number of pinned grains could be higher on the edges. Second, the saturation magnetization M_{FM}^{S} could be reduced. In the following, the two cases are investigated more closely. In Appendix 7.3 an example code for a stripe simulation with reduced M_{FM}^{S} in the edges is given.

5.2.1 Increased number of pinned grains

As shown in Sec. 5.1.1, the EB strength is increasing with an increasing number of pinned grains. When increasing the number of pinned grains in the edge region, the nucleation should show the desired asymmetry, and the EB strength should increase with decreasing stripe width. First of all, the remagnetization behavior was investigated. Therefore, the pinning in the edge region was varied from 10% to 90% in 10% steps for a 1.5 µm stripe. In Fig. 5.13 the nucleation of the DFB and IFB are shown for the pinning ratios of 10%, 30%, 60%, and 70%. In the middle region, the pinning ratio was kept at 30%. For a pinning ratio of 60%, the asymmetry starts to

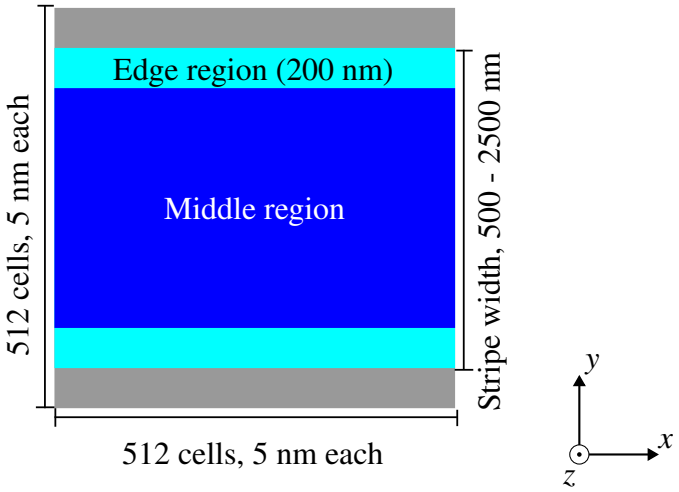

Figure 5.12: Schematic top view of the extended model for the stripes. The geometry is limited in the y-direction and an edge region of 200 nm has been defined with the possibility to define different material parameters. Besides that the layer structure and the number of cells is indicated.

occur, For a pinning ratio of 70% and higher, asymmetry is clearly visible. Below 60% the asymmetry is not present. This indicates that for the model presented here, the pinning ratio needs to be at least 60% in the edge region.

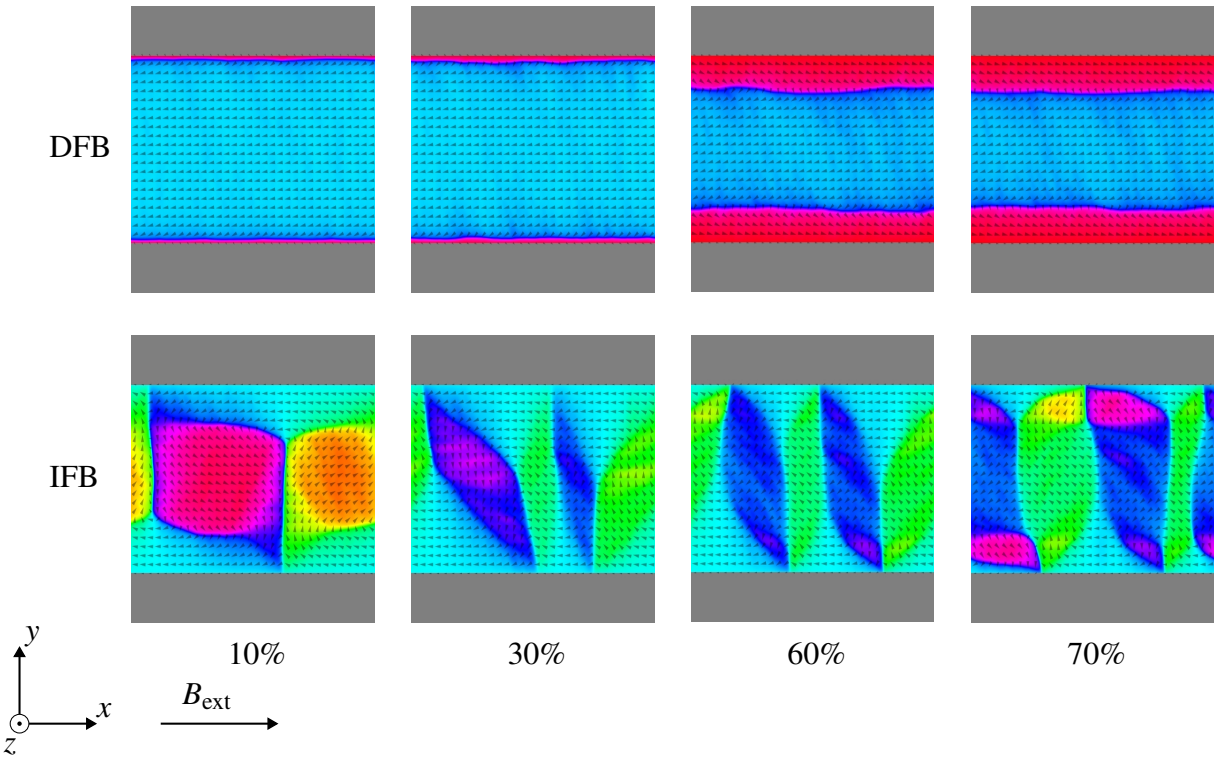

Figure 5.13: Remagnetization in the DFB and IFB for different pinning ratios in the edges. With pinning ratios of 10% and 30% the desired nucleation in the IFB can not be observed. At 60% the nucleation starts first in the edges and is even more pronounced at a pinning of 70%.

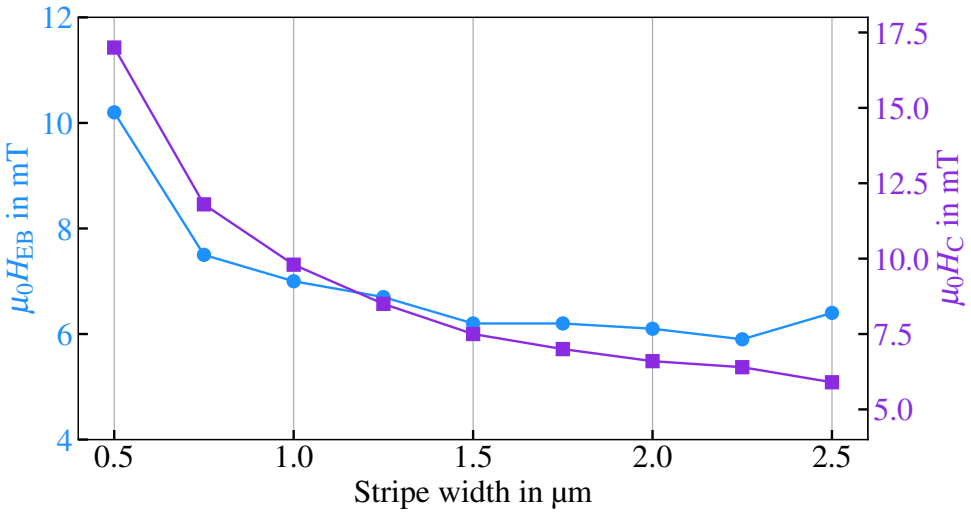

Figure 5.14: Simulated EB field (blue) and coercive field (violet) in dependence on the stripe width with increased number of pinned grains in the edge region.

This approach has then been used for simulations of different stripe widths ranging from 500 nm to 2500 nm, simulated with a pinning ratio of 60% pinned grains in the edges and 30% pinned grains in the middle. In Fig. 5.14 the resulting EB fields and coercive fields are plotted. The coercive fields show the expected inverse proportionality with the stripe width. The coercive field starts at 6 mT for the 2.5 µm stripe and increases to 17 mT for the 0.5 µm stripe. The EB field is also increasing with decreasing stripe width. For stripe widths above 1 µm, the EB field stays at about 6 to 7 mT and increases to 10 mT at 0.5 µm. This strong increase could also be observed experimentally as already shown in Fig. 5.10.

So far the influence of a higher pinning ratio in the edge region has been investigated. An open question is, whether this is a realistic assumption. In [Mer22a] and [Mer22b] it is shown, that the pinning of a grain is connected to the volume of a grain. A change in the grain size distribution on the edges of a stripe could then result in a higher number of pinned grains. In the following, a experimental study will be presented, investigating the grain size distribution for the edge and middle region of a 5 µm stripe. Assuming a columnar grain structure, the interface area of a grain is proportional to its volume and it is therefore sufficient to determine the interface area of a grain to get the grain's volume.

A sample of 5 µm stripes consisting only of the 5 nm Cu buffer layer and a 30 nm $Ir_{17}Mn_{83}$ layer has been fabricated. With an atomic force microscope the surface topology has been measured and further investigated by the watershed algorithm in Gwyddion [Gwy22] to extract the grain size distribution. Atomic force microscope images were measured on the left and right edges and in the middle of the stripes. Each measurement was repeated five times on different spots, which results in 15 measurements in total, to get a better distribution. The used atomic force microscope was a commercial Nanosurf FlexAFM. The contact mode was used

with a Nanosensors PPP-CONTR tip. The image size was set to 1024 x 1014 Px and a total area of 500 nm x 500 nm was scanned, resulting in an ideal resolution of about 0.5 nm x 0.5 nm. In Fig. 5.15 a) the raw data of the 'middle' measurement is shown. Compared to [Mer22a] the grain structure cannot clearly be seen. Within the time of the work, a comparable grain image could not be reproduced as shown in [Mer22a], even by using the same parameters the sputtering process and measurement parameters. Nonetheless, the results will be presented. The raw data needs to be further optimized before the watershed algorithm can be applied, as described in [Mer22a]. After applying a Gaussian filter [Gwy22], a sharpening [Gwy22] (both with a filter size of 2.5 nm) was performed. In Fig. 5.15 b) the result can be seen. Afterward, the watershed algorithm was applied and segmentation was performed. Since the filter size of the Gaussian and sharpening filter was set to 2.5 nm, the minimum grain area is given by $A = \pi r_{\text{min}}^2 = 19.63\,\text{nm}^2$, as described in [Mer22a]. With the given resolution, this results in $A \approx 82\,\text{Px}^2$. Further, for the watershed algorithm, the minimum droplet size was set to 10% and a step number of five. For the segmentation, a step amount of 50 was set with a droplet size of 10%. The parameters were chosen according to [Mer22a], to be able to compare the results. The final step is the application of an inversion mask. Gwyddion also allows to directly extract the grain radius distribution. In Fig. 5.16 the resulting distributions for the left, right and middle regions are plotted. As can be seen, the determined radius distribution is quiet noise. To make a statement on whether the distribution is different for the three cases, a lognormal function of type

$$p(r) = \frac{C}{\sqrt{2\pi}\sigma r} \exp\left(-\frac{(\ln r - \mu)^2}{2\sigma^2}\right), \tag{5.2}$$

with proportionality factor C, standard deviation σ and expected value μ, has been fitted onto the three distributions using the 'curvefit' function in the scipy package [Sci23] and python [Pyt23]. In Tab. 5.1 the determined parameters are given. For the left edge, a peak grains radius of (5.63 ± 0.19) nm, for the right side, a peak radius of (5.70 ± 0.08) nm, and for the middle region, a peak radius of (5.39 ± 0.09) nm was determined. Comparing the three, indeed a small

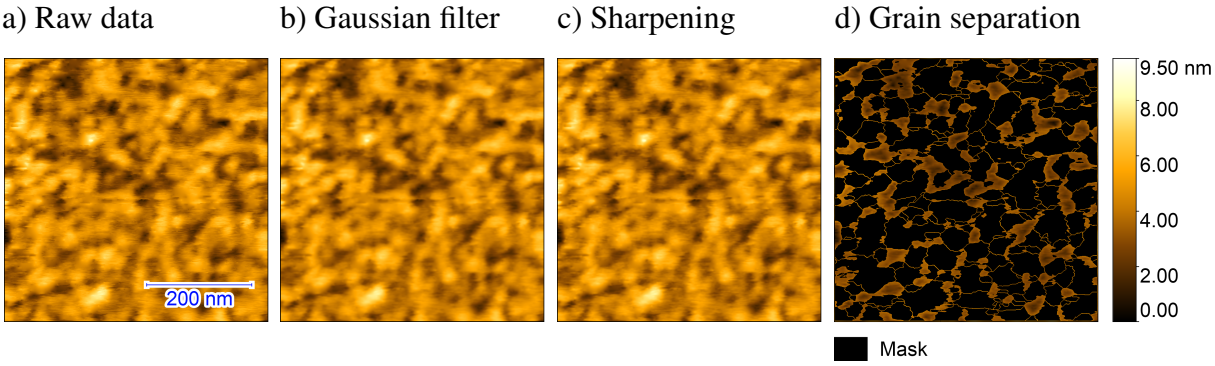

Figure 5.15: Method to extract the grain radius distribution. a) The raw data gained by atomic force microscopy is shown. After applying a Gaussian filter (b) and a sharpening (c), the watershed algorithm was applied to extract a mask for the grains (d).

difference is present. Taking into account that the grains are not perfect cylinders and that this measurement technique is only imaging the surface topology and not directly the magnetic AFM grains, a clear statement cannot be made here. All in all the simulations indicate that higher pinning in the edge region can be a possible explanation for the remagnetization behavior and the increase of the EB field with decreasing stripe width. The measured grain radius distribution indicates a small change in the grain radius within the measurement results. Nonetheless, the difference is rather small and it is not clear if this small difference actually leads to a change in the pinning ratio.

Table 5.1: Determined parameters C, μ and σ for the lognormal function.

Region	C in a. u.	σ in nm^{-1}	μ in nm
right	473 ± 24	0.531 ± 0.023	1.984 ± 0.026
mid	393 ± 20	0.582 ± 0.025	2.022 ± 0.029
left	467 ± 23	0.589 ± 0.023	2.054 ± 0.026

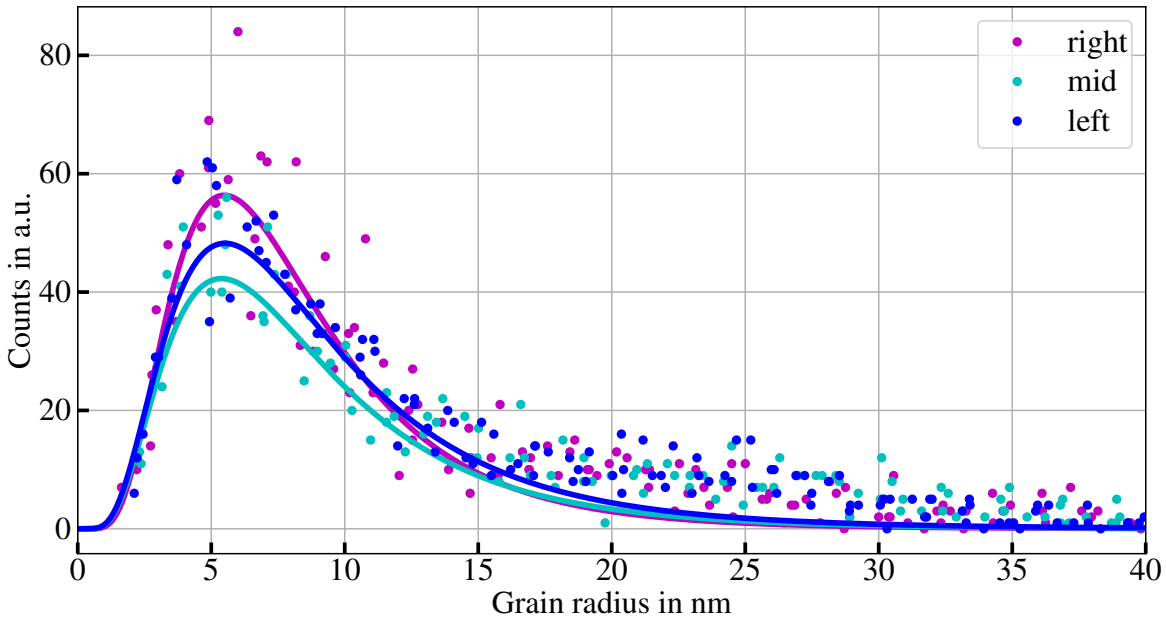

Figure 5.16: Plot of the counted grains against their radius for the right edge (purple), middle region (cyan) and left edge (blue). Furthermore, lognormal functions as given in Equ. (5.2) are fitted.

5.2.2 Decreased M_{FM}^{S}

The second approach results in a decreased saturation magnetization in the edge regions. As explained earlier, the EB field is given by

$$H_{\mathrm{EB}} = -\frac{J_{\mathrm{EB}}}{M_{\mathrm{S}} t_{\mathrm{F}}}, \tag{5.3}$$

when considering the simple Meiklejohn and Beam model. A reduction of the saturation magnetization leads to an increase of the EB field, since $H_{\mathrm{EB}} \propto 1/M_{\mathrm{S}}$. A reduced saturation magnetization in the edge region should therefore lead to the observed asymmetric nucleation and the increasing EB effect with decreasing stripe width. First, the influence of the saturation magnetization on the remagnetization behavior was investigated. For the 1.5 µm stripe, simulations were performed with reduced $M_{\mathrm{S,edge}}$ ranging from only 10% to 90% of the theoretical value of $M_{\mathrm{S}}^{NiFe} = 798\,\mathrm{kA/m}$. The pinning was kept at 30% in both regions. All other parameters are the same as in the simulations before. The most important results are summarized in Fig. 5.17. For all investigated $M_{\mathrm{S,edge}}$, magnetic remagnetization started in the middle for the DFB. On the IFB, remagnetization normally takes place also in the middle of the stripes, but with decreasing $M_{\mathrm{S,edge}}$, remagnetization starts increasingly on the edges, as it is desired for the experiments. At only 60% the asymmetry is strongly visible. For the simulations, this reduction will be used.

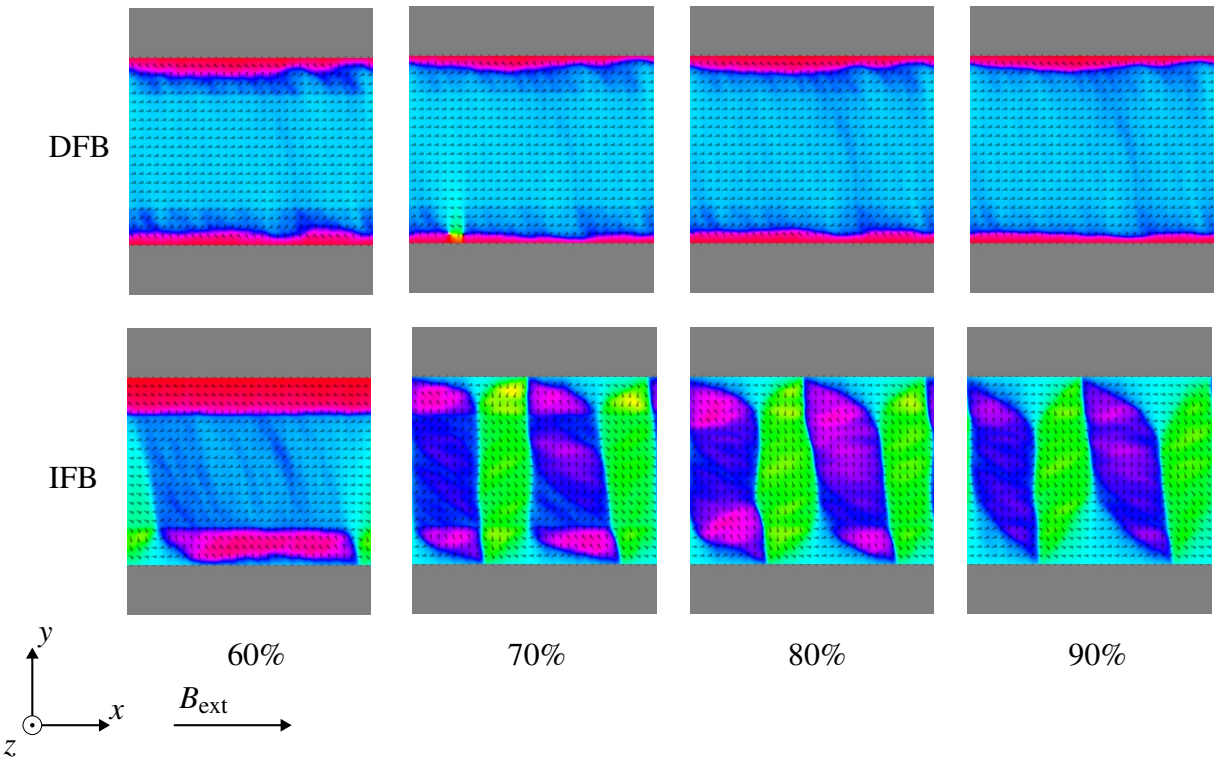

Figure 5.17: Remagnetization in the DFB and IFB for different reduced saturation magnetizations $M_{\mathrm{S,edge}}$ from 60% to 90% of M_{S} in the edges.

After showing that a reduced $M_{\mathrm{S,edge}}$ leads to the expected remagnetization, the idea will be ap-

plied to different stripe widths. With $M_{S,edge} = 0.6 M_{S,middle}$ stripes were simulated from 0.5 µm to 2.5 µm. In Fig. 5.18 the resulting coercive and EB fields are plotted against the stripe width. With decreasing stripe width, both fields are increasing. The coercive fields reach from 6.4 mT at 2.5 µm to 19.5 mT at 0.5 µm. In the EB field only a small increase is visible for stripe widths between 1.0 µm and 2.5 µm , but below 1.0 µm the EB field is strongly increasing up to 10.7 mT for the 0.5 µm stripe. The resulting fields are comparable to the experimental results given in Fig. 5.10. This indicates the appropriateness of the chosen parameters.

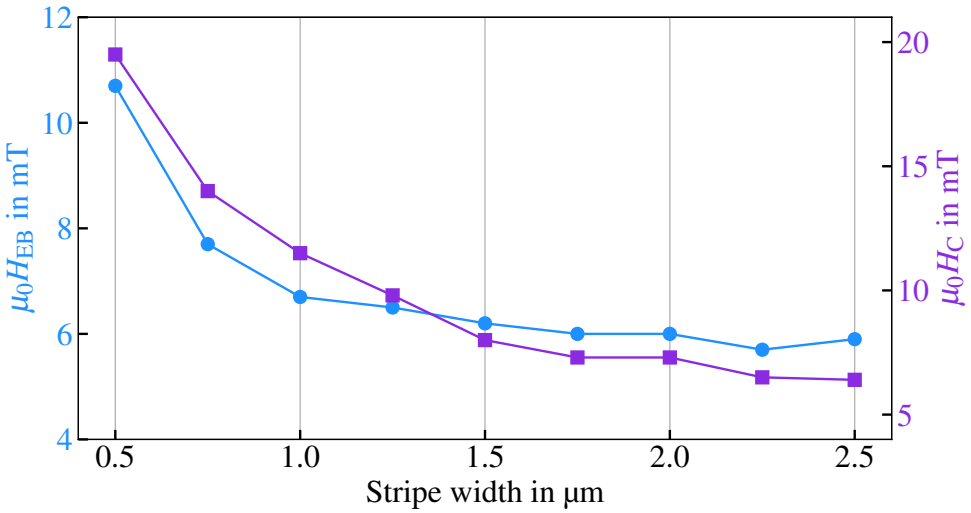

Figure 5.18: Simulated EB field (blue) and coercive field (violet) in dependence on the stripe width with decreased saturation magnetization in the edge region.

To experimentally investigate the possible reduction of the saturation magnetization, stripes of different widths have been fabricated. For each sample, the magnetic moment was measured in a VVSM. By knowing the sample volume, layer thickness, and the stripe width, the magnetic volume can be determined and the saturation magnetization normalized to the magnetic volume can be calculated. By assuming a constant edge region of reduced M_S, the calculated M_S should increase with increasing stripe width. In the following, the measurement procedure and the results are layed down in detail.

By optical lithography, freestanding stripes with a width of $1, 2, 5$, and 10 µm have been fabricated as explained in Chap. 3.1.3. The sample size was determined by a light microscope, resulting in sample dimensions given in Tab. 5.2. The samples were then investigated further in a VVSM. Hysteresis loops were measured, delivering results for the magnetic moments in saturation along the easy axis. To find the easy axis the loops were measured for different angles between 0○ and 360° in 3° steps. The results for the easy axis magnetic moments are also given in Tab. 5.2. Besides the sample dimension and its magnetic moment in saturation, the magnetic volume needs to be known in order to determine the saturation magnetization. With an atomic force microscope, the stripe's widths and the spacings between the stripes were measured. The non-contact mode was used. The image size was chosen to be big enough to cover at least

two stripes and one spacing between them. The resolution was about 20 nm (5 nm for the 1 µm stripes), resulting in a precise determination of the widths. For each sample, five spots were measured. By extracting a line profile in Gwyddion and fitting a step function, the width could be determined. The resulting widths were average and the error was further estimated by the sum of the maximum deviation of the measured widths from the average, the resolution of the atomic force microscope, and the fitting error. The results are listed in Tab. 5.2. Typically the stripe width is larger than expected by the lithographic mask, being a result form the different process steps in the lithography. Extending on that, the ratio between the magnetic and non-magnetic material could be determined and multiplied by the sample dimensions, resulting in an approximation of the magnetic volume. Dividing the determined magnetic moment in saturation with the magnetic volume leads to the saturation magnetization for each sample. The final results are listed in Tab. 5.3. When taking a look at the determined saturation magnetization, one can notice that it is increasing with increasing stripe width. If one assumes an edge region of constant size for all stripes, then one can conclude that the edge region possess a reduced saturation magnetization.
All in all it can be stated that the idea of an edge region with reduced saturation magnetization is in agreement with the experimental results described above. Simulations show the expected nucleation asymmetry and the increasing EB effect with decreasing stripe width.

Table 5.2: Measurement results for the sample area, stripe width, spacing and the portion of the magnetic volume.

Sample	Sample area	Stripe width	Spacing	Magnetic volume in %
1 µm	$(15.2 \pm 0.2)\,\mathrm{mm}^2$	$1.79 \pm 0.16\,\mu\mathrm{m}$	$0.21 \pm 0.08\,\mu\mathrm{m}$	90 ± 19
2 µm	$(17.6 \pm 0.2)\,\mathrm{mm}^2$	$2.61 \pm 0.14\,\mu\mathrm{m}$	$1.34 \pm 0.12\,\mu\mathrm{m}$	66 ± 8
5 µm	$(21.4 \pm 0.3)\,\mathrm{mm}^2$	$6.51 \pm 0.13\,\mu\mathrm{m}$	$3.33 \pm 0.15\,\mu\mathrm{m}$	66 ± 3
10 µm	$(13.3 \pm 0.2)\,\mathrm{mm}^2$	$11.7 \pm 0.3\,\mu\mathrm{m}$	$8.7 \pm 0.3\,\mu\mathrm{m}$	57 ± 3

Table 5.3: Determined values for the magnetic moment in saturation and the corresponding saturation magnetization.

Sample	magnetic moment	Saturation magnetization
1 µm	$(4.89 \pm 0.04) \cdot 10^{-2}\,\mathrm{emu}$	$(360 \pm 80)\,\mathrm{kA/m}$
2 µm	$(5.44 \pm 0.04) \cdot 10^{-2}\,\mathrm{emu}$	$(465 \pm 65)\,\mathrm{kA/m}$
5 µm	$(7.08 \pm 0.08) \cdot 10^{-2}\,\mathrm{emu}$	$(500 \pm 37)\,\mathrm{kA/m}$
10 µm	$(4.36 \pm 0.05) \cdot 10^{-2}\,\mathrm{emu}$	$(571 \pm 45)\,\mathrm{kA/m}$

5.3 Embedded micro stripes

Besides the freestanding stripes, embedded stripes have been investigated. As explained in Chap. 3.1.4, the embedded stripes were fabricated by IB at a dose of $2 \cdot 10^{16}$ ions/cm^2. The stripes have a width of $1, 2, 5$ and $10\,\mu$m, with a spacing equal to their width. In Fig. 5.19 a measured hysteresis loop for the $5\,\mu$m embedded stripes is plotted. The loop show a double hysteresis structure, where the upper part corresponds to the magnetization reversal in the bombarded areas. In those areas is the EB effect destroyed and the coercive field is strongly reduced to about 2 mT. The lower part of the hysteresis corresponds to the non-bombarded areas. Here, the EB is still present. When comparing the different widths, it can be noticed that the coercive field of the bombarded area is independent of the stripe's width. For the non-bombarded areas, the coercive field is increasing with decreasing stripe width from 6 mT to 10 mT. The EB strength is decreasing with decreasing stripe width from 7 mT to 5 mT. This is the first difference to the freestanding stripes, where the EB field was increasing with decreasing stripe width. The second difference can be found in the remagnetization behavior. In Fig. 5.20 the remagnetization behavior across a hysteresis loop is shown. First of all, the bombarded area is flipping, while the stripes keep their magnetization. On the DFB the nucleation in stripes then starts again in the middle, like in the freestanding ones. But on the IFB the nucleation also starts in the middle of the stripes. Further, the magnetic reversal of the remaining non-bombarded area is starting on the already nucleated stripes and quickly flips the complete bombarded area.

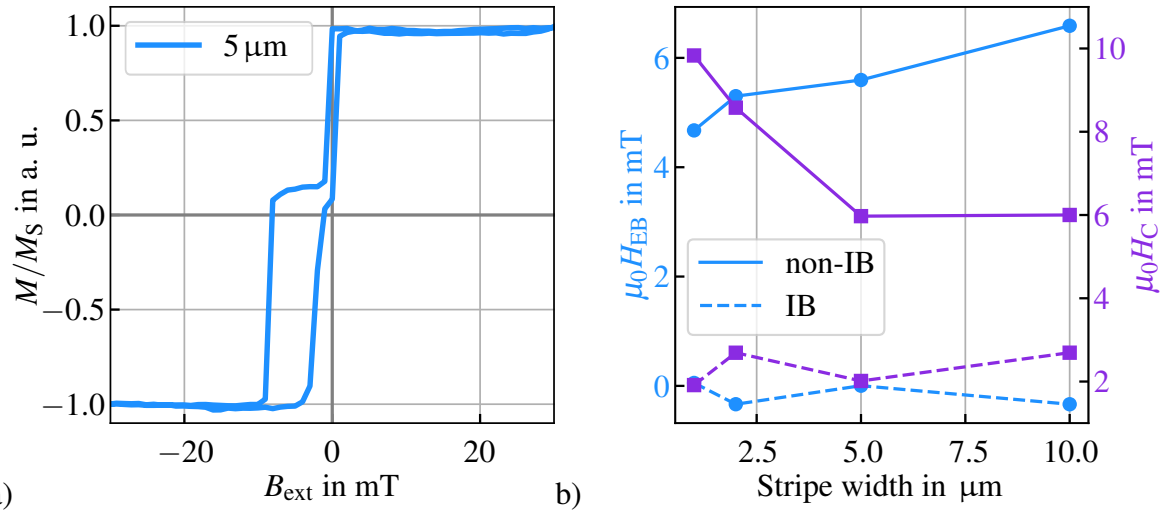

Figure 5.19: a) Experimentally measured hysteresis loops with Kerr microscopy for the $5\,\mu$m embedded stripes. The observed double hysteresis structure corresponds to the remagnetization in the bombarded and non-bombarded areas. b) The determined values for the EB and coercive field are plotted against the stripe width. The bombarded area (dash line) process much smaller coercive fields and a vanishing EB effect.

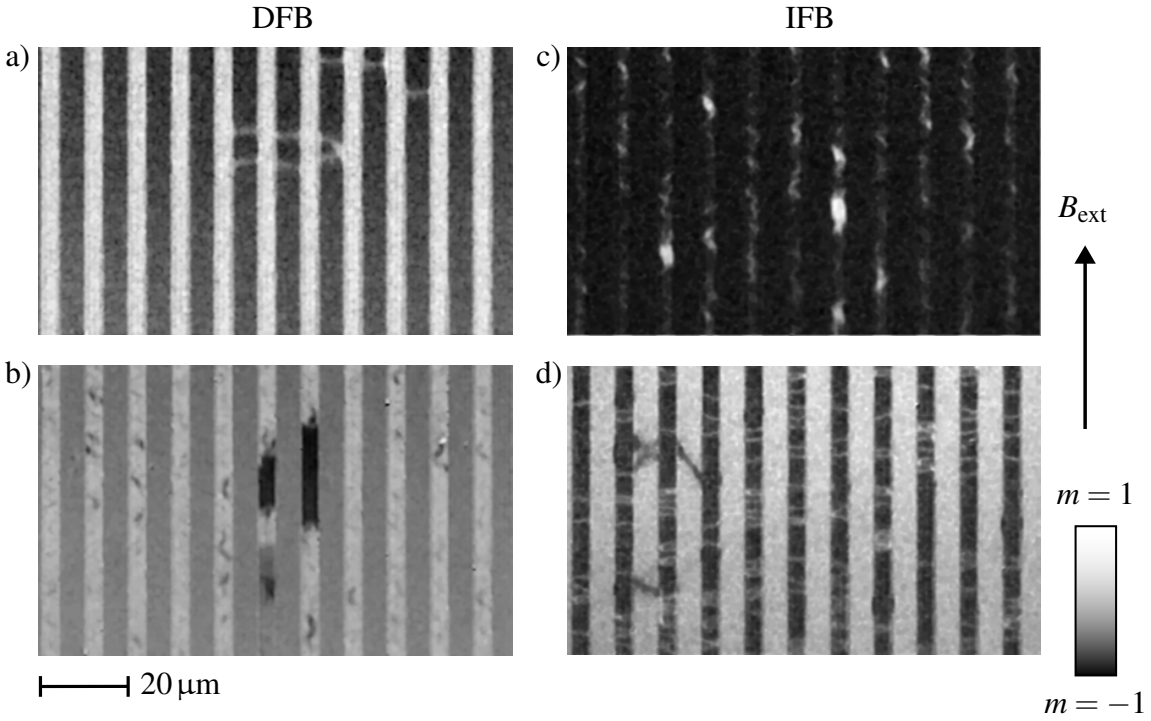

Figure 5.20: Remagnetization behavior observed in the Kerr microscope by Sapida Akhundzada on 5 µm embdded stripes. In the DFB, first, all the bombarded areas are remagnetizing (a, black area) followed by nucleation in the middle of the actual stripes (b). On the IFB again the stripes nucleate first in the middle (b, white), followed by the bombarded area (d).

To model the observed behavior correctly, again, the model has been modified. The basic principle is the same as in the simulations before. The simulation volume and its discretization stay unchanged. The model considers two different regions. One for the bombarded area and another one for the non-bombarded area, or the actual stripe. The actual stripe is centered in the simulation volume and is only limited in its y-dimension. All material parameters are kept similar to the full-film simulation or like in the middle region of the freestanding stripes. The AFM layer is split into grains, which are either pinned or rotatable and interact with the lowest FM layer, still with a pinning ratio of 30%. The rest of the volume is filled with the same layer system, but with modified material parameters to simulate the IB, which is destroying the EB effect [Huc18, Mü18]. This is incorporated by setting the interface exchange interaction between the AFM and FM layers to zero, meaning that the AFM and FM layers are not interacting with each other. Furthermore, a reduction of the saturation magnetization can be observed [Mü16]. Therefore, the saturation magnetization is reduced to 30% in the bombarded area, which was chosen to match the experimental observations. Lastly, the exchange stiffness was reduced to 50% to simulate material mixing and defect creation [Lel14]. In Fig. 5.21 the changed model is sketched.

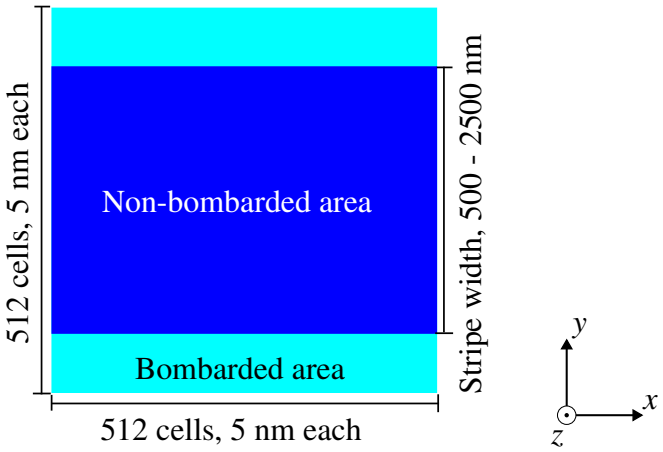

Figure 5.21: Sketch representing the model (top view) for the embedded EB stripes. The actual stripe is centered in the middle of the simulation volume and modeled exactly like in the full-film simulation. The width ranges from 0.5 µm to 1.5 µm. The rest of the simulation volume is filled with the same layer system, but with reduced exchange stiffness A_{ex} and saturation magnetization M_S. Besides that, the interface interaction is deactivated between the FM and AFM layers.

Simulations were then performed for stripe width ranging from 0.5 µm to 1.5 µm. In Fig. 5.22 a) a hysteresis for the 1.2 µm stripe is plotted. The expected double hysteresis structure is clearly visible. The upper part corresponds to the bombarded area and the lower part corresponds to the non-bombarded area. The bombarded area possess a nearly vanishing EB field of 0.6 mT and a small coercive field of 2.3 mT. The actual stripe has an EB field of 6.6 mT and a coercive field of 12 mT. All values close to experimentally observed values, validate the appropriateness of the chosen material parameters. In Fig. 5.22 the remaining results for the other stripe

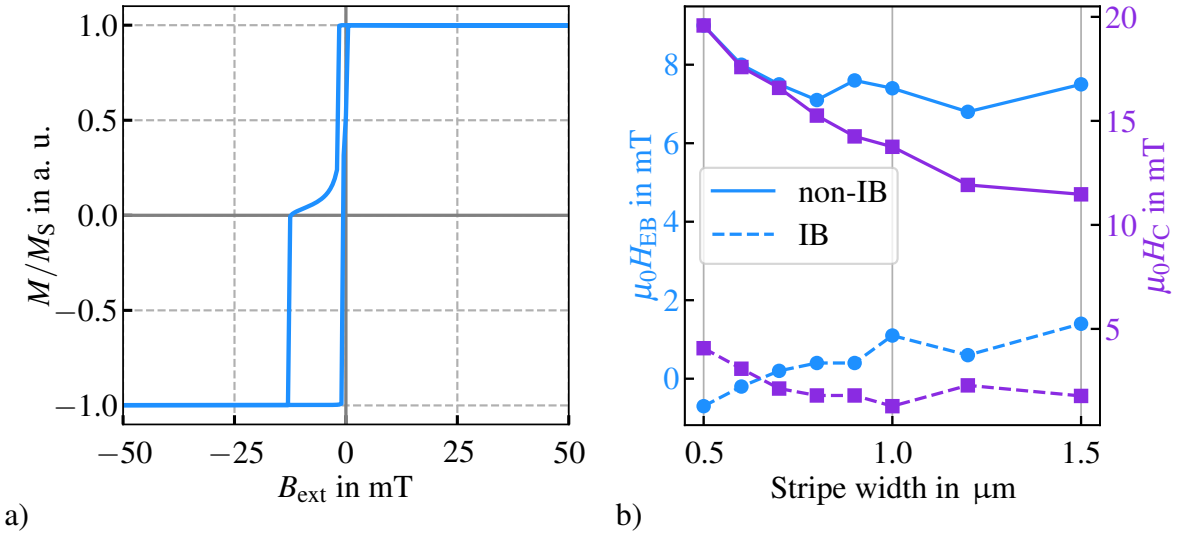

Figure 5.22: a) Simulated hysteresis loop for a 1.2 µm embedded EB stripe. b) The resulting EB and coercive fields of the bombarded and non-bombarded areas for the different stripe widths are plotted.

widths are plotted. Similar to the experiments, the coercive field of the non-bombarded area is increasing with decreasing stripe width, generally being larger than in the experiments, even though the stripes are smaller in the simulations. The EB field is more or less constant around 8 mT and is therefore 2 mT larger than experimentally observed. The bombarded area shows a nearly vanishing EB field for all stripes, as expected experimentally. The slight EB effect is connected to the interaction between the bombarded and non-bombarded FM layers and their exchange stiffness. The coercive fields of the bombarded area are at about 2.5 mT and match the experimental observations very well.
Finally, the resulting remagnetization behavior will be investigated. In Fig. 5.23 images of the FM magnetization on the DFB and on the IFB for a 1.5 µm stripe are given, showing the most important states. Unfortunately, the nucleation is not that clearly visible in the non-bombarded area, but a trend can be identified. At −3.5 mT the bombarded area is remagnetizing by an instant spin-flip and at −12 mT the non-bombarded area starts to nucleate in the middle. On the IFB the non-bombarded area starts to nucleate in the middle at −2 mT as well and is followed by a spin-flip or fast rotation of the bombarded area at −0.5 mT. The remagnetization behavior observed in the experiments could therefore be reproduced by the simulations.

It can be summarized, that the model presented here is capable of modeling embedded EB micro stripes that are fabricated by IB. The calculated fields are close to experimentally observed values and also the trends could be captured. Besides that, the magnetic reversal also takes

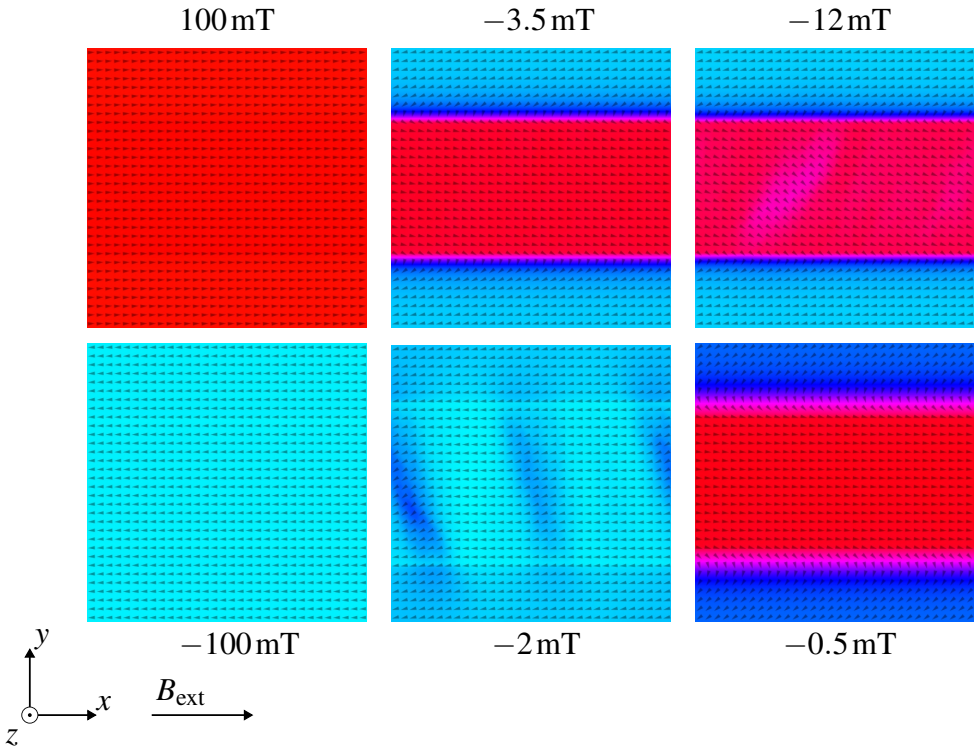

Figure 5.23: Simulated images of the FM magnetization at different external magnetic field strengths B_{ext}. The expected remagnetization behavior can be seen.

place like in the experiments.

5.4 Freestanding squares and discs

Besides the freestanding stripes, other geometries have been investigated experimentally. A closer look will now be taken towards freestanding squares and discs. The main difference between those geometries and the stripes is a further spacial limiting in the x-direction. As explained in Sec. 3.1, the geometries have been fabricated by sputtering and a lithography process. Instead of a lithography mask, electron beam lithography was used (see Chap. 3.1.3 or [Gau17] for more details). Of special interest is the modeling of the hysteresis loop and the nucleation. In Fig. 5.24 and 5.25 hysteresis loops and Kerr images of the nucleation processes can be seen for geometries of 1 µm and 10 µm size.

First, a closer look at the squares will be taken. The 10 µm squares possess a much larger EB field compared to the 1 µm ones. While the 1 µm squares have an EB field of 0.6 mT, the EB field for the 10 µm squares reaches 5.0 mT. The experimental results presented here are not final, meaning that the FC parameters might be not optimal. Considering this, the EB effect of the 1 µm squares might be increased in further experiments. Taking a look at the coercive fields, it can be noticed that the coercive field in the 1 µm squares is slightly larger, reaching 2.9 mT compared to 2.3 mT in the 10 µm squares. Taking a look at the nucleation processes, differences compared to the stripes can be seen. On the DFB, nucleation starts on the edges of the squares parallel to the field direction. On the IFB, the nucleation starts in the middle. This is the complete opposite as seen in the stripes.

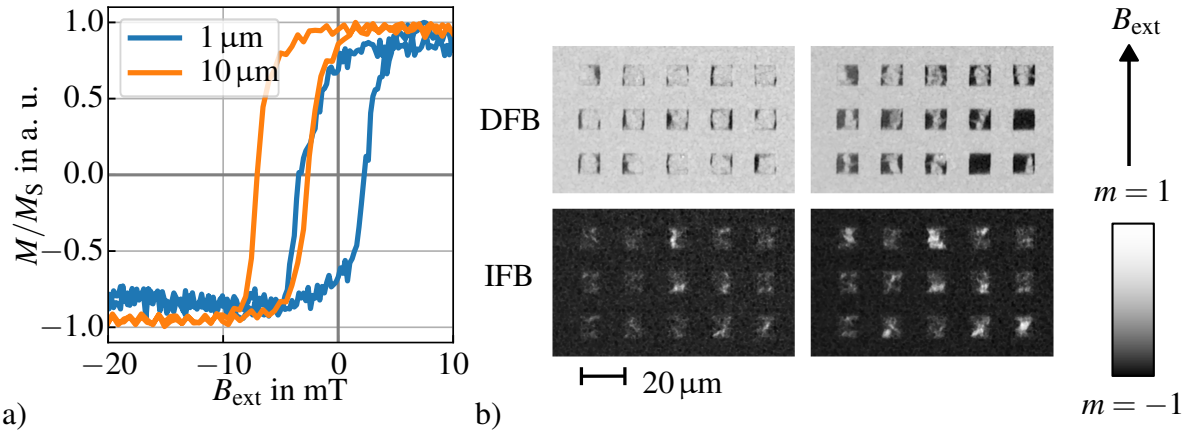

Figure 5.24: Plot of the measured hysteresis of the 1 and 10 µm square geometries (a) and Kerr images of the nucleation process for the DFB and IFB (b). The field direction is indicated by the arrow on the right side.

When taking a look at the discs, one can notice a clear difference between the 10 µm and 1 µm again. Not only is the EB field much smaller, but the shape of the hysteresis loop is also differ-

ent. The hysteresis loop for the 10 µm discs is similar to the squares, with an EB field of 4.5 mT and a coercive field of 2.3 mT. The hysteresis loop of the 1 µm discs possesses a small EB field of 0.3 mT in the opposite direction and a coercive field of 1.8 mT. Besides changes in the two fields, the shape is different. The structure shows a slight double hysteresis. Again, it needs to be emphasized that the FC parameters might not be optimal for the geometries. Taking a look at the nucleation, the overall process is the same as for the squares. On the DFB, the nucleation starts on the edges, while on the IFB the trend is not that clearly visible. Some of the discs start to nucleate on the edges and some nucleate first in the middle. An explicit statement can not be made.

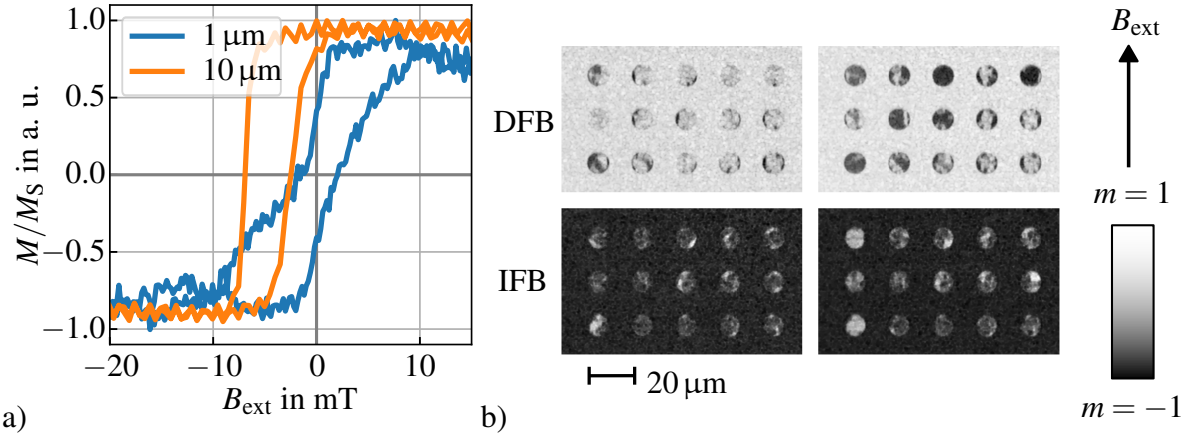

Figure 5.25: Plot of the measured hysteresis of the 1 and 10 µm disc geometries (a) and Kerr images of the nucleation process for the DFB and IFB (b). The field direction is indicated by the arrow on the right side.

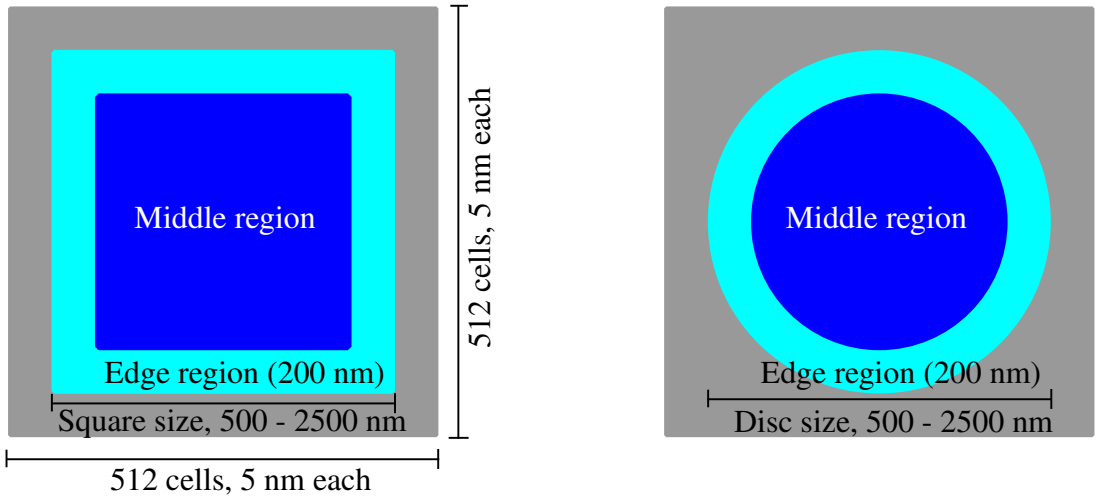

Figure 5.26: Schematic visualizing the simulation approach for the squares and discs (top view). The total simulation size is again 2.56 µm x 2.56 µm, while the geometries have a total size of 0.5 µm to 2.5 µm. For both geometries the edge region has been defined with a size of 200 nm.

The simulation approach is still the same as in the case of the freestanding stripes, meaning that the layer system and all material parameters are in general the same. This time, a further spatial limiting in the x-direction was defined and the edge region of 200 nm was defined in the x-direction as well. In Fig. 5.26 the changes in the model are visualized for the squares and discs. Since the remagnetization behavior is different compared to the freestanding stripes, different parameters need to be chosen. Since the nucleation is opposed to the freestanding stripes, the idea of a stronger EB in the edges is discarded and replaced by a smaller EB effect in the edges. The smaller EB effect was simulated by a reduced pinning ratio in the edge region. In the middle region, the pinning was kept at 30%, while in the edge region, the pinning was reduced to only 5%. In Fig. 5.27 a simulated hysteresis loop for a 2 µm square is plotted. The EB field can be determined to 5.8 mT with a coercive field of 4.0 mT and is thereby comparable with the experimental result of 5.0 mT for the 10 µm squares. The coercive field is larger than the experimental values for both the 10 µm squares and the 1 µm stripes. Besides that, the simulated hysteresis loop is rounder that the experimental one, indicating slower remagnetization. In Fig. 5.27 the remagnetization process is shown. Unfortunately, the observed nucleation could not be reproduced. On both field branches, the remagnetizations starts on the edges perpendicular to the field. Afterward, a domain wall motion across the square can be observed, moving towards the middle. The edges parallel to the field remagnetize at last. On the IFB, the situation is the same as on the DFB but follows experimental observations.

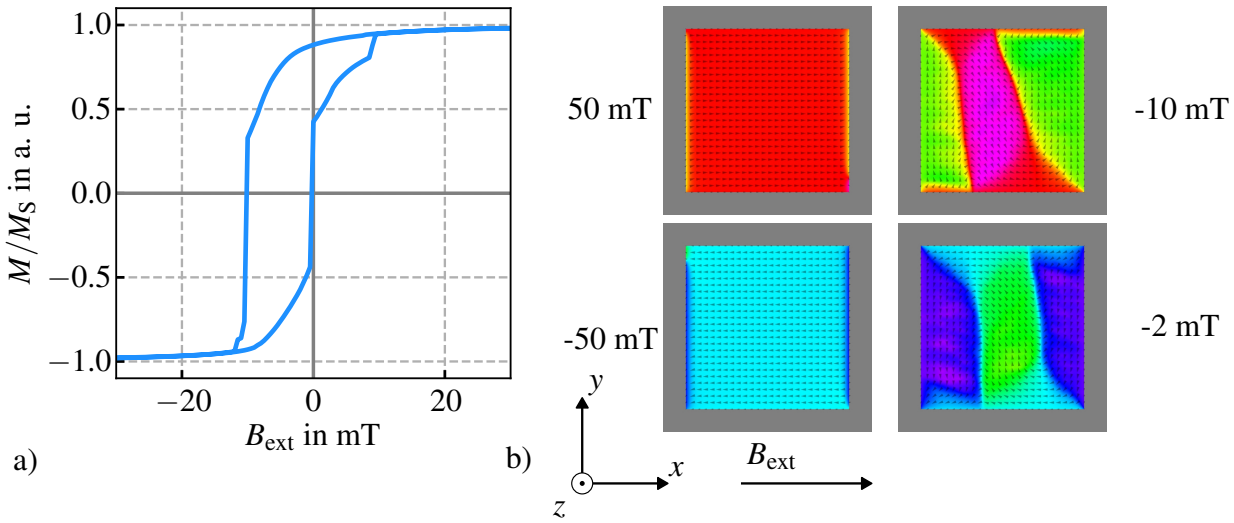

Figure 5.27: a) Simulated hysteresis loop for the 2 µm square. b) Images of the magnetization at different field strength are shown.

Next, a look is taken at the discs. The simulation is nearly the same as in the case of the squares, but instead of a cuboid a cylinder has been used for the geometries. In Fig. 5.28 the obtained hysteresis loop and images of the remagnetization for a simulated 2 µm disc are given. Compared to the squares the EB field is stronger, reaching 6.2 mT, and the coercive field is

weaker with 3.2 mT. Besides that, the hysteresis loop is much sharper. Experimentally there was no significant difference in the loops for the 10 µm squares and discs. The difference in the simulation might be reasoned by the different geometries and how they are discretized. In the finite-difference method, all cells have the same size. For the discs, this leads to rough surfaces, since the curve is modeled by cells of 5 nm size. Opposed to that, the surface of the squares is perfectly flat. This roughness is destabilizing the surface spins in the discs, leading to smaller coercive fields and a sharper hysteresis loops. Taking a look on the remagnetization process, one can see a difference to the square. On the DFB, nucleation starts to occur on the top edge and a domain wall motion across the disc can be observed. On the IFB, remagnetization starts again on the top but also on the bottom edge. Since the remagnetization takes place within one simulation step, no further details are accessible, giving insights into the further remagnetization process.

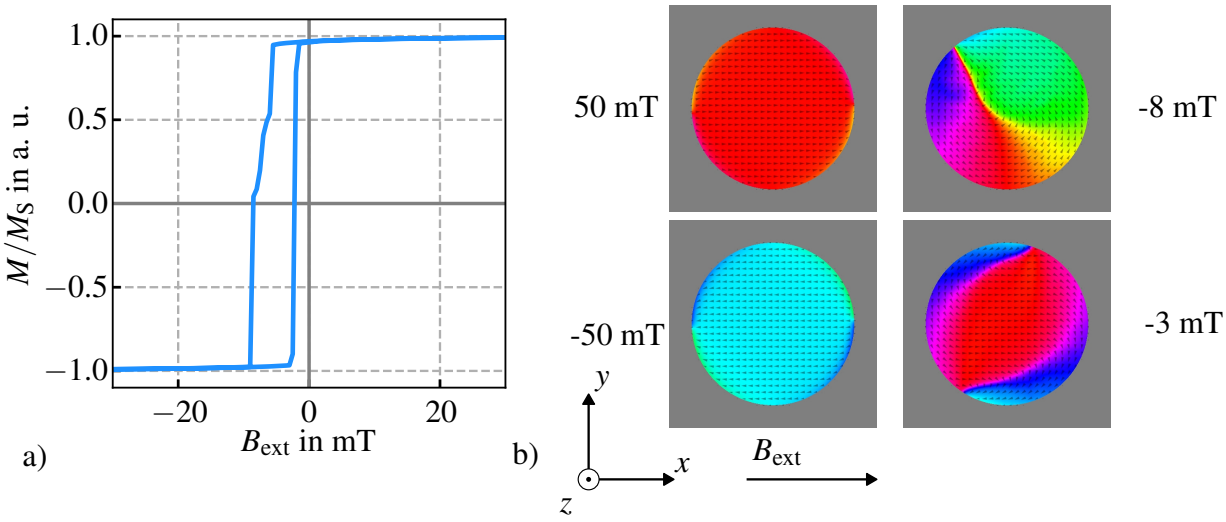

Figure 5.28: a) Simulated hysteresis loop for the 2 µm disc. b) Images of the magnetization at different field strength are shown.

An open question is the dependence of the EB field and the coerceive field on the geometry size. Simulations were performed for geometry sizes of 0.5 µm to 2.5 µm. In Fig. 5.29 the resulting EB fields (blue) and coercive fields (violet) for the squares (solid line) and the discs (dashed line) are plotted. As has been the case for the 2 µm geometries, the coercive field of the discs is always smaller than for the corresponding square. The EB fields do not show a clear trend, a small decrease with decreasing size might be visible for the squares.

In summary, further geometrical structures like squares and discs have been simulated. The experimentally observed squares and discs were modeled again with an edge region possessing different parameters. Especially the simulated hysteresis for the squares matches the experimentally observed one. The simulated discs show much smaller coercive fields and the hysteresis loop is not fitting the experimentally observed one. Unfortunately, the remagnetization process could not be modeled in detail. On the DFB, the remagnetization is not showing the same nucleation as in the experiments. Here, it needs to be kept in mind, that the experimentally

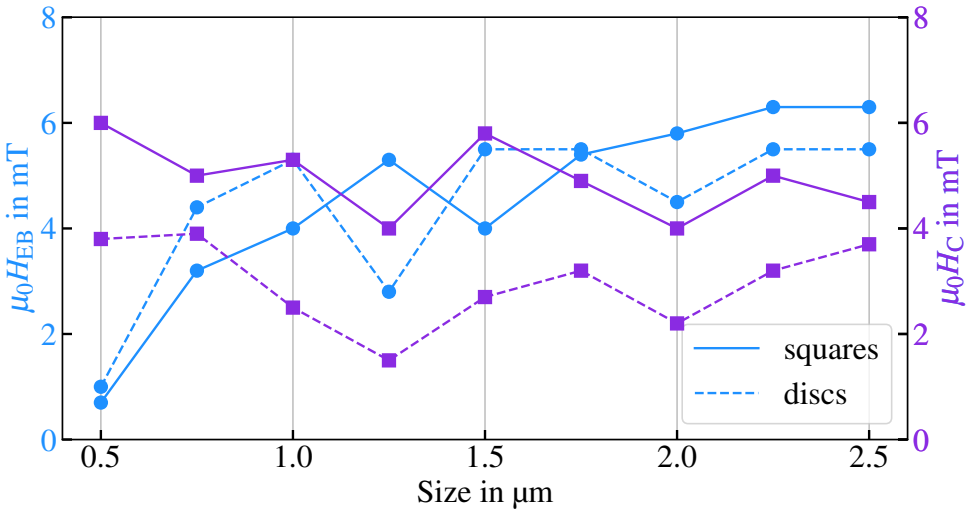

Figure 5.29: Simulated dependency of the EB field (blue) and coercive field (violet) for the freestanding squares (solid line) and discs (dashed line) on their size.

investigated structures were larger then the simulated ones. The Kerr images show 10 µm geometries, while the simulation was limited to 2.5 µm. The optical resolution limit of the Kerr microscope is further limiting the comparability. Changes to the model might improve the simulation results. Nonetheless, simulations for other sizes were performed and can be compared to experiments in the future.

5.5 Embedded squares and discs

In this final section, simulations of embedded squares and discs will be presented. Until now, no experimental results are present. The simulation results are therefore a possible forecast for future experiments. In Sec. 5.3 the embedded stripes have been simulated, showing great agreement with the experimental results and the simulation will therefore be adapted to embedded squares and discs following the same idea. The layer system and all material parameters are completely the same, only the geometries are different. For the squares, a cuboid with quadratic floor space and for the discs, a cylinder was used, representing the non-bombarded. The bombarded area, given by the rest of the simulation volume, is again modeled with a reduced saturation magnetization [Huc18], reduced exchange stiffness [Lel14], and vanishing exchange interaction between the FM and AFM layers [Mü18]. In Fig. 5.30 the changes are visualized.

In Fig. 5.31 simulation results for a 2 µm embedded squares are visualized. In a) the corresponding hysteresis loop can be seen. Again, a double hysteresis structure can be identified and as it can be seen in b) the upper part of the hysteresis accounts for the remagnetization of

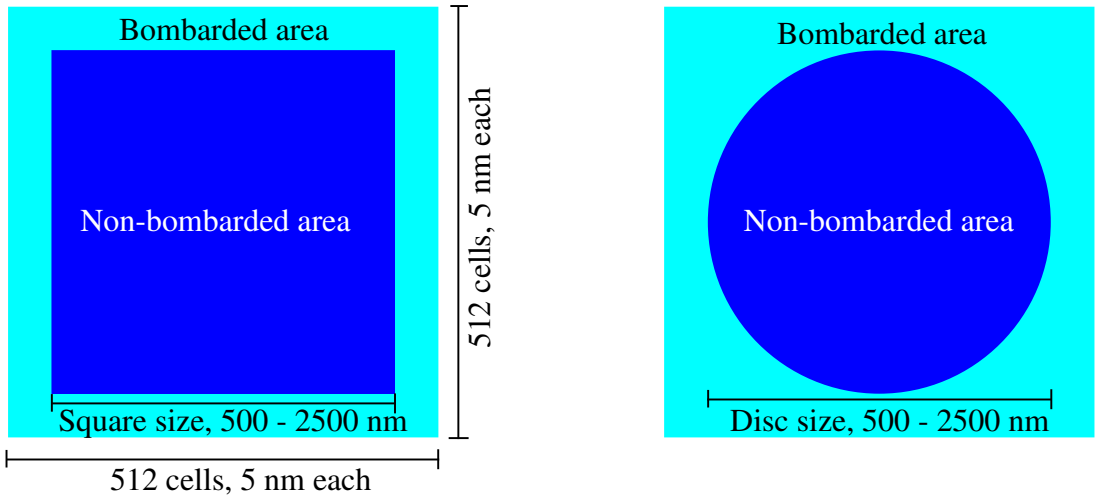

Figure 5.30: Schematic visualizing the simulation approach for the embedded squares and discs. The total simulation size is again 2.56 µm x 2.56 µm, while the geometries have a total size of 0.5 µm to 2.5 µm. The bombarded area filling the rest of the simulation area.

the bombarded area. On the DFB, the bombarded area nucleates first of all on the left and the right side of the squares. Afterward, the rest of the bombarded area and the actual square is nucleating, starting on the edges perpendicular to the field and moving towards the center. This is visible in the gradually decreasing hysteresis branch. Finally, the center rest of the square is quickly flipping, resulting in a negative saturation and a fast decrease of the remaining hysteresis branch. On the IFB, the squares are nucleating at first, again starting on the edges, followed by a flip of the hole square and the bombarded area perpendicular to the field. The bombarded part parallel to the field nucleates at last.

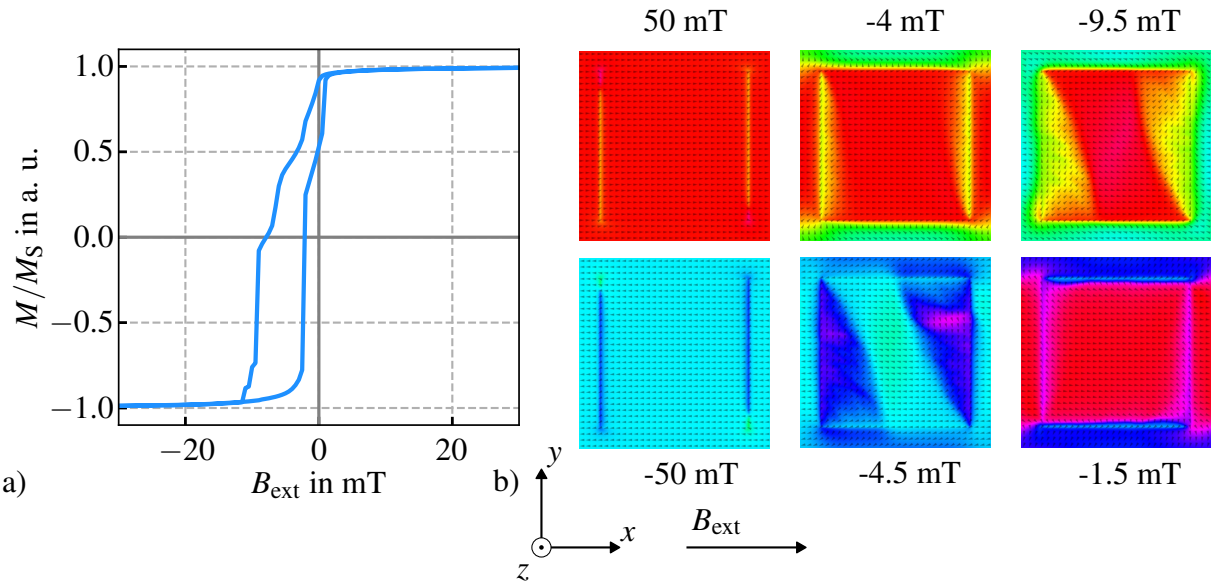

Figure 5.31: a) The obtained hysteresis loop for the 2 µm embedded square, showing the expected double hysteresis structure. b) The corresponding magnetization of the FM layer.

In positive and negative saturation artifacts on the left and right side can be seen. These are the result of the different saturation magnetizations, leading to a interface energy between bombarded and non-bombarded areas. The resulting EB field of the square reads 8.5 mT. The coercive field is given by 8.5 mT as well. Compared to the other experiments the coercive field seems to be overestimated, but the EB field doesn't seem to be unrealistic.
In Fig. 5.32 further results for the EB field and the coercive fields of the embedded squares are given. For the squares below 0.75 µm and above 2 µm the bombarded and non-bombarded parts of the hysteresis could not be separated, so they are left out here. The EB field for the bombarded area is vanishing for all stripes and the coercive field of the bombarded area is also close to zero. For the non-bombarded area, the coercive field is increasing for decreasing square size at first to 10.5 mT for the 1.25 µm square, but it then decreasing to 8.5 mT again. The EB fields are decreasing with decreasing square size from 8.5 mT to 4 mT for the smallest square. Overall, the results are comparable with the embedded stripes.

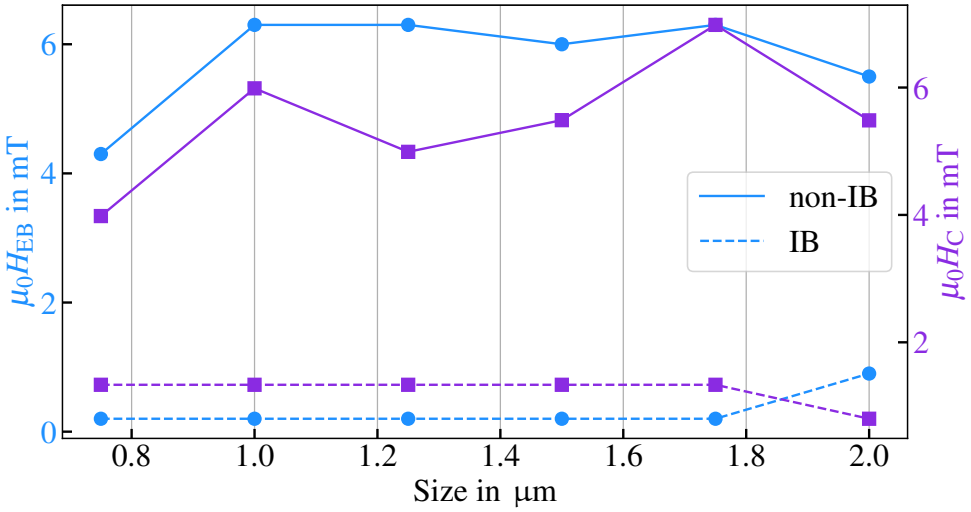

Figure 5.32: Simulated EB (blue) and coercive (violet) fields of the bombarded (dashed) and non-bombarded (solid) areas for the different disc sizes.

The same approach was done to simulate the embedded discs. Instead of a cuboid a cylinder was used. All other parameters are kept unchanged. In Fig. 5.33 the results for a simulated 2 µm disc are given. In a) the obtained hysteresis can be seen. Again, a double hysteresis structure can be identified. As for the embedded stripes and squares, the upper part corresponds to the bombarded area, while the lower part corresponds to the non-bombarded area. For the bombarded area, the EB field and the coercive field are nearly vanishing, possessing only about 1 mT. The actual disc is possessing an EB field of 5.5 mT and a coercive field of 5.5 mT as well. Compared to the square, both fields are smaller and the hysteresis is much steeper. Since this was also the case for the freestanding geometries, one can assume, that this is connected to the geometry and finite-difference method, as explained before. Taking a look at the nucleation, the overall remagnetization is the same as for the embedded square. On the DFB, the

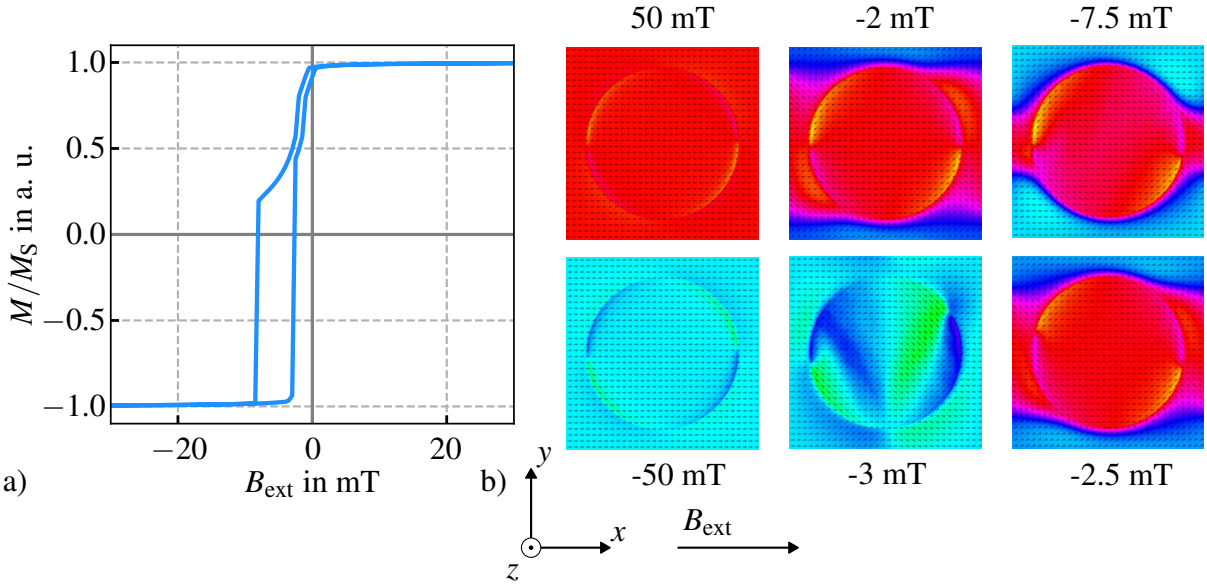

Figure 5.33: a) The obtained hysteresis loop for the 2 µm embedded disc, showing the expected double hysteresis structure. b) The corresponding magnetization of the FM layer.

bombarded area parallel to the field is nucleating first. Followed by a domain movement across the remaining bombarded area. At −8 mT the magnetization is flipping, resulting in negative saturation. This fast reversal can also be seen in the steep hysteresis. On the IFB, the magnetic reversal of the discs is again characterized by a fast flip at −2.5 mT, just after a starting rotation appeared at −3 mT . In Fig. 5.34 results for the other disc sizes are given. The EB field and coercive field of the bombarded area are nearly vanishing for all sizes and are in the range between 0 and 2 mT. The EB field of the disc itself is also quite constant at about 6 mT and only decreases to 4 mT for the 0.75 µm disc. For the coercive fields, the tend cannot be seen,

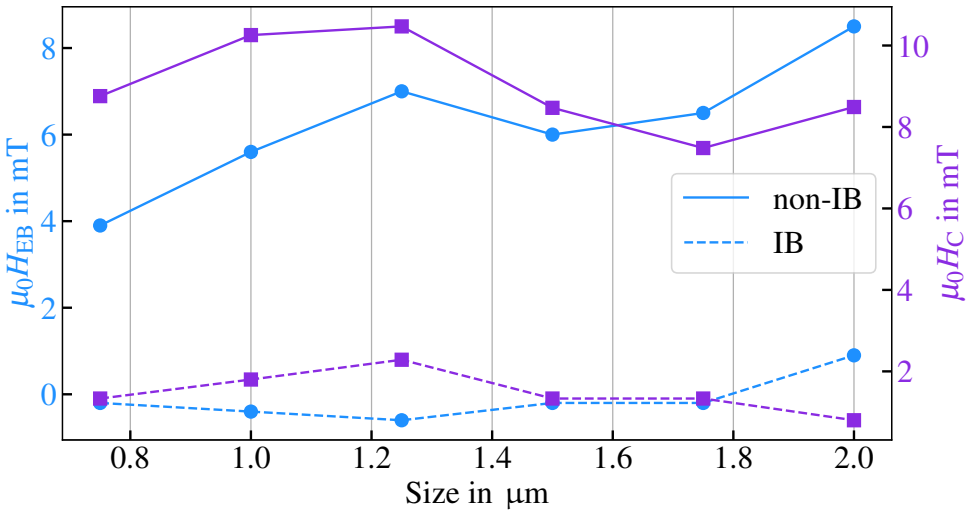

Figure 5.34: Simulated EB (blue) and coercive (violet) fields of the bombarded (dashed) and non-bombarded (solid) areas for the different disc sizes.

since it increases first to 7 mT for the 1.75 µm disc and decreases to 5 mT for the 1.25 µm disc. Overall a decreasing coercive field with decreasing stripe width can be expected experimentally.

In this chapter simulations of embedded EB squares and discs have been presented. The geometries possessed sizes of 0.5 µm to 2.5 µm. For all geometries, hysteresis loops were simulated and the magnetic reversal process was investigated. Like in the case of the embedded EB stripes, a double hysteresis structure was obtained. Except for the $0.5, 0.75, 2.25$ and 2.5 µm geometries, where this double hysteresis structure was not visible due to the limiting simulation volume. Besides that, trends in the EB and coercive fields were identified in dependence on the geometry size. The simulations presented can be compared with experiments, which will be performed in the future.

6 Summary and Outlook

In this work, micromagnetic simulations were used to investigate exchange-biased thin film patterned micro geometries. Experimental results of NiFe(10 nm)/IrMn(30 nm) thin film systems acted as a reference in terms of hysteresis loop properties and nucleation behavior within the magnetic reversal process. The systems were produced by sputtering, lithographical processes, and/or ion bombardment, resulting in freestanding and embedded stripes, cubes, and discs, with sizes in the micrometer range between 1 and 10 µm. To model the experimental systems and reproduce the results, an existing model by De Clercq [Cle16] has been extended. For the simulations, MuMax3 was used, which is a finite-difference-based micromagnetic simulation program, that uses the GPU to accelerate the computation [Van14]. Furthermore, experiments were performed to investigate certain simulation approaches for reasonability.

In principle, the model is only simulating the interface of the antiferromagnetic (AFM) layer. The interface itself is simulated by a polycrystalline model, consisting of grains that are pinned or rotatable. The pinned grains establish the exchange bias (EB) effect, while the rotatable grains increase the coercive field. This idea is based on the assumptions of Fulcomer and Charap [Ful72] and Harres et al. [Har12]. The total simulation volume was about 2.5 µm x 2.5 µm x 12 nm, allowing the simulation of geometries in the micrometer range. The volume is discretized in cubes of 5 nm x 5 nm x 3 nm. Thereby, the top three layers are used for the ferromagnetic (FM) layer and one more layer for the AFM interface.

In the first part of this work, the model by De Clercq [Cle16] was applied to full film simulations and our $Ni_{81}Fe_{19}$/$Ir_{17}Mn_{83}$ thin film system. Using appropriate material parameters, a realistic hysteresis loop could be produced. For the full film simulations, parameter studies were carried out. By changing the number of pinned grains, the EB strength could be varied. Thereby, the expected linear dependence was observed. Further, the coercive field was decreasing with an increasing pinning ratio. The results of Harres et al. [Har12] could therefore be reproduced. Extending on that, an asymmetry was observed, which dependence on the pinning ratio and the angle between EB field and the external field, following the results of Camarero et al. [Cam05]. The dependence of the EB and coercive field on the FM and AFM layer thicknesses were also simulated and showed the expected behavior. Only the dependence of the coercive field on the FM layer thickness could not be reproduced. Lastly, the angular dependence of the grain's anisotropies was investigated, showing a strong dependence of the EB field on the angular distribution of the pinned grain's anisotropy.

The model for the full film simulations was further used in the simulations for the patterned ge-

ometries. First of all, the freestanding micro stripes were simulated. By just limiting the width of the full film to get a stripe, the desired nucleation behavior was not reached. On the decreasing field branch (DFB), the nucleation should start in the middle, while on the increasing field branch (IFB) the nucleation should start on the edges of the stripes. Besides that, experimental results indicate an increasing EB effect with decreasing stripe width. The general requirement to match the experimental results is an increased EB effect in an edge region on the left and the right side of the stripes. Two possible cases were found to induce such a nucleation behavior. An increased pinning ratio in the edges and a reduced saturation magnetization. By defining an edge region of 200 nm on each side, the two different properties could be included in the simulation. In both cases, the experimental results could be reproduced. Doubling the pinning ratio in the edges lead to the desired nucleation behavior and EB increase. Alternatively, the saturation magnetization can be reduced to 60%, leading again to the desired results. The two different approaches were further investigated experimentally, to test them for plausibility. An increased pinning ratio could be explained by a structural change in the edges of the AFM layer. An atomic force microscope was used to investigate the polycrystalline surface structure of a 5 µm stripe pattern consisting only of the IrMn layer at 15 different spots. By determining the grain radius distribution and fitting a lognormal function, the most probable radius was determined. Here, no clear difference was observable. Opposed to that, VVSM measurements indeed showed a decreasing saturation magnetization with decreasing stripe width if normalized to the magnetic volume. Indicating that a reduced saturation magnetization in the edges can be assumed.

Next, the embedded micro stripes were simulated. By ion bombardment (IB), the EB effect was destroyed between the stripes. To reproduce the experimental observation, the simulation approach was changed. The edge region was neglected, and the layer system was extended to the full simulation volume. To incorporate the effects of the IB in the bombarded areas, the saturation magnetization and exchange stiffness were reduced and the interface exchange coupling between the AFM and FM layer was neglected. By this, the experimentally observed double hysteresis loop could be reproduced with realistic properties. Further, the dependencies of the EB and coercive fields on the stripe width could be reproduced in good agreement with the experiments. Especially, the nucleation behavior could be reproduced in very good agreement. On the DFB, the bombarded areas nucleate first, followed by a magnetic reversal in the stripe center. On the IFB, first, the stripe's center is nucleating, followed by the bombarded area starting at the stripe's edge. All in all, the embedded stripes could be modeled in great detail.

After simulating the stripes, freestanding squares and discs were modeled following the same idea. To simulate the squares, a further spatial limiting was set, and the edge region was included. Experimentally, the nucleation is different compared to the stripes. On the DFB, the remagnetization starts in the edges parallel to the field, while on the IFB the nucleation starts in the center of the squares. This behavior was tried to be incorporated by reducing the pinning ratio in the edge region. Unfortunately, the nucleation process could not be reproduced.

Even though, the obtained hysteresis loops are realistic, showing a more curved shape. The discs were modeled by cylinders. Here, a strong change in the hysteresis loop was observed. While experimentally there was no significant difference to the squares, the simulated loops were much steeper and possessed smaller coercive fields. The reason is most probably located in the finite-difference method used for the discretization and the limited capability to simulate curved geometries. Using a finite-element-based solution should increase the simulation quality.

Finally, embedded squares and discs were modeled. Since there exist no experimental results for those geometries, the results are an outlook for future experiments. The model is only slightly changed from the embedded stripes by changing the stripes to squares or discs. Again, a double hysteresis loop can be observed. In terms of magnetization reversal, the bombarded areas nucleate first on the DFB, and on the IFB, the non-bombarded areas nucleate first. The embedded squares themselves nucleate like the freestanding ones, while the embedded discs are nucleating much faster by a spin-flip, which can also be seen by the steep hysteresis. The limits of the finite-difference method need to be considered as well.

In future simulations, other geometries might be investigated, allowing to anticipate experimental results before the fabrication of those systems. Further, simulations of stray field landscapes above a patterned EB system, like presented in [Ehr15, Gau16, Huh22], are possible and first results are under investigation. Also, more complex effects like spin-spirals in multi-layered EB systems should be achievable in future simulations. The presented results are therefore an important basis for upcoming simulations. With increasing computation power and memory capacity, larger geometries in the range of dozen micrometers could be simulated. Here, it needs to be kept in mind that the computation time and memory consumption linearly scales with the number of cells [Lel18], making larger cell numbers accessible in the future. Besides increasing the simulation volume, the cell size could be reduced, resulting in the possibility to simulate material with a smaller exchange lengths l_{ex} [Abo13], meaning materials with a smaller exchange stiffness A_{ex} or higher saturation magnetization M_{S}. A challenging task is the simulation of out-of-plane magnetized systems, like thin Co layers. So far, attempts to simulate those systems were not successful. Challenging is here the fact, that an out-of-plane magnetization leads to large stray fields above the sample. Those stray fields are then only simulated correctly, if the simulation volume is large enough in the z-direction, extending heavily the computational effort and memory needs. Besides that, further experiments with multiple FM/AFM interfaces in combination with IB are done. Simulations incorporating different ion doses and layer thicknesses could bring insides into the magnetic behavior of such systems, and even give the opportunity to easily investigate each layer's behavior separately.

7 Appendix

7.1 Lithography process parameters

Table 7.1: Process parameters used for the UV-lithography

	positive photoresist	negative photoresist
hard-baking	10 min @ 120°C	10 min @ 120°C
Ti-Prime	4000 rpm 40 s	4000 rpm 40 s
spin-coating	AZ 1505 2000 rpm 30 s	AZnLoF 2070 (4:3) 6000 rpm 40 s
soft-baking	5 min @ 90°C	5 min @ 100°C
UV exposure in MA4	5.5 s	14.5 s
post exposure bake		1 min @ 110°C
development	15 s in KOH	30 s in AZ 826 MIF
water rinsing	30 s	30 s

7.2 Mumax3 Code for a full film simulation

```
//Set cell size in x,y,z
Cx := 5.0e-9
Cy := 5.0e-9
Cz := 3.0e-9

//Set number of cells in x,y,z
num_FM_layers := 3 // 9nm FM layer
Nx := 512
Ny := 512
Nz := 1 + num_FM_layers

//Define geometry (full film)
setgridsize(Nx, Ny, Nz)
setcellsize(Cx, Cy, Cz)
setgeom(cuboid(Nx*Cx, Ny*Cy, Nz*Cz))
```

```
//Periodic boundary condition
setPBC(10, 10, 0)

//200 Regions for AFM grains
maxRegion := 200
for i := 0; i < maxRegion; i++ {
        DefRegion(i, Layer(0))
}

//FM material parameters
A_FM := 13e-12
M_FM := 796e3
K_FM := 1000

//FM region 201 to 200 + num_FM_layers
for i := 201; i < 201+num_FM_layers; i++ {
        Aex.setRegion(i, A_FM)
        Msat.setRegion(i, M_FM)
        DefRegion(i, Layer(i-200)) // 1 to num_FM_layers
        m.setRegion(i, uniform(0.1, 0, 0))
        Ku1.SetRegion(i, K_FM)
        AnisU.SetRegion(i, vector(1, 0.1, 0))
}

//Define grains
grainSize := 10e-9
randomSeed := 1234567
ext_make3dgrains(grainSize, 0, maxRegion, layer(0), randomSeed)

//AFM parameters
t_AFM := Cz
M_AFM := M_FM
A_A_rot := 1.1e-11
A_A_pin := 1.1e-11
K_AFM_pin := 2.7e8
K_AFM_rot := 4000
number_of_pin := 60 //30% pinned
angle_pinned := 0.0 //angle of pinned anisotropy
```

```
angle_rot := 0.0    //angle of rot anisotropy

angle := 0.0
axis1 := vector(1, 0, 0)

// First number_of_pin regions for pinned grains
for i := 0; i < number_of_pin; i++ {
        NoDemagSpins.SetRegion(i, 1)
        frozenspins.SetRegion(i, 1)
        Aex.setRegion(i, A_A_pin)
        Msat.setRegion(i, M_AFM)
        angle = angle_pinned * pi / 180 * randNorm()
        axis1 = vector(cos(angle), sin(angle), 0)
        anisU.SetRegion(i, axis1)
        m.setRegion(i, uniform(cos(angle), sin(angle), 0))
        K := K_AFM_pin
        Ku1.SetRegion(i, K)
}

// Rest for rotatable grains
for i := number_of_pin; i < maxRegion; i++ {
        NoDemagSpins.SetRegion(i, 1)
        Aex.setRegion(i, A_A_rot)
        Msat.setRegion(i, M_AFM)
        angle = angle_rot * pi / 180.0 * randNorm()
        axis1 = vector(cos(angle), sin(angle), 0)
        anisU.SetRegion(i, axis1)
        m.setRegion(i, uniform(cos(angle), sin(angle), 0))
        K := K_AFM_rot
        Ku1.SetRegion(i, K)
}

//FM/AFM exchange coupling
J_I_pin := 1.8e-4
J_I_rot := 0.4e-4
alpha_H_pin := (2 / M_FM) * (1 / (1/A_FM + 1/A_A_pin))
for i := 0; i < number_of_pin; i++ {
        for j := 201; j < 202; j++ {
                ext_ScaleExchange(i, j,
```

```
                        J_I_pin*Cz/(2*M_FM*alpha_H_pin))
        }
}
alpha_H_rot := (2 / M_FM) * (1 / (1/A_FM + 1/A_A_rot))
for i := number_of_pin; i < maxRegion; i++ {
        for j := 201; j < 202; j++ {
                ext_ScaleExchange(i, j,
                        J_I_rot*Cz/(2*M_FM*alpha_H_rot))
        }
}
for i := 0; i < maxRegion; i++ {
        for j := 0; j < i; j++ {
                ext_ScaleExchange(i, j, 0)
        }
}

//Run hysteresis loop and save magnetization
B_app := 0.0
TableAddVar(B_app, "B_app", "T")
TableAdd(m.Region(200 + num_FM_layers))
TableAdd(CropLayer(m, 0))
B_ext.setregion(201, vector(1, 0, 0))
B_ext.setregion(202, vector(1, 0, 0))
B_ext.setregion(203, vector(1, 0, 0))
relax()
for i := 100; i > -101; i-- {
        B_app = i * 1e-3
        B_ext.setregion(201, vector(B_app*cos(3.0*pi/180),
                B_app*sin(3.0*pi/180), 0))
        B_ext.setregion(202, vector(B_app*cos(3.0*pi/180),
                B_app*sin(3.0*pi/180), 0))
        B_ext.setregion(203, vector(B_app*cos(3.0*pi/180),
                B_app*sin(3.0*pi/180), 0))
        tablesave()
        minimize()
}
for i := -100; i < 101; i++ {
        B_app = i * 1e-3
        B_ext.setregion(201, vector(B_app*cos(3.0*pi/180),
```

```
            B_app*sin(3.1*pi/180), 0))
        B_ext.setregion(202, vector(B_app*cos(3.0*pi/180),
            B_app*sin(3.1*pi/180), 0))
        B_ext.setregion(203, vector(B_app*cos(3.0*pi/180),
            B_app*sin(3.1*pi/180), 0))
        tablesave()
        minimize()
}
```

7.3 Mumax3 Code for a stripe with reduced saturation magnetization

```
//Set cell size in x,y,z
Cx := 5.0e-9
Cy := 5.0e-9
Cz := 3.0e-9

//Set number of cells in x,y,z
num_FM_layers := 3 // 9nm FM layer
Nx := 512
Ny := 512
Nz := 1 + num_FM_layers

//Define geometry (full film)
setgridsize(Nx, Ny, Nz)
setcellsize(Cx, Cy, Cz)
setgeom(cuboid(Nx*Cx, Ny*Cy, Nz*Cz))

//Periodic boundary condition
setPBC(10, 0, 0)


//Stripe size
width := 2000e-9
sides := 200e-9
mid := width - 2*sides
base := cuboid(Nx*Cx, width, Nz*Cz)
setgeom(base)

//First 200 regions for AFM layer
for i := 1; i < 201; i++ {
        DefRegion(i, Layer(0))
}
//Region 205 and 206 for FM layer
for i := 1; i < 4; i++ {
        DefRegion(205, Layer(i)) //mid
        DefRegion(206, Layer(i)) //egde
```

```
}

//FM material parameters
A_FM := 13e-12
M_FM := 796e3
K_FM := 1000

/Mid of stripe
Aex.setRegion(205, A_FM)
Msat.setRegion(205, M_FM)
m.setRegion(205, uniform(0.1, 0, 0))
Ku1.SetRegion(205, K_FM)
AnisU.SetRegion(205, vector(1, 0, 0))
DefRegion(205, cuboid(Nx*Cx, mid, 3*Cz).transl(0, 0, 0.5*Cz))

//Stripe edge
A_FM_edge := A_FM
Aex.setRegion(206, A_FM_edge)
Msat.setRegion(206, 0.5*M_FM)
m.setRegion(206, uniform(0.1, 0, 0))
Ku1.SetRegion(206, K_FM)
AnisU.SetRegion(206, vector(1, 0, 0))
DefRegion(206, cuboid(Nx*Cx, sides, 3*Cz).transl(
0, (mid/2+sides/2), 0.5*Cz))
DefRegion(206, cuboid(Nx*Cx, sides, 3*Cz).transl(
0, -(mid/2+sides/2), 0.5*Cz))

//AFM material parameters
t_AFM := Cz
M_AFM := M_FM
A_AFM := 1.1e-11
K_AFM_pin := 2.7e8
K_AFM_rot := 4000
pinned_mid := 25
pinned_edge := 25
randomSeed := 23876427627
angle_pinned := 0.0
angle_rot := 0.0
angle := 0.0
```

```
axis1 := vector(1, 0, 0)

//Pinned edge (0 to pinned_edge)
for i := 1; i < pinned_edge+1; i++ {
        NoDemagSpins.SetRegion(i, 1)
        frozenspins.SetRegion(i, 1)
        Aex.setRegion(i, A_AFM)
        Msat.setRegion(i, M_AFM)
        angle = angle_pinned * pi / 180 * randNorm()
        axis1 = vector(cos(angle), sin(angle), 0)
        anisU.SetRegion(i, axis1)
        m.setRegion(i, uniform(cos(angle), sin(angle), 0))
        Ku1.SetRegion(i, K_AFM_pin)
}

//Rotatable edge(pinned_edge to 100)
for i := pinned_edge + 1; i < 101; i++ {
        NoDemagSpins.SetRegion(i, 1)
        Aex.setRegion(i, A_AFM)
        Msat.setRegion(i, M_AFM)
        angle = angle_rot * pi / 180.0 * randNorm()
        axis1 = vector(cos(angle), sin(angle), 0)
        anisU.SetRegion(i, axis1)
        m.setRegion(i, uniform(cos(angle), sin(angle), 0))
        Ku1.SetRegion(i, K_AFM_rot)
}

//Pinned mid (101 to pinned_mid+101)
for i := 101; i < pinned_mid+101; i++ {
        NoDemagSpins.SetRegion(i, 1)
        frozenspins.SetRegion(i, 1)
        Aex.setRegion(i, A_AFM)
        Msat.setRegion(i, M_AFM)
        angle = angle_pinned * pi / 180 * randNorm()
        axis1 = vector(cos(angle), sin(angle), 0)
        anisU.SetRegion(i, axis1)
        m.setRegion(i, uniform(cos(angle), sin(angle), 0))
        Ku1.SetRegion(i, K_AFM_pin)
}
```

```
//Rotatable mid (pinned_mid+101 to 200)
for i := pinned_mid + 101; i < 201; i++ {
        NoDemagSpins.SetRegion(i, 1)
        Aex.setRegion(i, A_AFM)
        Msat.setRegion(i, M_AFM)
        angle = angle_rot * pi / 180.0 * randNorm()
        axis1 = vector(cos(angle), sin(angle), 0)
        anisU.SetRegion(i, axis1)
        m.setRegion(i, uniform(cos(angle), sin(angle), 0))
        Ku1.SetRegion(i, K_AFM_rot)
}

//FM/AFm coupling in edges and mid

J_II_middle := 0.4e-4
J_II_edge := 0.4e-4
J_III_middle := 1.8e-4
J_III_edge := 1.8e-4

alpha_H_pin := (2 / M_FM) * (1 / (1/A_FM + 1/A_AFM))

for i := 1; i < pinned_edge; i++ {
        ext_ScaleExchange(i, 205,
                J_III_edge*Cz/(2*M_FM*alpha_H_pin))
        ext_ScaleExchange(i, 206,
                J_III_edge*Cz/(2*M_FM*alpha_H_pin))
}
for i := pinned_edge; i < 101; i++ {
        ext_ScaleExchange(i, 205,
                J_II_edge*Cz/(2*M_FM*alpha_H_pin))
        ext_ScaleExchange(i, 206,
                J_II_edge*Cz/(2*M_FM*alpha_H_pin))
}
for i := 101; i < 101+pinned_mid; i++ {
        ext_ScaleExchange(i, 205,
                J_III_middle*Cz/(2*M_FM*alpha_H_pin))
        ext_ScaleExchange(i, 206,
                J_III_middle*Cz/(2*M_FM*alpha_H_pin))
}
```

```
for i := 101 + pinned_mid; i < 201; i++ {
        ext_ScaleExchange(i, 205,
                J_II_middle*Cz/(2*M_FM*alpha_H_pin))
        ext_ScaleExchange(i, 206,
                J_II_middle*Cz/(2*M_FM*alpha_H_pin))
}
for i := 0; i < 201; i++ {
        for j := 0; j < i; j++ {
                ext_ScaleExchange(i, j, 0)
        }
}

//Grains for AFM
grain_size_mid := 10e-9
grain_size_edge := 10e-9

ext_make3dgrains(grain_size_mid, 101, 99,
cuboid(Nx*Cx, mid, 1*Cz)
.transl(0, 0, -1.5*Cz), 2434533)
ext_make3dgrains(grain_size_edge, 1, 99,
cuboid(Nx*Cx, sides, 1*Cz)
.transl(0, (mid/2+sides/2), -1.5*Cz), 2434533)
ext_make3dgrains(grain_size_edge, 1, 99,
cuboid(Nx*Cx, sides, 1*Cz)
.transl(0, -(mid/2+sides/2), -1.5*Cz), 523863482)

//Run hysteresis loop and save magnetization
B_app := 0.0
TableAddVar(B_app, "B_app", "T")
TableAdd(CropLayer(m, 3))
TableAdd(CropLayer(m, 0))
B_ext.setregion(205, vector(0.1, 0, 0))
B_ext.setregion(206, vector(0.1, 0, 0))
relax()
B_ext = vector(0, 0, 0)
for i := 100; i > -101; i-- {
        B_app = i * 0.5e-3
        B_ext.setregion(205, vector(B_app*cos(3.0*pi/180),
                B_app*sin(3.0*pi/180), 0))
```

```
        B_ext.setregion(206, vector(B_app*cos(3.0*pi/180),
                B_app*sin(3.0*pi/180), 0))
        tablesave()
        minimize()
        snapshot(CropLayer(m, 0))
        snapshot(CropLayer(m, 3))
}
for i := -100; i < 101; i++ {
        B_app = i * 0.5e-3
        B_ext.setregion(205, vector(B_app*cos(3.0*pi/180),
                B_app*sin(3.0*pi/180), 0))
        B_ext.setregion(206, vector(B_app*cos(3.0*pi/180),
                B_app*sin(3.0*pi/180), 0))
        tablesave()
        minimize()
        snapshot(CropLayer(m, 0))
        snapshot(CropLayer(m, 3))
}
```

List of important abbreviations

(AFM)	antiferromagnet(ic)
(DFB)	decreasing field branch
(EB)	exchnage bias(ed)
(FC)	field cooling
(FM)	ferromagnet(ic)
(IB)	ion bombardment
(IFB)	increasing field branch
(VSM)	vibrating sample magnetometry
(VVSM)	vector vibrating sample magnetometry

Danksagung

An dieser Stelle möchte ich mich bei allen bedanken, die diese Arbeit möglich gemacht haben oder mich bei der Anfertigung unterstützt haben.

An aller erster Stelle möchte ich mich bei Herrn Prof. Dr. Arno Ehresmann für die Aufnahme in seine Gruppe bedanken. Ohne die Möglichkeit der Nutzung der Labore und des Simulationsrechners wäre diese Arbeit nicht möglich gewesen. Ergänzend bedanke ich mich für die Übernahme des Erstgutachtens dieser Arbeit und bedanke ich mich ebenso bei Herrn Prof. Dr. Kilian Singer für die Annahme des Zweitgutachtens.

Des Weiteren möchte ich mich bei meiner Betreuerin Sapida Akhundzada für die sehr gute Betreuung und die Unterstützung bei Experimenten, insbesondere bei der Fertigung der Proben, dem VSM und dem Kerr-Mikroskop, bedanken. Genauso gilt mein besonderer Dank Christian Janzen für die Unterstützung bei der Verwendung des Rasterkraftmikroskops. Nicht untererwähnt sollen meine wunderbaren Kollegen Arne Vereijken, Maximillian Merkel, Yahya Shubbak und Florian Ott bleiben, die mich ebenfalls tatkräftig unterstützt haben. Weiterer Dank gilt unserem Techniker Arne Schröder und unserer Sekretärin Andrea Wecker. Ich danke mich für die großartige Zeit.

Nicht zuletzt möchte ich mich auch bei meiner Familie und Freunden für die fortwährende Unterstützung während meines gesamten Studiums bedanken.

8 Bibliography

[Abe19] Abert, C. *Micromagnetics and spintronics: models and numerical methods*. European Physical Journal B, 92(120) (2019). URL https://link.springer.com/article/10.1140/epjb/e2019-90599-6.

[Abo13] Abo, G. S. and Hong, Y.-K. and Park, J. and Lee, J. and Lee, W. and Choi, B.-C. *Definition of Magnetic Exchange Length*. IEEE Transactions on Magnetics, 49(8), 4937 (2013). URL https://ieeexplore.ieee.org/document/6497624.

[Akh22] Akhundzada, S. *private communication*. University of Kassel (2022).

[Bar13] Barati, E. and Cinal, M. and Edwards, D. M. and Umerski, A. *Calculation of Gilbert damping in ferromagnetic films*. EPJ Web of Conferences, 40(18003) (2013). URL https://www.epj-conferences.org/articles/epjconf/abs/2013/01/epjconf_Jems2012_18003/epjconf_Jems2012_18003.html.

[Bas14] Basaran, A. C. and Saerbeck, T. and de la Venta, J. and Huckfeldt, H. and Ehresmann, A. and Schuller, Ivan K. *Exchange bias: The antiferromagnetic bulk matters*. Applied Physics Letters, 105(7), 072403 (2014). URL https://aip.scitation.org/doi/10.1063/1.4893457.

[Ber99] Berkowitz, A.E. and Takano, K. *Exchange anisotropy — a review*. Journal of Magnetism and Magnetic Materials, 200(1), 552 (1999). URL https://www.sciencedirect.com/science/article/pii/S0304885399004539.

[Bin04] Binek, C. *Training of the exchange-bias effect: A simple analytic approach*. Physical Review B, 70, 014421 (2004). URL https://link.aps.org/doi/10.1103/PhysRevB.70.014421.

[Cam05] Camarero, J. and Sort, J. and Hoffmann, A. and García-Martín, J. M. and Dieny, B. and Miranda, R. and Nogués, J. *Origin of the Asymmetric Magnetization Reversal Behavior in Exchange-Biased Systems: Competing Anisotropies*. Physical Review Letters, 95, 057204 (2005). URL https://journals.aps.org/prl/abstract/10.1103/PhysRevLett.95.057204.

[Cle16] Clercq, J. D. and Vansteenkiste, A. and Abes, M. and Temst, K. and Waeyenberge, B. V. *Modelling exchange bias with MuMax3*. Journal of Physics D: Applied

Physics, 49, 435001 (2016). URL https://iopscience.iop.org/article/10.1088/0022-3727/49/43/435001.

[Cle17] Clercq, J. D. *Modelling antiferromagnetic interfaces with MuMax3*. Ph.D. thesis, Ghent University (2017). URL https://biblio.ugent.be/publication/8530162/file/8530169.

[Ehr05] Ehresmann, A. and Junk, D. and Engel, D. and Paetzold, A. and Roell, K. *On the origin of ion bombardment induced exchange bias modifications in polycrystalline layers*. Journal of Physics D: Applied Physics, 38(6), 801 (2005). URL https://iopscience.iop.org/article/10.1088/0022-3727/38/6/001.

[Ehr06] Ehresmann, A. and Engel, D. and Weis, T. and Schindler, A. and Junk, D. and Schmalhorst, J. and Hoeink, V. and Sacher, M. D. and Reiss, G. *Fundamentals for magnetic patterning by ion bombardment of exchange bias layer systems*. physica status solidi (b), 243(1), 29 (2006). URL https://onlinelibrary.wiley.com/doi/abs/10.1002/pssb.200562442.

[Ehr15] Ehresmann, A. and Koch, I. and Holzinger, D. *Manipulation of Superparamagnetic Beads on Patterned Exchange-Bias Layer Systems for Biosensing Applications*. Sensors, 15(11), 28854 (2015). URL https://www.mdpi.com/1424-8220/15/11/28854.

[Eng05] Engel, D. and Ehresmann, A. and Schmalhorst, J. and Sacher, M. and Hoeink, V. and Reiss, G. *Initialization of unidirectional anisotropy in a ferromagnet–antiferromagnet bilayer by keV-He ion bombardment*. Journal of Magnetism and Magnetic Materials, 293(3), 849 (2005). URL https://www.sciencedirect.com/science/article/pii/S0304885304018438.

[Fer08] Fert, A. *Nobel Lecture: Origin, development, and future of spintronics*. Rev. Mod. Phys., 80, 1517 (2008). URL https://link.aps.org/doi/10.1103/RevModPhys.80.1517.

[Fit00] Fitzsimmons, M. R. and Yashar, P. and Leighton, C. and Schuller, Ivan K. and Nogués, J. and Majkrzak, C. F. and Dura, J. A. *Asymmetric Magnetization Reversal in Exchange-Biased Hysteresis Loops*. Physical Review Letters, 84, 3986 (2000). URL https://journals.aps.org/prl/abstract/10.1103/PhysRevLett.84.3986.

[Fra00] Fraune,M. and Rüdiger,U. and Güntherodt,G. and Cardoso,S. and Freitas,P. . *Size dependence of the exchange bias field in NiO/Ni nanostructures*. Applied Physics Letters, 77(23), 3815 (2000). URL https://aip.scitation.org/doi/10.1063/1.1330752.

[Fra21] Franco, V. and Dodrill, B. *Magnetic Measurement Techniques for Materials Characterization*. Springer Cham, 1 edition (2021). URL https://link.springer.com/book/10.1007/978-3-030-70443-8.

[Ful72] Fulcomer, E. and Charap, S. H. *Thermal fluctuation aftereffect model for some systems with ferromagnetic-antiferromagnetic coupling*. Journal of Applied Physics, 43(10), 4190 (1972). URL https://aip.scitation.org/doi/10.1063/1.1660894.

[Gau16] Gaul, A. and Hankemeier, S. and Holzinger, D. and Müglich, N. D. and Staeck, P. and Frömter, R. and Oepen, H. P. and Ehresmann, A. *Engineered magnetic domain textures in exchange bias bilayer systems*. Journal of Applied Physics, 120(3), 033902 (2016). URL https://aip.scitation.org/doi/10.1063/1.4958847.

[Gau17] Gaul, A. *Erzeugung remanent stabiler Domänenmuster in austauschverschobenen Dünnschichtsystemen mittels Heliumionenmikroskopie*. Ph.D. thesis, University of Kassel (2017).

[Ger22] Gerlach, W. and Stern, O. *Der experimentelle Nachweis der Richtungsquantelung im Magnetfeld*. Zeitschrift für Physik, 9, 349–352 (1922). URL https://link.springer.com/article/10.1007/BF01326983.

[Get08] Getzlaff, M. *Fundamentals of Magnetism*. Springer-Verlag, 1 edition (2008). URL https://link.springer.com/book/10.1007/978-3-540-31152-2.

[Gwy22] Gwyddion. *Gwyddion Dokumentation* (22.12.2022). URL http://gwyddion.net/documentation/.

[Har12] Harres, A. and Geshev, J. *A polycrystalline model for magnetic exchange bias*. Journal of Physics: Condensed Matter, 24(32), 326004 (2012). URL https://iopscience.iop.org/article/10.1088/0953-8984/24/32/326004.

[Hei08] Heitkamp, B. *Ultraschnelle Magnetisierungsdynamik: Co und Fe20Ni80 / IrMn*. Ph.D. thesis, Technische Universität Berlin (2008).

[Hol15] Holzinger, D. *Transport magnetischer Partikel durch maßgeschneiderte magnetische Feldlandschaften zur Anwendung in mikrofluidischen Mischprozessen*. Ph.D. thesis, University of Kassel (2015).

[Hub98] Hubert, A. and Schäfer, R. *Magnetic Domains*. Springer-Verlag, 1 edition (1998). URL https://link.springer.com/book/10.1007/978-3-540-85054-0.

[Huc18] Huckfeldt, H. *Strukturelle und magnetische Veränderungen in Schichtsystemen mit Grenzflächenaustauschkopplung nach dem Beschuss mit keV-Heliumionen*. Ph.D. thesis, University of Kassel (2018).

[Huh22] Huhnstock, R. *Analysis of near-substrate magnetic particle transport for Lab-on-a-chip applications: stray field modulations, influence of particle properties and three-dimensional trajectories*. Ph.D. thesis, University of Kassel (2022).

[Hun25] Hund, F. *Zur Deutung verwickelter Spektren, insbesondere der Elemente Scandium bis Nickel*. Zeitschrift für Physik, 33, 345–371 (1925). URL https://link.springer.com/article/10.1007/BF01328319.

[Kas05] Kassing, R. and Blügel, S. and Bergmann, L. and Schäfer C. *Lehrbuch der Experimentalphysik, 6. Festkoerper*. de Gruyter, 2 edition (2005).

[Kim00] Kim, J.-V. and Stamps, R. L. and McGrath, B. V. and Camley, R. E. *Angular dependence and interfacial roughness in exchange-biased ferromagnetic/antiferromagnetic bilayers*. Physical Review B, 61, 8888 (2000). URL https://link.aps.org/doi/10.1103/PhysRevB.61.8888.

[Kim01a] Kim, J.-V. and Stamps, R. L. *Defect-modified exchange bias*. Applied Physics Letters, 79(17), 2785 (2001). URL https://aip.scitation.org/doi/10.1063/1.1413731.

[Kim01b] Kim, J.-V. and Stamps, R. L. *Theory of long-wavelength spin waves in exchange biased bilayers*. Journal of Applied Physics, 89(11), 7651 (2001). URL https://aip.scitation.org/doi/10.1063/1.1357867.

[Kim05] Kim, J.-V. and Stamps, R. L. *Hysteresis from antiferromagnet domain-wall processes in exchange-biased systems: Magnetic defects and thermal effects*. Physical Review B, 71, 094405 (2005). URL https://link.aps.org/doi/10.1103/PhysRevB.71.094405.

[Kiw01] Kiwi, M. *Exchange bias theory*. Journal of Magnetism and Magnetic Materials, 234(3), 584 (2001). URL https://www.sciencedirect.com/science/article/pii/S0304885301004218.

[Lan35] Landau, L. and Lifshitz, E. *On the theory of dispersion of magnetic permeability in ferromagnetic bodies*. Physikalische Zeitschrift der Sowjetunion, 8, 153 (1935).

[Lel14] Leliaert, J. and Van de Wiele, B. and Vansteenkiste, A. and Laurson, L. and Durin, G. and Dupré, L. and Van Waeyenberge, B. *A numerical approach to incorporate intrinsic material defects in micromagnetic simulations*. Journal of Applied Physics, 115(17), 17D102 (2014). URL https://aip.scitation.org/doi/10.1063/1.4854956.

[Lel18] Leliaert, J. *Fast micromagnetic simulations on GPU — recent advances made with mumax3*. Journal of Physics D: Applied Physics, 51(123002) (2018). URL https://iopscience.iop.org/article/10.1088/1361-6463/aaab1c.

[Mü16] Müglich, N. D. *Exchange-Bias-Dünnschichtsysteme — Charakterisierung, Modellierung und Anwendung*. Ph.D. thesis, University of Kassel (2016).

[Mü18] Müglich, N. D. and Merkel, M. and Gaul, A. and Meyl, M. and Götz, G. and Reiss, G. and Kuschel, T. and Ehresmann, A. *Preferential weakening of rotational magnetic anisotropy by keV-He ion bombardment in polycrystalline exchange bias layer systems*. New Journal of Physics, 20(5), 053018 (2018). URL https://iopscience.iop.org/article/10.1088/1367-2630/aabcb3.

[Maa08] Maalouf, A. and Gadonna, M. and Bosc, D. . *An improvement in standard photolithography resolution based on Kirchhoff diffraction studies*. Journal of Physics D: Applied Physics, 42(1), 015106 (2008). URL https://dx.doi.org/10.1088/0022-3727/42/1/015106.

[Mal66] Mallinson, J. *Magnetometer Coils and Reciprocity*. Journal of Applied Physics, 37, 2514 (1966). URL https://aip.scitation.org/doi/10.1063/1.1708848.

[Mal87] Malozemoff, A. P. *Random-field model of exchange anisotropy at rough ferromagnetic-antiferromagnetic interfaces*. Physical Review B, 35, 3679 (1987). URL https://link.aps.org/doi/10.1103/PhysRevB.35.3679.

[Mau87] Mauri, D. and Kay, E. and Scholl, D. and Howard, J. K. *Novel method for determining the anisotropy constant of MnFe in a NiFe/MnFe sandwich*. Journal of Applied Physics, 62(7), 2929 (1987). URL https://aip.scitation.org/doi/10.1063/1.339374.

[McC03] McCord, J. and Schäfer, R. and Mattheis, R. and Barholz, K.-U. *Kerr observations of asymmetric magnetization reversal processes in CoFe/IrMn bilayer systems*. Journal of Applied Physics, 93(9), 5491 (2003). URL https://aip.scitation.org/doi/10.1063/1.1562732.

[Mei56] Meiklejohn, W. H. and Bean, C. P. *New Magnetic Anisotropy*. Physical Review, 102, 1413 (1956). URL https://link.aps.org/doi/10.1103/PhysRev.102.1413.

[Mer20] Merkel, M. and Huhnstock, R. and Reginka, M. and Holzinger, D. and Vogel, M. and Ehresmann, A. and Zehner, J. and Leistner, K. *Interrelation between polycrystalline structure and time-dependent magnetic anisotropies in exchange-biased bilayers*. Physical Review B, 51(123002) (2020). URL https://journals.aps.org/prb/abstract/10.1103/PhysRevB.102.144421.

[Mer22a] Merkel, M. *Validation of a generalized model for the description of polycrystalline exchange-biased magnetic thin films*. Ph.D. thesis, University of Kassel (2022).

[Mer22b] Merkel, M. and Reginka, M. and Huhnstock, R. and Ehresmann, A. *Polycrystalline exchange-biased bilayers: Magnetically effective versus structural antiferromagnetic grain volume distribution*. Physical Review B, 106, 014403 (2022). URL https://link.aps.org/doi/10.1103/PhysRevB.106.014403.

[Mes15] Meschede, D. *Gerthsen Physik*. Springer Sprektrum, 25 edition (2015). URL https://link.springer.com/book/10.1007/978-3-662-45977-5.

[Nog99] Nogués, J. and Schuller, I. K. *Exchange bias*. Journal of Magnetism and Magnetic Materials, 192(2), 203 (1999). URL https://www.sciencedirect.com/science/article/pii/S0304885398002662.

[OG10] O'Grady, K. and Fernandez-Outon, L.E. and Vallejo-Fernandez, G. *A new paradigm for exchange bias in polycrystalline thin films*. Journal of Magnetism and Magnetic Materials, 322(8), 883 (2010). URL https://www.sciencedirect.com/science/article/pii/S0304885309011561.

[Ohl03] Ohldag, H. and Scholl, A. and Nolting, F. and Arenholz, E. and Maat, S. and Young, A. T. and Carey, M. and Stoehr, J. *Correlation between Exchange Bias and Pinned Interfacial Spins*. Physical Review Letters, 91, 017203 (2003). URL https://link.aps.org/doi/10.1103/PhysRevLett.91.017203.

[Pap18] Papusoi, C. and Le, T. and Lo, C. and Kaiser, C. and Desai1, M. and Acharya, R. *Measurements of Gilbert damping parameter alpha for CoPt-based and CoFe-based films for magnetic recording applications*. Journal of Physics D: Applied Physics, 51(325002) (2018). URL https://iopscience.iop.org/article/10.1088/1361-6463/aacfcf.

[Pea81] Pease, R. F. W. *Electron beam lithography*. Contemporary Physics, 22(3), 265 (1981). URL https://doi.org/10.1080/00107518108231531.

[Pyt23] Python. *Python website* (02.03.2023). URL https://www.python.org/.

[PZL20] Peng, S., D. Zhu, W. Li, H. Wu, A. J. Grutter, D. A. Gilbert, J. Lu, D. Xiong, W. Cai, P. Shafer, K. L. Wang and W. Zhao. *Exchange bias switching in an antiferromagnet/ferromagnet bilayer driven by spin–orbit torque*. Nature Electronics, 3, 757–764 (2020). URL https://www.nature.com/articles/s41928-020-00504-6#citeas.

[Rad08] Radu, F. and Zabel, H. *Magnetic Heterostructures: Advances and Perspectives in Spinstructures and Spintransport*, chapter Exchange Bias Effect

of Ferro-/Antiferromagnetic Heterostructures, pages 97–184. Springer Berlin Heidelberg, Berlin, Heidelberg (2008). URL https://doi.org/10.1007/978-3-540-73462-8_3.

[RES03] Radu, F., M. Etzkorn, R. Siebrecht, T. Schmitte, K. Westerholt and H. Zabel. *Interfacial domain formation during magnetization reversal in exchange-biased CoO/Co bilayers*. Physical Review B, 67, 134409 (2003). URL https://journals.aps.org/prb/abstract/10.1103/PhysRevB.67.134409.

[Sak17] Sakurai, J. and Napolitano, J. *Modern Quantum Mechanics*. Cambridge University Press, 2 edition (2017). URL https://www.cambridge.org/highereducation/books/modern-quantum-mechanics/AAE1925F1A0963C6124421B03D7801AE#overview.

[Sch14] Schmidt, C. and Smolarczyk, M. and Gomer, L. and Hillmer, H. and Ehresmann, A. *Artificial sub-mum magnetic patterning by He+ ion bombardment through a mask fabricated by Ultraviolet NanoImprint Lithography (UV-NIL)*. Nuclear Instruments and Methods in Physics Research Section B: Beam Interactions with Materials and Atoms, 322, 59 (2014). URL https://www.sciencedirect.com/science/article/pii/S0168583X14000998.

[Sci23] SciPy. *SciPy website* (02.03.2023). URL https://scipy.org/.

[Soe96] Soeya, S. and Fuyama, M. and Tadokoro, S. and Imagawa, T. *NiO structure–exchange anisotropy relation in the Ni81Fe19/NiO films and thermal stability of its NiO film*. Journal of Applied Physics, 79(3), 1604 (1996). URL https://aip.scitation.org/doi/10.1063/1.361004.

[Sto47] Stoner, E. C. and Wohlfarth, E. P. *Interpretation of high coercivity in ferromagnetic materials*. Nature, 160(9), 650–651 (1947). URL https://www.nature.com/articles/160650a0.

[Sto91] Stoner, E.C. and Wohlfarth, E.P. *A mechanism of magnetic hysteresis in heterogeneous alloys*. IEEE Transactions on Magnetics, 27(4), 3475 (1991). URL https://ieeexplore.ieee.org/document/1183750.

[Sto06] Stoehr, J. and Siegmann, H.C. *Magnetism From Fundamentals to Nanoscale Dynamics*. Springer-Verlag, 1 edition (2006). URL https://link.springer.com/book/10.1007/978-3-540-30283-4.

[Til08] Tillmanns, A. and Oertker, S. and Beschoten, B. and Güntherodt, G. and Eisenmenger, J. and Schuller, I. K. *Angular dependence and origin of asymmetric magnetization reversal in exchange-biased Fe/FeF2(110)*. Physical Review B, 78, 012401 (2008). URL https://link.aps.org/doi/10.1103/PhysRevB.78.012401.

[Tse03] Tseng, A.A. and Chen, K. and Chen, C.D. and Ma, K.J. *Electron beam lithography in nanoscale fabrication: recentdevelopment*. IEEE Transactions on Electronics Packaging Manufacturing, 26(2), 141 (2003). URL https://ieeexplore.ieee.org/abstract/document/1236879.

[Van14] Vansteenkiste, A. and Leliaert, J. and Dvornik, M. *The design and verification of MuMax3*. AIP Advances 4, 107133, 4(107133) (2014). URL https://aip.scitation.org/doi/10.1063/1.4899186.

[Wu10] Wu, J. and Park, J. S. and Kim, W. and Arenholz, E. and Liberati, M. and Scholl, A. and Wu, Y. Z. and Hwang, Chanyong and Qiu, Z. Q. *Direct Measurement of Rotatable and Frozen CoO Spins in Exchange Bias System of CoO/FeAg(001)*. Physical Review Letters, 104, 217204 (2010). URL https://link.aps.org/doi/10.1103/PhysRevLett.104.217204.

[Yin06] Yin, L. F. and Wei, D. H. and Lei, N. and Zhou, L. H. and Tian, C. S. and Dong, G. S. and Jin, X. F. and Guo, L. P. and Jia, Q. J. and Wu, R. Q. *Magnetocrystalline Anisotropy in Permalloy Revisited*. PHYSICAL REVIEW LETTERS, 97(067203) (2006). URL https://journals.aps.org/prl/abstract/10.1103/PhysRevLett.97.067203.

[Zha02] Zhang, K. and Zhao, T. and Fujiwara, H. *Training effect in ferro (F)/antiferromagnetic (AF) exchange coupled systems: Dependence on AF thickness*. Journal of Applied Physics, 91(10), 6902 (2002). URL https://aip.scitation.org/doi/abs/10.1063/1.1447869.